The photometric effect of errors in Y-position could not be determined directly to better than 5 percent from the observed Pt-Cr-Ne emission line spectra. However, the light loss caused by an incorrect Y-center can be modeled using the mean point source cross-sections and the mean loci of Y-centers. Examples of observed light loss curves derived from high signal-to-noise external Tungsten lamp continuum spectra are presented. These results will provide a useful check on the subsequent modeling.

6.3.2 Location of Spectra

6.3.2.1 Definition of Y-Base and Theta-Z

In order to determine the center of a spectrum on the photocathode, the diode array is stepped perpendicular to the dispersion to make a Y-map. The standard procedure in ground calibrations was to use 24 Y-steps covering a range of 384 microns, resulting in an image with a step size of 16 microns in Y, and 512 pixels on 50 micron centers in X. The Y-map is centered on the expected position of the spectrum. We are interested in computing two parameters from the Y-map: (1) the optimum Y-deflection for acquiring the spectrum, referred to as the Y-base, and (2) the angle that the spectrum makes relative to the diode array, designated theta-Z.

The optimum Y-deflection is determined in the following manner. Once the Y-center of the spectrum is known as a function of diode number, a linear curve is fit to the points. The data points that define the Y-center can deviate from a straight line because of small distortions in the magnetic focusing fields. The linear fit is then used to define the Y-base. When the

entire diode array is covered by a spectrum, the Y-base is evaluated at diode 256, the X-center of the array. For other dispersers, where only part of the diode array is used, the Y-base is evaluated at the center of the spectrum. These central X-positions are tabulated for all disperser/tube combinations in Table 6.3.2.1-1. Examples of Y-center curves and best fit lines are shown in Figures 6.3.2.1-1 through 6.3.2.1-4. Y-bases are measured in "Y-base units," which correspond to microns to within 10%. The angle theta-Z is defined as the arctangent of the slope of the best fit line.

6.3.2.2 Algorithms for Determining the Y-Center of Spectra

Considerable thought was given to the problem of devising a general algorithm to determine the Y-center as a function of X. Since the prime method of determining Y-bases uses the on-board Pt-Cr-Ne lamps and since many regions of interest contain few bright emission lines, the algorithm must work well on low signal-to-noise data. Furthermore, many spectra are not well centered in the Y-map, so that the algorithm should be insensitive to truncation of a Y cross-section. The shapes of the cross-sections in Y vary with aperture size from the square shape shown in Figure 6.3.2.2-1 to the triangular form shown in Figure 6.3.2.2-2. Three methods for determining the center of such curves were considered: (1) cross-correlation, (2) centroiding, and (3) contour averaging. The cross-correlation method was selected, because it produced the best results for low signal levels. The merits of each method are briefly discussed in the following sections.

Table 6.3.2.1-1

END POINTS, X-CENTERS, AND EXPOSURE TIMES FOR FOS SPECTRA

GRATING	ENDPOINTS (DIODE)		RED DETECTOR CENTER (DIODE)	EXPOSURE TIME PER Y-STEP (S)
H13	*	*	*	*
H19	1	396	198	5
H27	1	512	256	5
H40	1	512	256	1
H57	1	512	256	1
H78	54	512	283	1
L15	1	126	63	1
L65	1	214	107	1
PRI	333	497	415	0.5

GRATING	ENDPOINTS (DIODE)		BLUE DETECTOR CENTER (DIODE)	EXPOSURE TIME PER Y-STEP (S)
H13	60	512	286	10
H19	1	512	256	5
H27	1	512	256	5
H40	1	512	256	2
H57	1	206	103	5
H78	*	*	*	*
L15	318	512	415	10
L65	295	373	334	10
PRI	27	178	102	0.5

*This combination is never used

Based on the June 1985 wavelength calibration by Sirk and Bohlin.

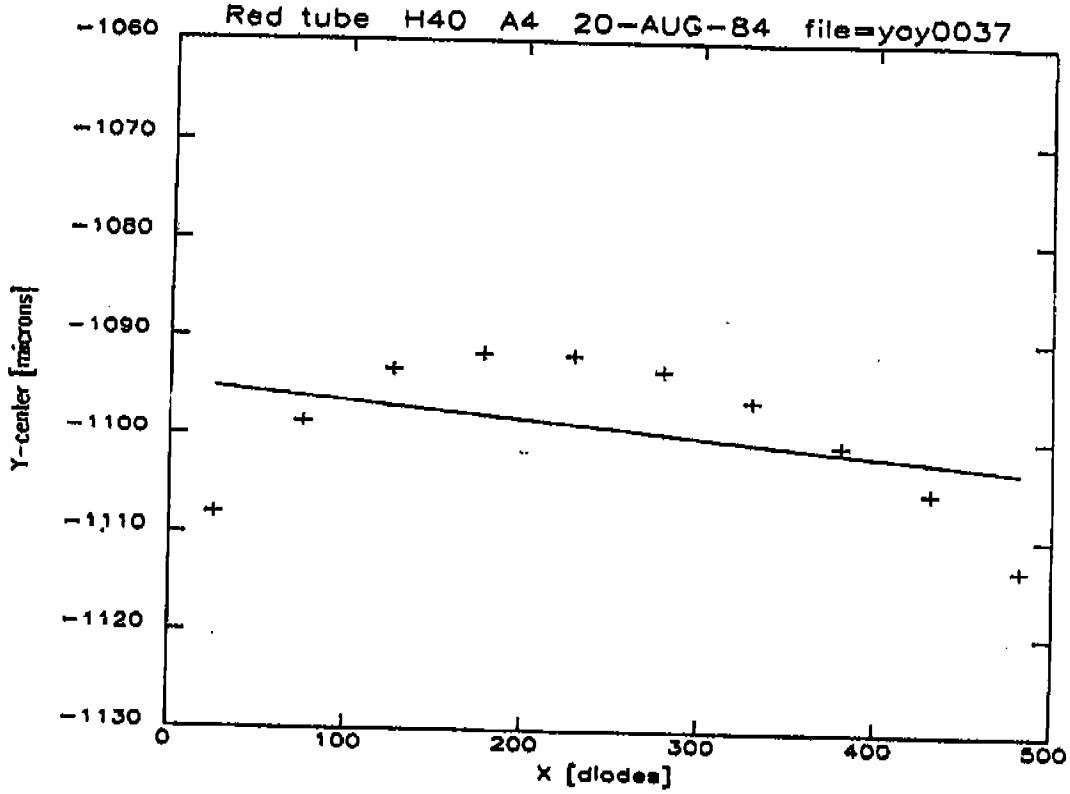

Figure 6.3.2.1-1. Y-center as a function of diode for red tube H40, ambient calibration, 21 kv voltage, August 20, 1984. Crosses: the Y-center for each bin. The solid line is the least squares fit.

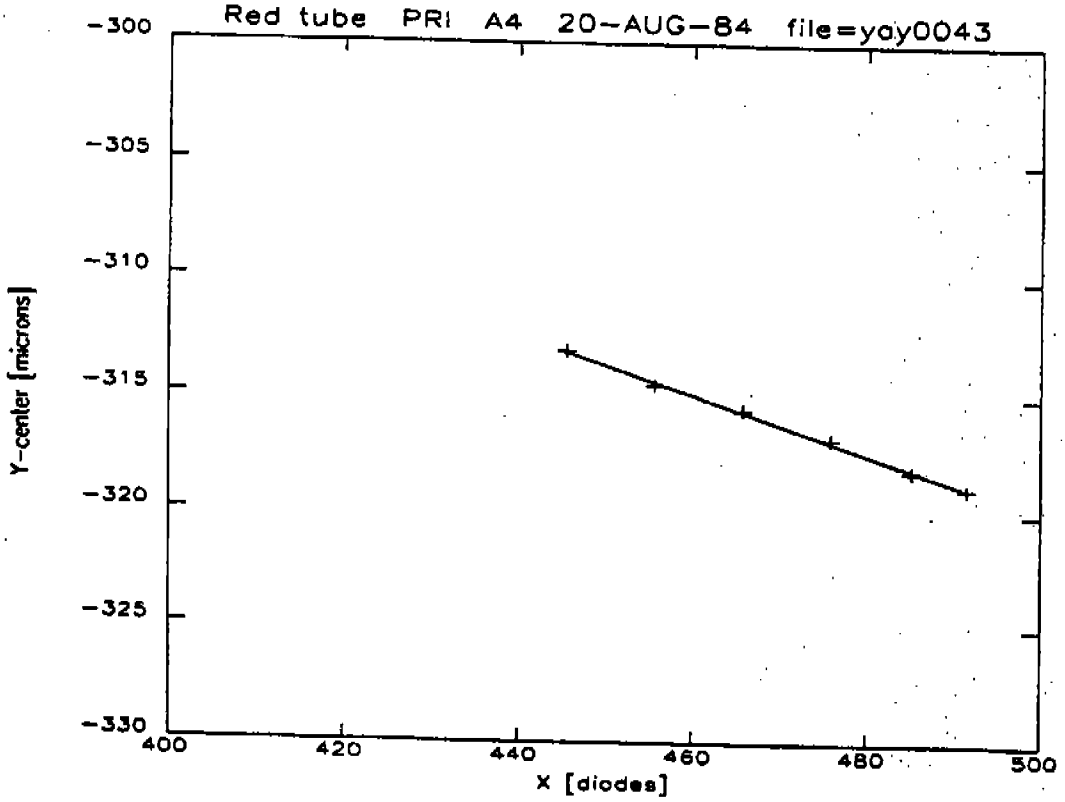

Figure 6.3.2.1-2. Y-center as a function of diode for red tube prism, ambient calibration, 21 kv voltage, August 20, 1984. Note that the X scale is expanded to cover the region from diode 400 to 500 where the prism spectrum is located.

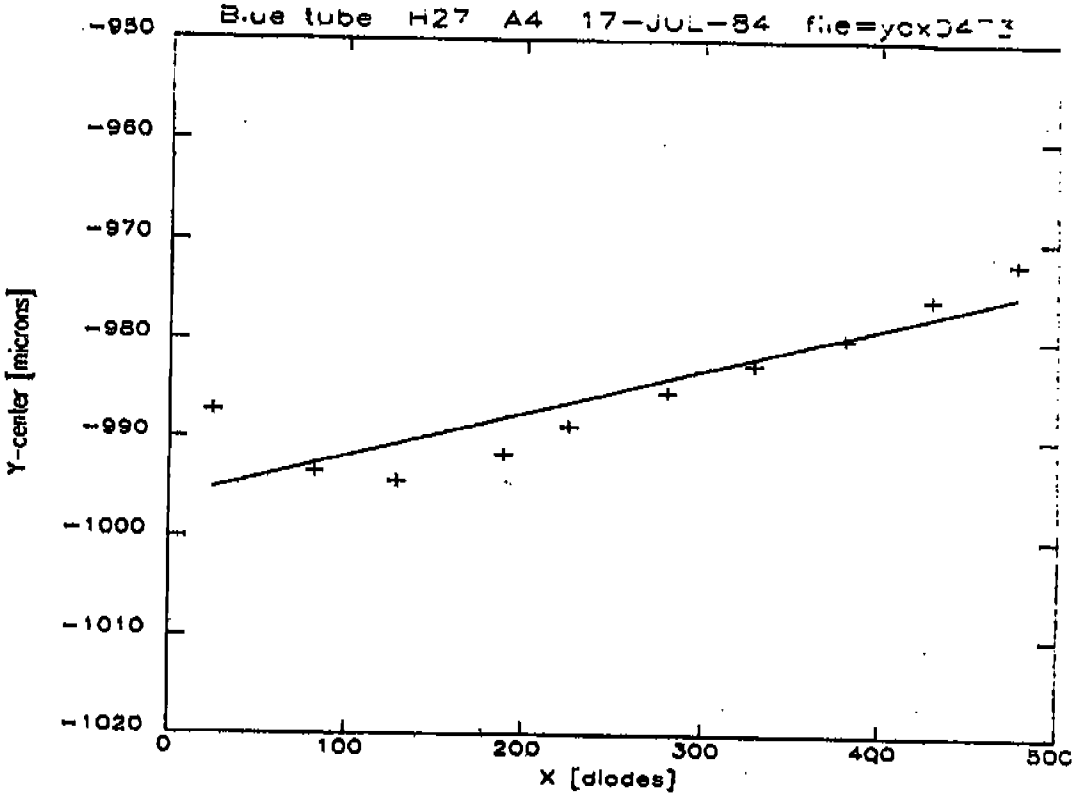

Figure 6.3.2.1-3. Y-center as a function of diode for blue tube H27 vacuum calibration, 23 kv voltage, July 17, 1984.

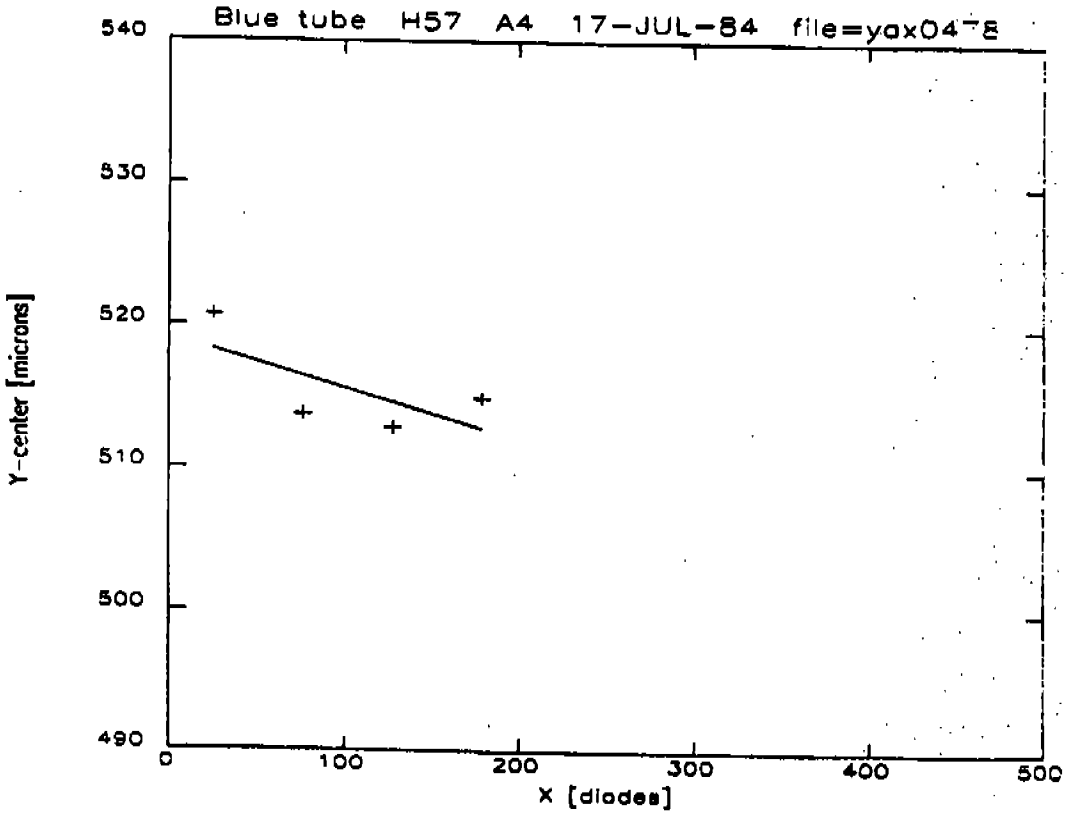

Figure 6.3.2.1-4. Y-center as a function of diode for blue tube H57 vacuum calibration, 23 kv voltage, July 17, 1984. The diode array is only partially covered by the spectrum, because the blue tube attenuates strongly above 5500A.

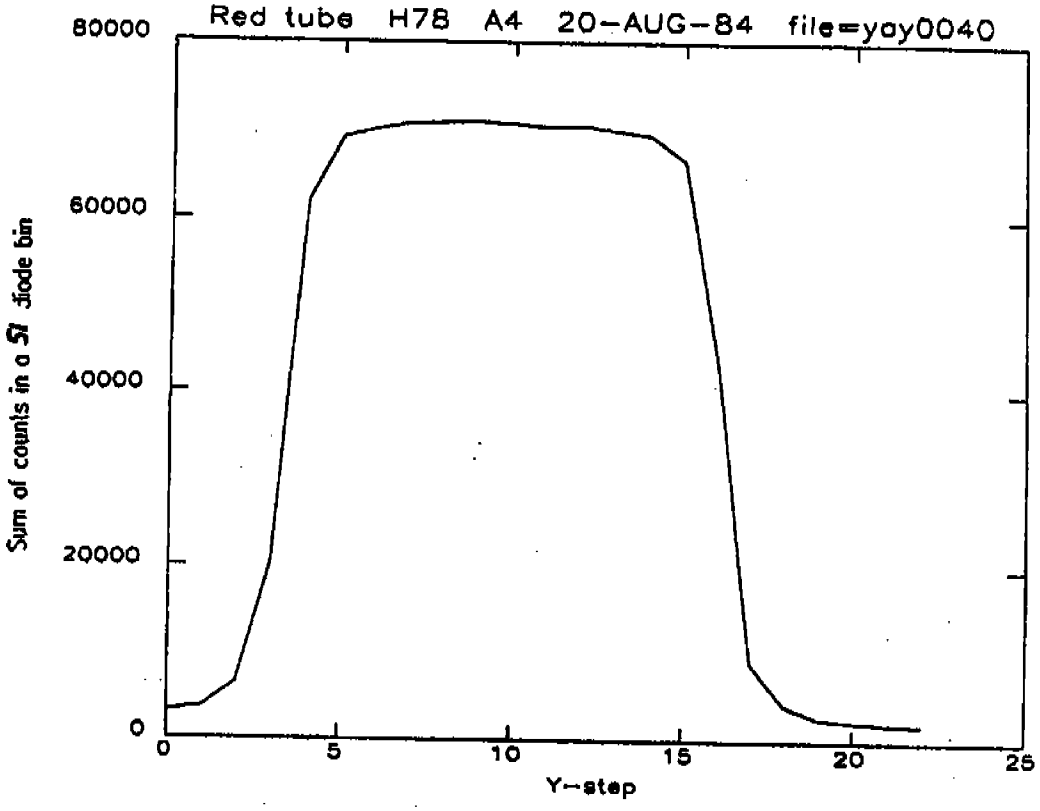

Figure 6.3.2.2-1. Cross-section of the 0.1 arcsec spectrum with a bin size of 50 diodes. The size of the Y-steps is 16 microns.

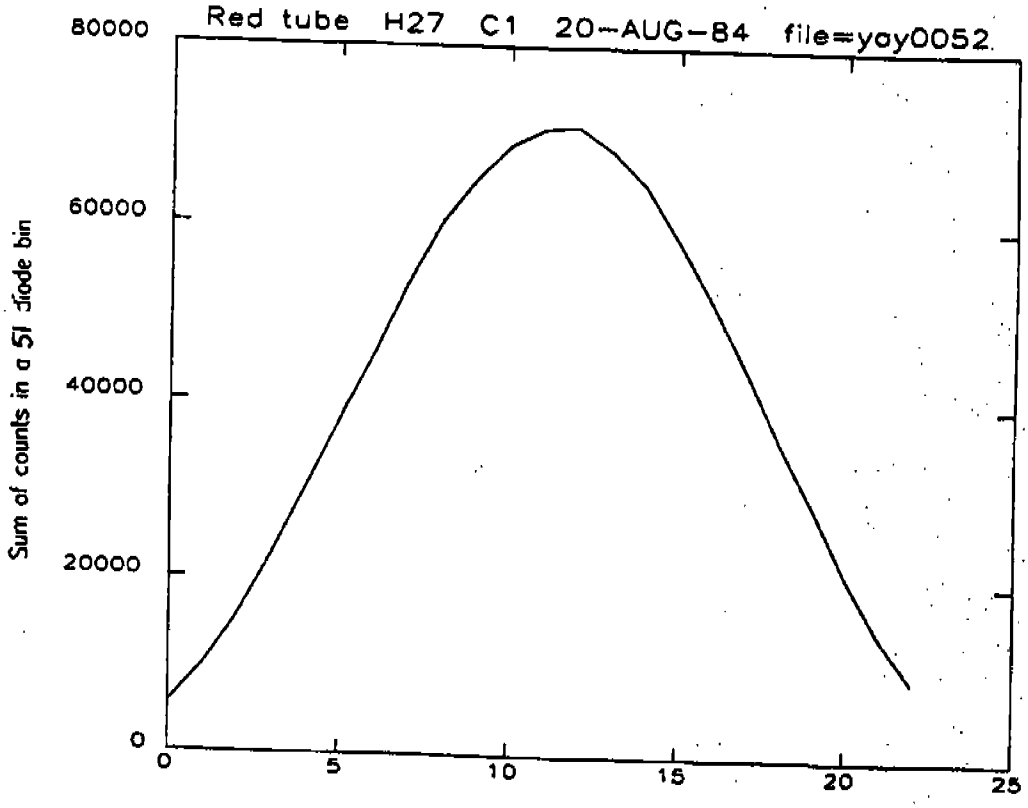

Figure 6.3.2.2-2. Cross-section of an 1.0 arcsec spectrum with a bin size of 50 diodes. The profile is much more rounded than the 0.1 arcsec aperture, because the spectrum is almost as wide as the diode array.

6.3.2.2.1 Cross-Correlation

A square template is cross-correlated with the Y cross-section to determine the point of best correlation which defines the center of the spectrum. In order to improve the counting statistics, the spectra are summed in 51 diode bins, resulting in 10 data points per spectrum in X. The bin size is a compromise between the need to produce smooth cross-sections in regions of the spectrum with few emission lines, and the need for enough data points in X to measure the curvature adequately. The effective center of each bin depends on the distribution of spectral lines within it. The bin center is calculated with a centroid in X:

$$\bar{X} = \frac{\sum X_i \, C_i}{\sum C_i}$$

where x_i are the diode numbers and c_i the corresponding count rates.

To simplify template fitting, each Y cross-section is normalized to its peak. Only two template widths are necessary to accomodate all the aperture sizes, because for apertures one arcsec and smaller the FWHM is determined by the 1.43 arcsec (200 micron) diode height. The remaining three apertures are 2 arcsec wide in the Y-direction, producing 280 micron cross-sections. A quadratic fit is made to the three points at the peak of the correlation curve to determine the center of the spectrum. The algorithm is the same as that used to determine the line centers in the FOS wavelength calibration.

This method produces satisfactory results when the number of counts in the peak of the cross-section is greater than 200. Results for bins with fewer than this number of counts are not included in the Y-center plots. This is particularly important for the low resolution and prism dispersers where the spectrum is confined to a small portion of the diode array.

6.3.2.2.2 Centroiding

The centroiding method is simpler and computationally faster than cross-correlation, but has two major drawbacks: (1) the Y-center is easily thrown off by noise due to poor counting statistics in the cross-section; and (2) centroiding produces incorrect results when a Y-map is truncated, which is often the case in the existing calibration data. A cross-section consists of a set of Y-positions y_i and the corresponding count rates c_i. The centroid in Y is then:

$$\bar{Y} = \frac{\sum y_i C_i}{\sum C_i}$$

The truncation problem can usually be alleviated by centroiding only those data points which are above the half-maximum of the cross-sections. The Y-maps are rarely truncated more than this. There is no correction for the errors produced by poor counting statistics in Y-cross-sections, so this method is not considered suitable for general use.

6.3.2.2.3 Contour Averaging

Contour averaging in effect computes the Y-positions of the upper and lower edges of the spectrum, then averages them to find the center. In this method, the contour lines at intensities of

.2, .4, .6, and .8 are computed for a Y-map where each Y cross-section has been normalized to its peak. The contours for a continuum spectrum are shown in Figure 6.3.2.2.3-1. The average of the Y-positions of matching contour lines gives the center of the spectrum in Y along the diode array. Increasing the number of contours in the average does not result in more accurate Y-centers, because the additional contours are interpolated between the same data points in the cross-section.

Contour averaging uses only the data in two or three Y-steps at the upper and lower edges of the spectrum. The cross-correlation method is also influenced mainly by the points at the edges of the spectrum, because that is where the difference between the template and the spectrum cross-section is greatest. Thus, the two methods are quite similar for high signal-to-noise data. Indeed, the two methods agree to within 2 microns (one-eighth the Y-step size), which is remarkably good agreement considering the 200 micron resolution of the Y-maps. The main drawback to contour averaging is that it does not work well on noisy cross-sections, because linear interpolation is used to calculate the contours, and interpolation does not produce satisfactory results on non-monotonic functions. Therefore, cross-correlation is preferred over the contouring technique, since cross-correlation gives more precise results with low count-rate data.

6.3.2.3 Y-Base and Theta-Z Measurements

Numerous Y-base and theta-Z measurements were made during the vacuum calibration of July 1984 and the ambient calibrations of June and August 1984. The vacuum Y-maps were made with the

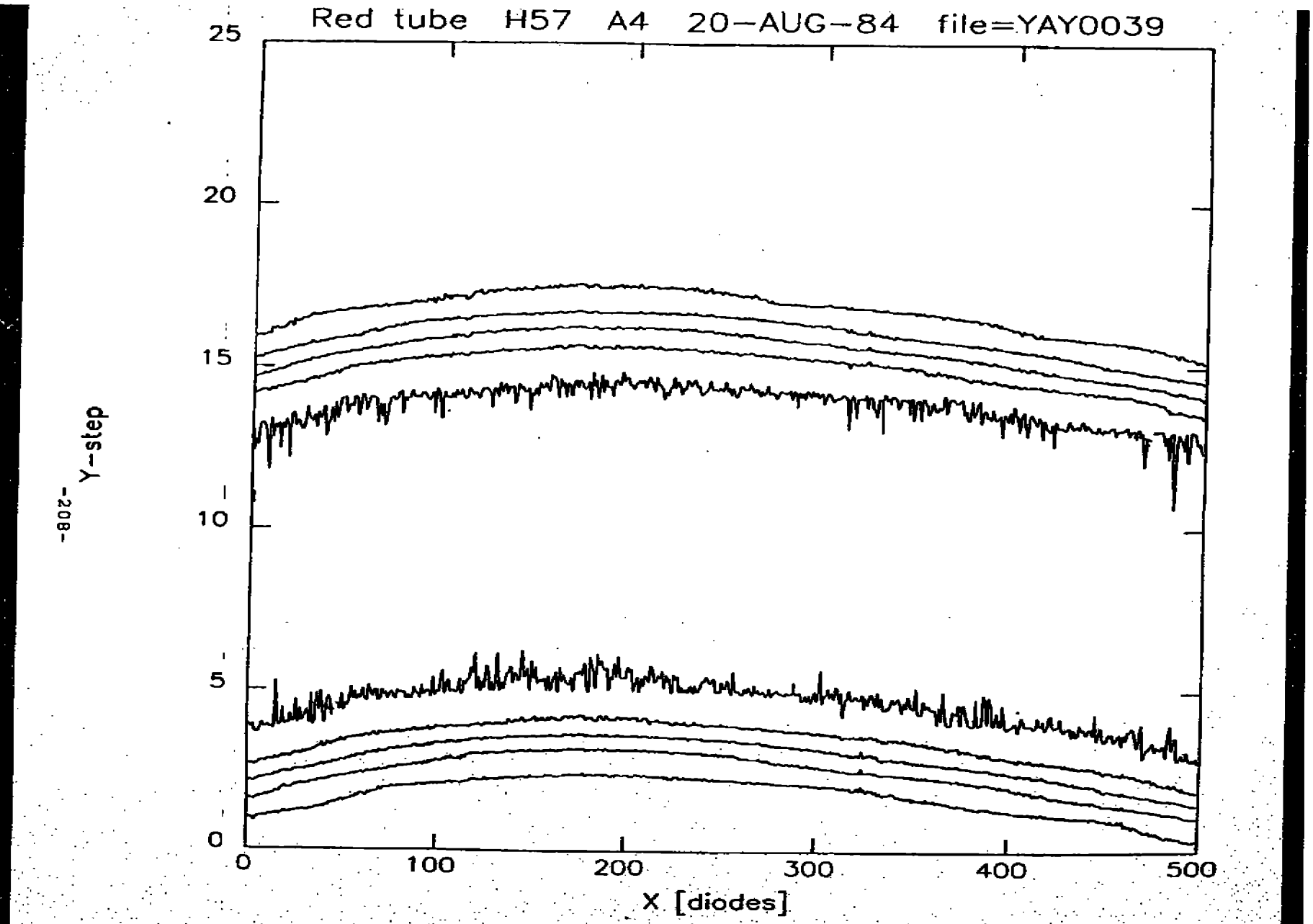

Figure 6.3.2.2.3-1. A contour plot of a normalized Y-map of a continuum spectrum, clearly showing the curvature produced by the red Digicon. The con-

Pt-Cr-Ne emission line lamp, while the ambient Y-maps use the Tungsten and Deuterium external continuum lamps. The spectra were corrected for paired pulse effects with the constants $t_1 = -0.17 \times 10^{-6}$ and $t_2 = 10.5 \times 10^{-6}$ seconds. All Y-base measurements taken since the removal and replacement of the Digicons in the spring of 1984 are summarized in Table 6.3.2.3-1. The range referred to in this table is the total variation in Y-center across the diode array, which is affected both by theta-Z and the amount of distortion. The FOS file-name listed in sixth column consists of a three letter tape designation followed by the number of the file. Files on a given tape are numbered consecutively, e.g., file YAA0001 is the first file on tape YAA. Not all consecutive files were recorded without filter-grating wheel movement. The scatter in the Y-base values due to the filter-grating wheel repeatability is discussed by Hartig, Bohlin, and Harms in CAL/FOS-012 and by Hartig in CAL/FOS-017.

The value of theta-Z is highly dependent on where the endpoints of the spectrum are chosen for the low dispersion modes with short spectra, and for high dispersion modes with partial coverage (H19, H78 Red and H13, H57 Blue). For example, on H57 blue, the theta-Z derived from the first 200 diodes is $-0.^{o}035$ compared with $+0.^{o}035$ if fainter spectral lines out to diode 350 are used. However, the calculated Y-bases differed by only three microns. Because the faint lines are not detected in short exposures, the endpoint of the spectrum was set at diode 200. The typical error in the determination of theta-Z is .01 degrees for gratings that utilize the entire diode array, and 0.5 degrees

where theta-Z is calculated from fewer data points. The Y-base values are accurate to better than 5 microns in all cases. Since the Y-base depends on where the endpoints are chosen, the endpoints of the spectra used to compute theta-Z are listed in Table 6.3.2.1-1. Exposure time may also affect the measured value of theta-Z. Underexposure may result in the loss of fainter spectral lines at the ends of a spectrum. To avoid this, we recommend using the optimum exposure times for the .01 arcsec aperture listed in Table 6.3.2.1-1.

6.3.2.4 Shifts Due to Changes in Temperature and Digicon Voltage

The Y-base and theta-Z measurements were examined to investigate whether systematic shifts occurred between data taken at different temperatures. There are three temperatures to be considered: cold operate in vacuum at -30°C, hot operate in vacuum at -10°C, and ambient calibration at 20°C. All observations at a given temperature were averaged in this analysis. On the red tube, there was no systematic shift in Y-base due to temperature: the mean Y-base shift between cold operate and ambient was -17 microns with a standard deviation of 34 microns. However, the red tube did show a systematic change in theta-Z of .052 $\pm$ .012 degrees between cold operate and ambient. The blue tube showed a systematic shift in Y-base of -61 $\pm$ 31 microns between cold operate and ambient, but the blue side theta-Z did not show a systematic shift: the mean was shift -.004 $\pm$ .026 degrees. The offsets due to changes in temperature are listed in Tables 6.3.2.4-1 and 6.3.2.4-2.

Table 6.3.2.3-1

Y-BASE AND THETA-Z MEASUREMENTS

GRATING	APERTURE	Y-BASE (microns)	RANGE IN Y (microns)	THETA-Z (degrees)	FILE	MAX CTS
RED TUBE, AMBIENT, 22 JUNE 1984, TEMP=ROOM, V=18KV, TUNGSTEN LAMP						
H27	A4	315	22	-0.032	YAQ0097	1372
H27	A4U	751	24	-0.045	YAQ0098	1270
H40	A4	-1122	25	-0.023	YAQ0076	1076
H40	A4	-1122	25	-0.022	YAQ0077	1090
H40	A4U	-687	24	-0.020	YAQ0078	680
H40	A4U	-681	21	-0.014	YAQ0079	675
H40	A4U	-698	23	-0.021	YAQ0080	685
H57	A4	-1313	32	-0.052	YAQ0082	2567
H57	A4	-1313	32	-0.051	YAQ0083	551
H57	A4	-1281	27	-0.043	YAQ0090	1320
H57	A4	-1281	31	-0.049	YAQ0091	1137
H57	A4	-1298	32	-0.051	YAQ0092	1074
H57	A4	-1297	32	-0.051	YAQ0093	1072
H57	A4U	-863	31	-0.049	YAQ0094	1011
H57	B2	-1105	31	-0.050	YAQ0107	5876
H78	A4U	626	21	0.006	YAQ0087	1376
H78	A4	186	21	0.006	YAQ0088	2262
H78	A4	186	20	0.004	YAQ0089	1125
L65	A4	-361	37	0.23	YAQ0099	23350
L65	A4	-360	37	0.24	YAQ0100	4790
L65	A4	-359	37	0.23	YAQ0101	4680
L65	A4U	77	37	0.24	YAQ0102	2930
PRI	A4	-372	5	-0.12	YAQ0104	55158
PRI	A4U	71	7	-0.15	YAQ0105	33629
BLUE TUBE, AMBIENT, 22 JUNE 1984, TEMP=ROOM, V=18KV, TUNGSTEN LAMP						
H40	A2	544	31	0.086	YAR0022	1349
H57	A4	585	10	0.039	YAR0023	597
L65	A4	-203	26	0.21	YAR0024	1172
BLUE TUBE, VACUUM, 11 JULY 1984, TEMP=-30C, V=23KV, PLATINUM LAMP						
H13	A4	-249	13	-0.037	YAT1896	1427
H13	A4	-249	15	-0.039	YAT1897	1437
H13	A4	-261	17	-0.044	YAT1898	1053

Table 6.3.2.3-1 Cont'd

GRATING	APERTURE	Y-BASE (microns)	RANGE IN Y (microns)	THETA-Z (degrees)	FILE	MAX CTS
BLUE TUBE, VACUUM, 11 JULY 1984, TEMP=-30C, V=23KV, PLATINUM LAMP						
H19	A4	-536	19	0.088	YAT1876	87
H19	A4	-538	22	0.10	YAT1877	89
H19	A4	-537	24	0.11	YAT1878	75
H27	A4	-981	25	0.064	YAT1874	553
H27	A4	-972	25	0.060	YAT1875	527
H40	A4	520	16	0.043	YAT1872	1732
H40	A4	514	19	0.055	YAT1873	1994
H57	A4	556	17	-0.044	YAT1899	1953
L65	A4	-314	24	0.14	YAT1884	1208
L65	A4	-319	34	0.20	YAT1885	1235
L65	A4	-319	29	0.17	YAT1886	1160
L65	A4	-267	25	0.15	YAT1890	1203
L65	A4	-283	29	0.18	YAT1894	1182
PRI	A4	-390	6	-0.11	YAT1887	1774
PRI	A4	-393	5	-0.09	YAT1888	2023
PRI	A4	-341	2	-0.01	YAT1892	2061
PRI	A4	-351	3	-0.06	YAT1895	2166
RED TUBE, VACUUM, 15 JULY 1984, TEMP=-30C, V=21KV, PLATINUM LAMP						
H19	A4	-218	33	-0.077	YAX0020	2854
H19	A4U	216	35	-0.083	YAX0021	2405
H27	A4	316	48	-0.11	YAX0022	10950
H40	A4	-1112	36	-0.082	YAX0025	6948
H57	A4	-1207	45	-0.10	YAX0028	31335
H78	A4U	567	18	-0.058	YAX0029	14333
L15	A4	-121	9	-0.10	YAX0030	400
BLUE TUBE, VACUUM, 17 JULY 1984, TEMP=-10C, V=23kV, PLATINUM LAMP						
H13	A4U	+214	19	-0.040	YAX0467	7300
H19	A4	-514	28	0.070	YAX0474	3500
H19	A4	-499	28	0.064	YAX0488	80
H19	A2	-501	25	0.067	YAX0486	2500
H19	C1	-501	25	0.063	YAX0489	7000

Table 6.3.2.3-1 Cont'd

GRATING	APERTURE	Y-BASE (microns)	RANGE IN Y (microns)	THETA-Z (degrees)	FILE	MAX CTS
BLUE TUBE, VACUUM, 17 JULY 1984, TEMP=-10C, V=23kV, PLATINUM LAMP						
H19	B2	-289	25	0.067	YAX0481	2097
H19	B3	-287	25	0.066	YAX0482	6209
H19	A2	-501	26	0.065	YAX0486	2602
H19	A3	-502	32	0.074	YAX0487	1995
H19	C1	-501	24	0.063	YAX0489	7027
H19	C2	-300	27	0.065	YAX0490	3743
H27	A4	-985	22	0.050	YAX0473	18000
H40	A4	507	16	0.037	YAX0476	25000
H40	A4	500	15	0.034	YAX0500	4007
H40	A4U	923	16	0.037	YAX0499	4152
H40	C1	499	15	0.038	YAX0496	31903
H40	C1	499	14	0.037	YAX0497	31994
H40	C1	920	14	0.036	YAX0498	31684
H40	A3	497	15	0.040	YAX0501	14087
H40	A3U	916	15	0.036	YAX0502	13928
H40	A2U	920	15	0.037	YAX0503	10385
H40	A2	503	15	0.039	YAX0504	10436
H40	B3	714	15	0.038	YAX0505	28848
H40	B2	711	16	0.042	YAX0506	9852
H40	B1	714	15	0.039	YAX0507	9719
H57	A4	515	9	-0.043	YAX0475	20000
L15	A4U	+6	2	0.008	YAX0469	2000
L65	A4	-274	21	0.22	YAX0471	24000
RED TUBE, VACUUM, 17 JULY 1984, TEMP=-10C, V=21KV, PLATINUM LAMP						
H19	A4	-212	32	-.073	YAX0522	2600
H27	A4	+342	42	-.094	YAX0523	30000

Table 6.3.2.3-1 Cont'd

GRATING	APERTURE	Y-BASE (microns)	RANGE IN Y (microns)	THETA-Z (degrees)	FILE	MAX CTS
BLUE TUBE, VACUUM, 20 JULY 1984, TEMP=-10C, V=23KV, PLATINUM LAMP						
H13	A4	-222	16	-0.094	YAX0902	274
H13	A4U	201	18	-0.11	YAX0903	324
H13	A4	-234	20	-0.12	YAX0920	246
H13	A4U	184	13	-0.081	YAX0921	271
RED TUBE, VACUUM, 20 JULY 1984, TEMP=-10C, V=21KV, PLATINUM LAMP						
H78	A4	151	37	-0.12	YAX0907	9898
H78	A4	169	25	-0.078	YAX0908	9338
H78	A4U	606	22	-0.072	YAX0909	6698
RED TUBE, AMBIENT, 20-21 AUGUST 1984, TEMP=ROOM, V=21kV, TUNGSTEN LAMP						
H19	C1	-260	33	-0.044	YAY0064	323
H19	C3	-40	27	-0.032	YAY0062	643
H19	B3	-57	26	-0.035	YAY0065	248
H27	A4	289	32	-0.056	YAY0047	351
H27	A4U	714	30	-0.052	YAY0036	250
H27	A2	290	32	-0.056	YAY0045	6181
H27	A3	290	32	-0.057	YAY0046	1480
H27	B1	489	31	-0.054	YAY0048	4798
H27	B2	492	30	-0.052	YAY0049	1673
H27	B3	491	31	-0.056	YAY0050	9854
H27	C1	288	33	-0.059	YAY0052	12616
H27	C2	506	31	-0.058	YAY0053	9000
H27	C3	510	29	-0.054	YAY0054	24039
H27	C4	502	34	-0.062	YAY0055	20810
H40	A4	-1099	20	-0.020	YAY0037	4500
H57	A4	-1265	32	-0.048	YAY0039	10000
H78	A4	140	23	0.002	YAY0058	11088
H78	A4U	593	23	0.007	YAY0040	7000
H78	A2	140	22	0.002	YAY0056	54946
H78	A3	142	22	0.002	YAY0057	29262
H78	B1	342	21	0.003	YAY0059	41557
H78	B2	344	20	0.001	YAY0060	32906
H78	C2	358	21	0.006	YAY0061	40127
L65	A4	-360	28	0.23	YAY0044	5000
PRI	A4	-317	5	-0.043	YAY0043	60000

Table 6.3.2.3-1 Cont'd

GRATING	APERTURE	Y-BASE (microns)	RANGE IN Y (microns)	THETA-Z (degrees)	FILE	MAX CTS
BLUE TUBE, AMBIENT, 26 AUGUST 1984, TEMP=ROOM, V=23KV, TUNGSTEN LAMP						
H19	C1	-561	31	0.072	YAZ0106	327
H27	A3	-1057	23	0.054	YAZ0107	1128
H40	A4	412	20	0.054	YAZ0108	806
H57	A4	476	7	-0.013	YAZ0109	1130
L65	A4	-336	50	0.16	YAZ0110	2038
PRI	A4	-434	3	-0.040	YAZ0111	1720

The lower half of a paired aperture was used unless otherwise noted with a U for the upper aperture.

Table 6.3.2.4-1

Y-BASE OFFSETS DUE TO CHANGES IN TEMPERATURE

Red Tube , V=21kv, 0.1 arcsec aperture

Grating	Y-base T=-30 (microns)	Y-base T=-10 (microns)	Shift between T=-30 and t=-10 (microns)	Y-base Ambient (microns)	Shift between T=-30 and ambient (microns)
H19	-218	-212	6	-261	-43
H27	316	342	26	289	-27
H40	-1112			-1099	13
H57	-1207			-1265	-52
H78U	567			593	26
					Mean: -17 +/- 34

Blue tube , V=23kv, 0.1 arcsec aperture

Grating	Y-base T=-30	Y-base T=-10	Shift between T=-30 and t=-10	Y-base Ambient	Shift between T=-30 and ambient
H19	-537	-514	23	-561	-24
H27	-977	-985	-8	-1057	-80
H40	517	507	-10	412	-105
H57	556	516	-40	477	-79
L65	-300	-274	44	-336	-36
PRI	-390			-434	-44
			Mean: 2 +/-32		Mean: -61 +/- 31

Table 6.3.2.4-2

THETA-Z OFFSETS DUE TO CHANGES IN TEMPERATURE

Red Tube , V=21kv, 0.1 arcsec aperture

Grating	Theta-Z T=-30 (degrees)	Theta-Z T=-10 (degrees)	Shift between T=-30 and t=-10 (degrees)	Theta-Z Ambient (degrees)	Shift between T=-30 and ambient (degrees)
H19	-.077	-.072	.005	-.044	.033
H27	-.109	-.093	.016	-.056	.053
H40	-.082			-.020	.062
H57	-.100			-.048	.052
H78U	-.058	-.043	.015	.007	.065
					Mean: .053 +/- .012

Blue Tube , V=23kv, 0.1 arcsec aperture

Grating	Theta-Z T=-30	Theta-Z T=-10	Shift between T=-30 and t=-10	Theta-Z Ambient	Shift between T=-30 and ambient
H19	.106	.080	-.026	.072	-.034
H27	.062	.050	-.012	.055	-.007
H40	.049	.034	-.015	.054	-.005
H57	-.044	-.043	.001	-.014	.030
			Mean: .013 +/- .011		Mean: -.004 +/- .026

Table 6.3.2.4-3

Y-BASE OFFSETS DUE TO CHANGE IN VOLTAGE

Red Tube, ambient, 0.1 arcsec aperture

Grating	Y-base 18kv (microns)	Y-base 21kv (microns)	Shift between 18kv and 23kv
H27	315	289	-26
H27U	751	714	-37
H40	-1044	-1099	-55
H57	-1226	-1265	-39
H78	188	140	-48
H78U	627	593	-34
			Mean: -40 +/- 10

Blue Tube, ambient, 0.1 arcsec aperture

Grating	Y-base 18kv (microns)	Y-base 23kv (microns)	Shift between 18kv and 23kv
H19	-437	-561	-124
H27	-954	-1057	-103
H40	544	412	-132
H57	585	476	-109
L65	-203	-336	-133
PRI	-295	-434	-139
			Mean: -123 +/- 14

Table 6.3.2.4-4

THETA-Z OFFSETS DUE TO CHANGE IN VOLTAGE

Red Tube, ambient, 0.1 arcsec aperture

Grating	Theta-Z 18kv (degrees)	Theta-Z 21kv (degrees)	Shift between 18kv and 23kv
H27U	-.045	-.052	-.007
H40	-.012	-.020	-.008
H57	-.049	-.048	.001
H78	.006	.002	-.004
H78U	.006	.007	.001
			Mean: .007 +/- .009

Blue Tube, ambient, 0.1 arcsec aperture

Grating	Theta-Z 18kv (degrees)	Theta-Z 23kv (degrees)	Shift between 18kv and 23kv
H40	.086	.054	-.032
H57	.039	-.013	-.052

During the July vacuum calibration and the August ambient calibration, the blue and red Digicons were operated at 23 and 21 kV, respectively. However, in the June ambient calibration, data was obtained at 18 kV for both detectors. Both detectors showed systematic decreases in Y-base values with increased voltage. The mean Y-base shift for the red tube between the June and August calibrations was -40 $\pm$ 10 microns. The blue tube Y-base measurements from June are only available on tape for gratings H40, H57, and L65. This data was supplemented by Y-base values calculated in FOS Calibration Notebook 3 for gratings H19, H27, and the prism. The mean shift for these six dispersers is -123 $\pm$ 14 microns. When Y-base values from the FOS notebook are compared to those calculated from the data tapes by the method discussed here, the results agree to within 5 microns. Theta-Z did not shift systematically with voltage on the red tube: the mean shift was .007 $\pm$ .009 degrees. Theta-Z comparisons between 18 and 23 kV are available for only two gratings on the blue tube. The shift on H40 was -.032 degrees, and -.052 degrees on H57. Theta-Z comparisons were made using only those gratings with full spectral coverage. The offset due to changes in voltage are shown in Tables 6.3.2.4-3 and 6.3.2.4-4.

6.3.2.5 Mean Point Source Cross-Section

The main interest in FOS photometric precision is for stellar point sources, which are adequately approximated by the fully illuminated 0.1 arcsec aperture. The mean cross-section of an FOS spectrum taken with the 0.1 arcsec aperture was computed by averaging ten cross-sections from one spectrum on each detector,

Each cross-section is the sum of the counts in a 50-diode bin. The cross-sections were normalized to their peaks, and then interpolated on a one micron grid. The center of each cross-section was determined by cross-correlation, and the interpolated cross-sections were then centered and summed to produce the mean curve. The H78 Y-map in file YAY0040 was chosen for the red tube cross-section, because it was one of the few that was not truncated, and yet had sufficient counts for one percent accuracy. The H40 Y-map in file YAX0501 was used for the blue tube cross-section. The FWHM is 206.0 Y-base units (equivalent to microns to within 10%) for the blue curve and 206.3 Y-base units for the red curve. The mean cross-sections are tabulated in Tables 6.3.2.5-1 and 6.3.2.5-2, and plotted in Figures 6.3.2.5-1 and 6.3.2.5-2, where Y-base units and microns are used interchangeably, even though Y-base units are only approximately equivalent to microns.

6.3.2.6 Mean Reduced Locus of Y-Centers

The average Y-center as a function of diode number in an FOS spectrum was determined for each detector. The effect of the different orientation (theta-Z) of each grating was removed by computing the deviation of the Y-center from the best fit line for each grating. The results for the three fully covered gratings on each side (Blue - H19, H27, H40; Red - H27, H40, H57) were shifted to zero Y-base and averaged to obtain the final curves, illustrated in Figures 6.3.2.6-1 and 6.3.2.6-2, and listed in Table 6.3.2.6-1.

Table 6.3.2.5-1

BLUE TUBE MEAN POINT SOURCE CROSS-SECTION

Y (MICRONS)	INTENSITY
-150.00	4.13142E-02
-145.00	4.49599E-02
-140.00	5.01553E-02
-135.00	5.93092E-02
-130.00	7.07596E-02
-125.00	9.03191E-02
-120.00	0.13048
-115.00	0.18436
-110.00	0.27366
-105.00	0.43243
-100.00	0.60533
-95.000	0.77064
-90.000	0.86509
-85.000	0.92411
-80.000	0.96145
-75.000	0.97578
-70.000	0.98225
-65.000	0.98720
-60.000	0.99058
-55.000	0.99310
-50.000	0.99531
-45.000	0.99691
-40.000	0.99758
-35.000	0.99803
-30.000	0.99833
-25.000	0.99826
-20.000	0.99798
-15.000	0.99768
-10.000	0.99816
-5.0000	0.99905

Y (MICRONS)	INTENSITY
0.0000	1.0000
5.0000	0.99989
10.000	0.99887
15.000	0.99739
20.000	0.99590
25.000	0.99490
35.000	0.99354
40.000	0.99268
45.000	0.99170
50.000	0.99061
55.000	0.98852
60.000	0.98574
65.000	0.98217
70.000	0.97501
75.000	0.96533
80.000	0.95167
85.000	0.91036
90.000	0.83798
95.000	0.74179
100.00	0.59572
105.00	0.42942
110.00	0.27304
115.00	0.16328
120.00	0.11605
125.00	8.39821E-02
130.00	6.39523E-02
135.00	5.40057E-02
140.00	4.62675E-02
145.00	4.02842E-02
150.00	3.75334E-02

Table 6.3.2.5-2

BLUE TUBE MEAN POINT SOURCE CROSS-SECTION

Y (MICRONS)	INTENSITY
-150.00	2.18572E-02
-145.00	3.04461E-02
-140.00	4.27927E-02
-135.00	5.86833E-02
-130.00	8.58453E-02
-125.00	0.12515
-120.00	0.17348
-115.00	0.25360
-110.00	0.35851
-105.00	0.47012
-100.00	0.58599
-95.000	0.69565
-90.000	0.79401
-85.000	0.87521
-80.000	0.92664
-75.000	0.95811
-70.000	0.97718
-65.000	0.98364
-60.000	0.98824
-55.000	0.99301
-50.000	0.99483
-45.000	0.99521
-40.000	0.99533
-35.000	0.99587
-30.000	0.99640
-25.000	0.99654
-20.000	0.99667
-15.000	0.99705
-10.000	0.99779
-5.0000	0.99879

Y (MICRONS)	INTENSITY
0.00000E+00	1.0000
5.0000	1.0015
10.000	1.0026
15.000	1.0027
20.000	1.0016
25.000	1.0008
30.000	1.0003
35.000	0.99978
40.000	0.99926
45.000	0.99859
50.000	0.99881
55.000	0.99912
60.000	0.99734
65.000	0.99160
70.000	0.98287
75.000	0.96440
80.000	0.92870
85.000	0.87436
90.000	0.80381
95.000	0.70301
100.00	0.58684
105.00	0.46980
110.00	0.36138
115.00	0.26733
120.00	0.18314
125.00	0.12813
130.00	9.20825E-02
135.00	6.49018E-02
140.00	4.71736E-02
145.00	3.67673E-02

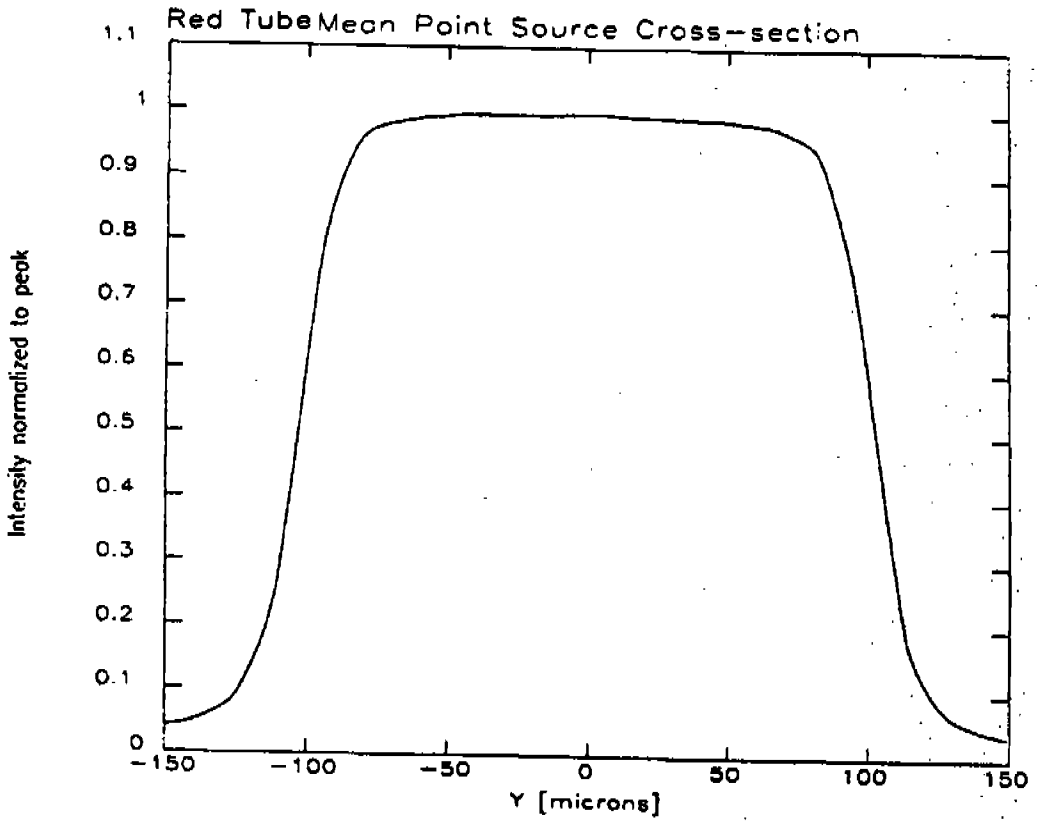

Figure 6.3.2.5-1. Mean cross-sections of a point source spectrum as represented by a 0.1 arcsec aperture spectrum with the red and blue detectors. This cross-section should adequately represent the actual cross-section for a point source in any FOS aperture.

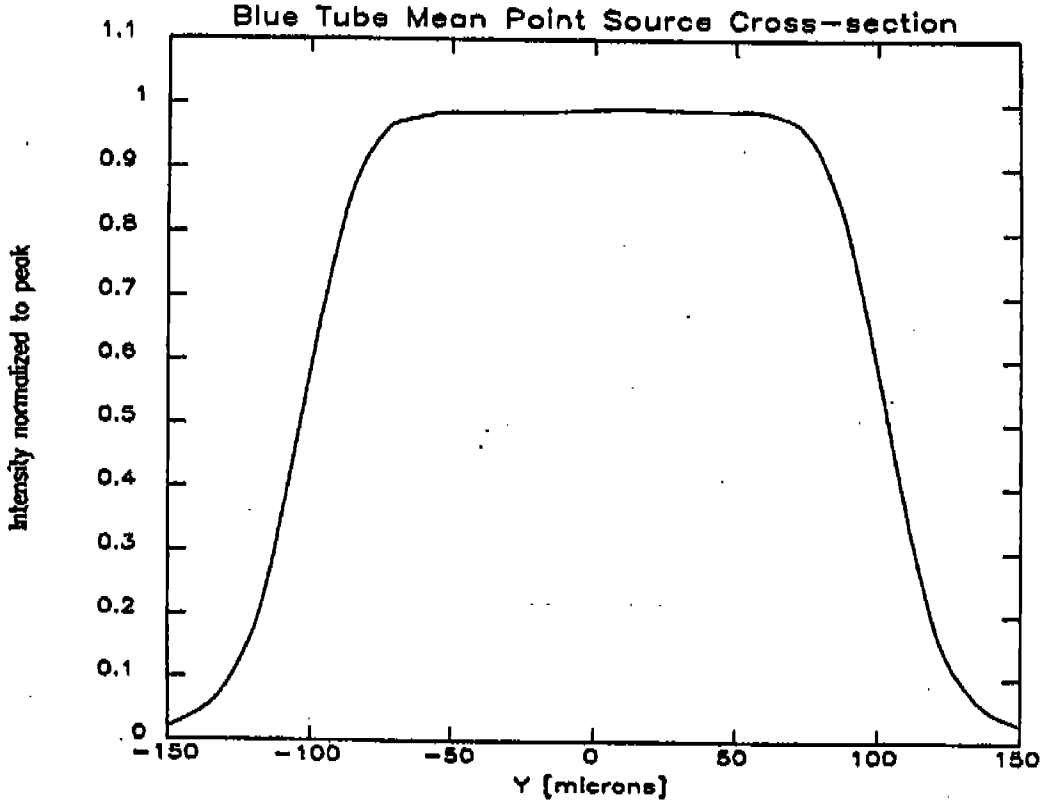

Figure 6.3.2.5-2. Mean cross-sections of a point source spectrum as represented by a 0.1 arcsec aperture spectrum with the red and blue detectors. This cross-section should adequately represent the actual cross-section for a point source in any FOS aperture.

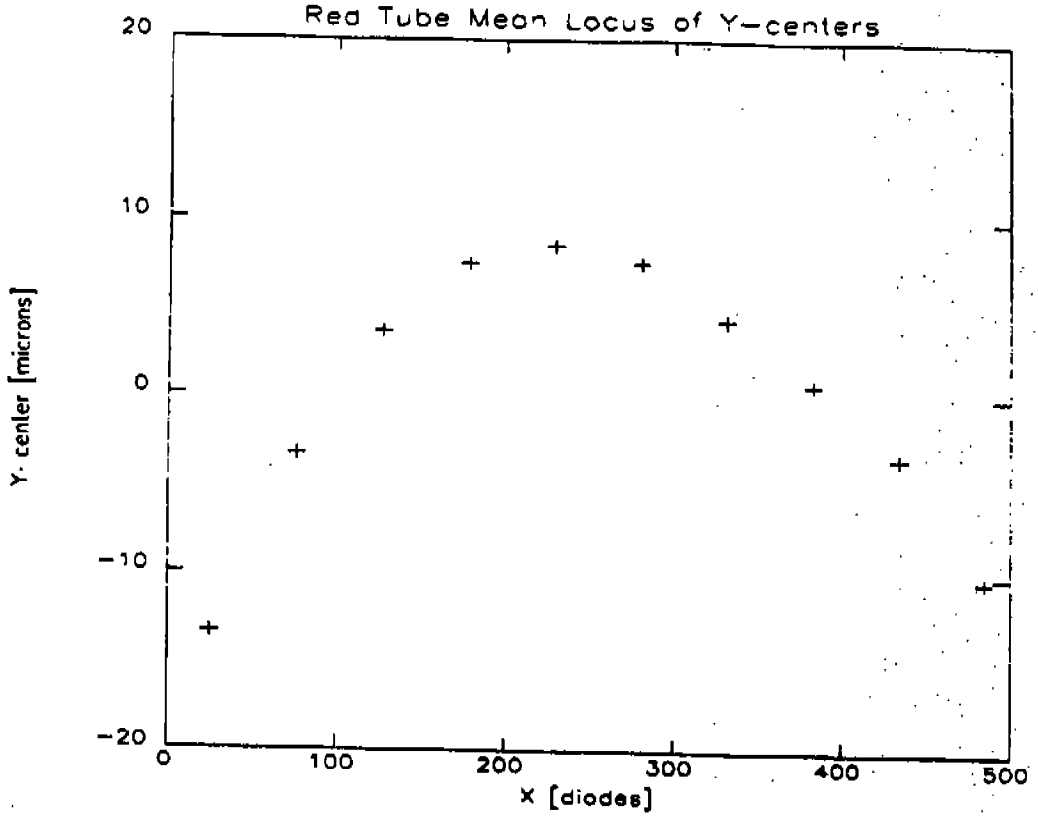

Figure 6.3.2.6-1. Mean Y-center as a function of diode for each detector. The curve has been reduced to zero theta-Z and zero Y-base.

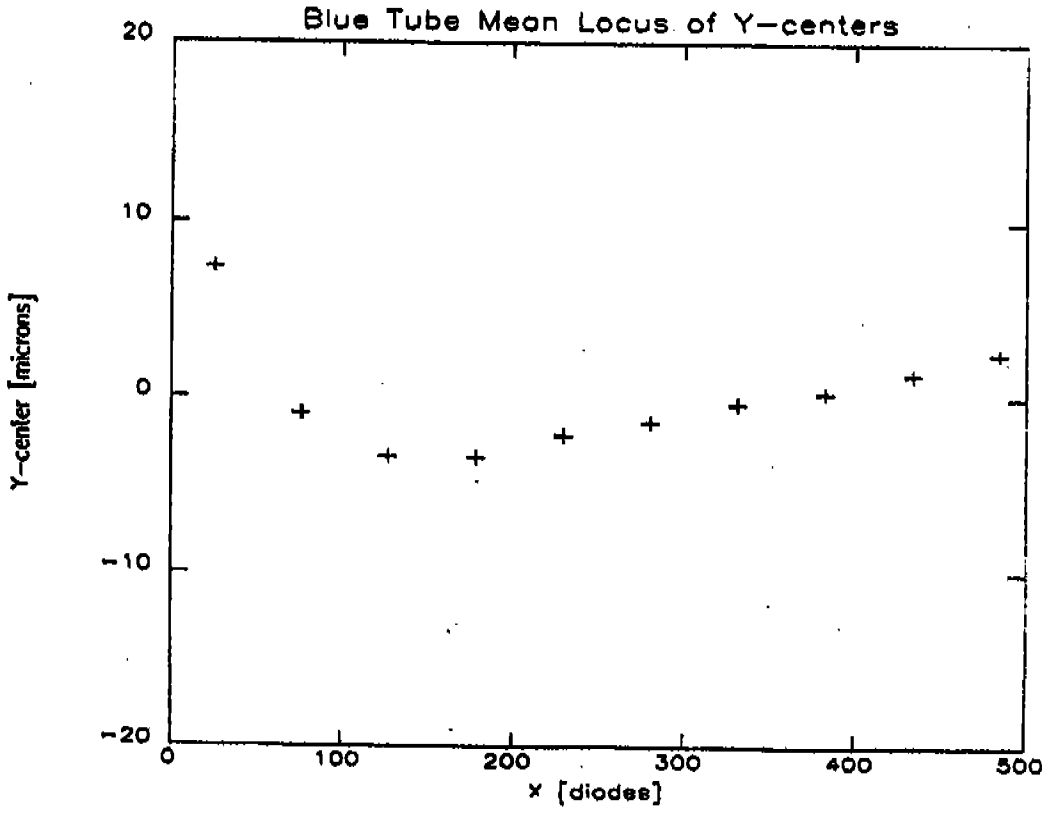

Figure 6.3.2.6-2. Mean Y-center as a function of diode for each detector. The curve has been reduced to zero theta-Z and zero Y-base.

Table 6.3.2.6-1

MEAN LOCUS OF Y-CENTERS

BLUE TUBE DIODE	Y-CENTER (MICRONS)
25.	7.5
76.	-0.9
127.	-3.4
178.	-3.4
229.	-2.2
280.	-1.4
331.	-0.3
382.	0.3
433.	1.3
484.	2.5

RED TUBE DIODE	Y-CENTER (MICRONS)
25.	-13.3
76.	-3.3
127.	3.6
178.	7.5
229.	8.5
280.	7.5
331.	4.3
382.	0.7
433.	-3.4
484.	-10.2

6.3.3 Photometric Consequences of Positioning Errors (Observed)

The photometric consequences of positioning errors must be investigated separately for each combination of detector, grating, and aperture, because theta-Z is different for each grating. Because the locus of Y-centers is not symmetric in Y, a positive Y-base error has a different effect than a negative Y-base error of the same magnitude.

Ideally, we would like to directly measure the light loss, from ground-based calibration data obtained in vacuum. Unfortunately, the existing internal Pt-Cr-Ne emission line spectra in Y-maps simply do not have enough counts to determine the light loss to better than 3-5%. A typical light loss curve derived from an emission line spectrum is shown in Figure 6.3.3-1, illustrating that the curves are noisy and of little use. Some of the continuum spectra taken in ambient calibrations have adequate counting statistics, but because theta-Z changes with temperature, the ambient light loss curves cannot be used to predict the performance of the FOS in vacuum. However, it is possible to predict light loss curves from the mean locus of Y-centers, the mean spectrum cross-section, and the Y-base and theta-Z values measured in vacuum.

Light-loss curves obtained from ambient continuum spectra can be used to check whether the calculated light loss agrees with the observations. The raw data for the light loss measurements are the same Y-maps used for the Y-base measurements. The Y-maps are summed in 50 diode bins, to improve counting statistics. The spectrum at the nominal Y-base is linearly interpo-

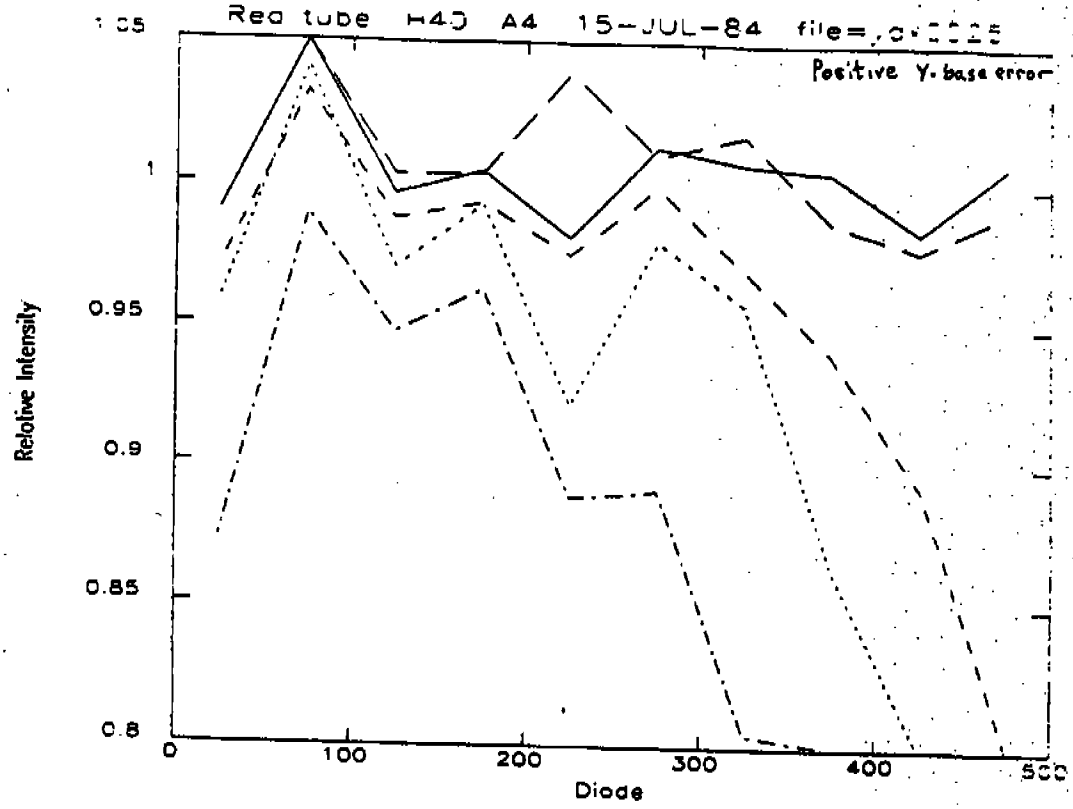

Figure 6.3.3-1. The effects of error in Y-position as a function of diode number determined from an emission line spectrum on the red tube. The upper plot is for positive Y-base errors, the lower plot for negative Y-base errors. The two plots differ because the locus of Y-centers is not symmetric. The five curves represent errors of 30 microns (solid line), 50 microns (long dash), 70 microns (medium dash), 80 microns (short dash), and 90 microns (dot-dash). The error in the curves is at the 5% level.

Figure 6.3.3-1 Cont'd

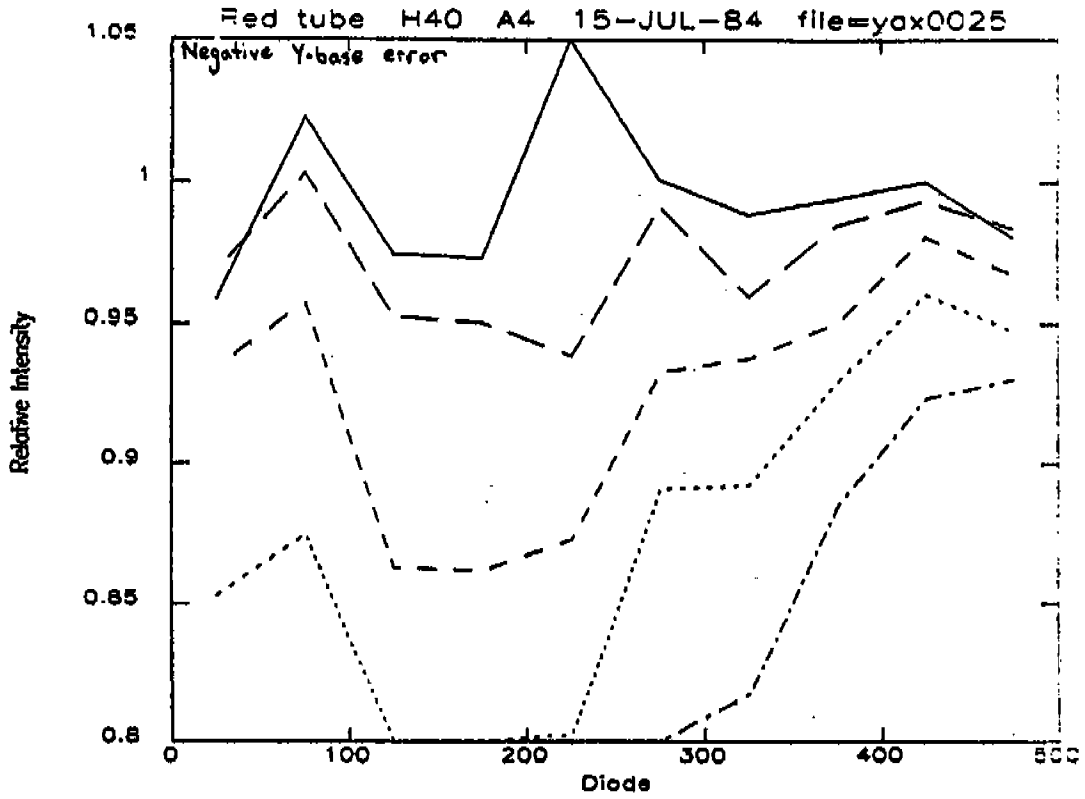

lated between the Y-steps of the Y-map, where necessary. Similarly, the spectra at offsets of 30, 50, 70, 80, and 90 microns above and below the nominal Y-base are also interpolated. Each light-loss curve at a given offset is simply the binned spectrum at the offset divided by the binned spectrum at the nominal Y-base. Examples of these observed light loss curves are presented in Figures 6.3.3-2 through 6.3.3-4.

6.3.4 Photometric Consequences of Positioning Errors (Modeled)

Computer models of the photometric consequences of errors in Y-base positions are being developed at the STScI using the (ever-improving) FOS computer simulation. Dr. Ralph Bohlin will provide the results as an update to this section.

6.4 Pulse Coincidence Correction

6.4.1 Channel Deadtime - The two 512 channel FOS sensors are multichannel photon counting detectors. Each of the separate 1024 channels has a 10.5 microsecond dead time circuit. That is, upon arrival of a channel event, that electronic channel is digitally gated off for 10.5 microseconds. This technique forces each channel to have the same input to output counting characteristic.

6.4.2 Pulse Pair Calibration - The vital first element of the FOS calibration effort is the accurate removal of this digicon electronics nonlinear pulse counting characteristic. We assume the standard formula:

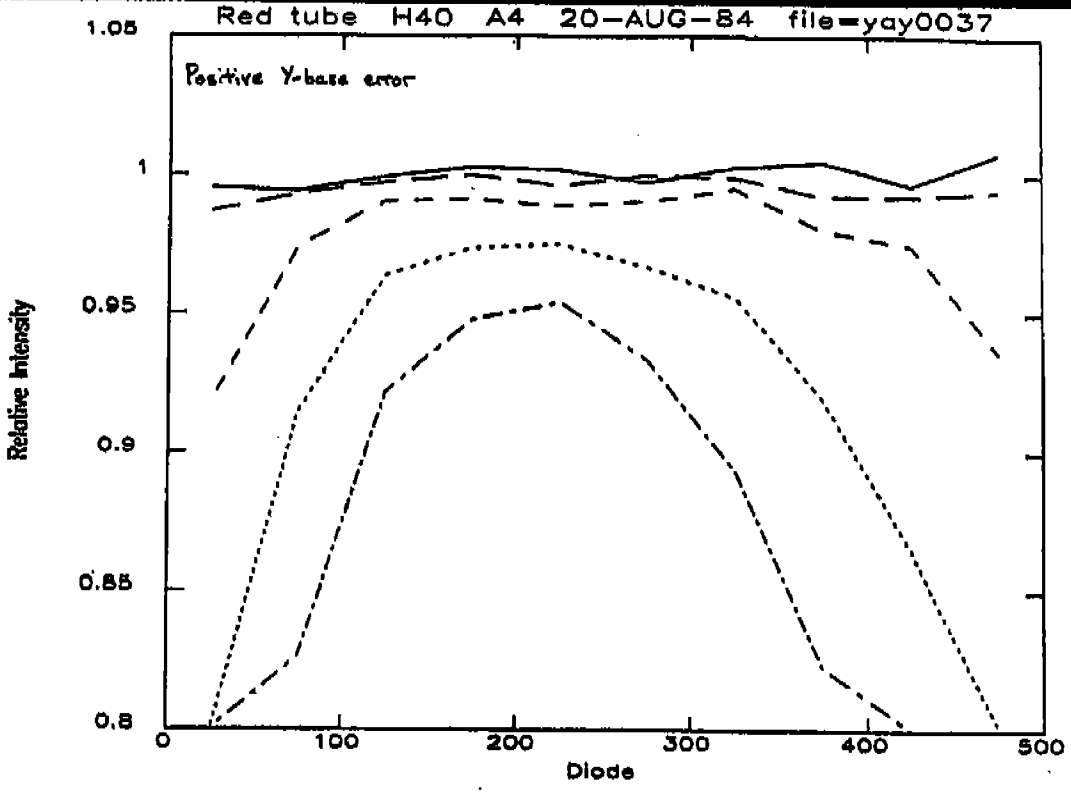

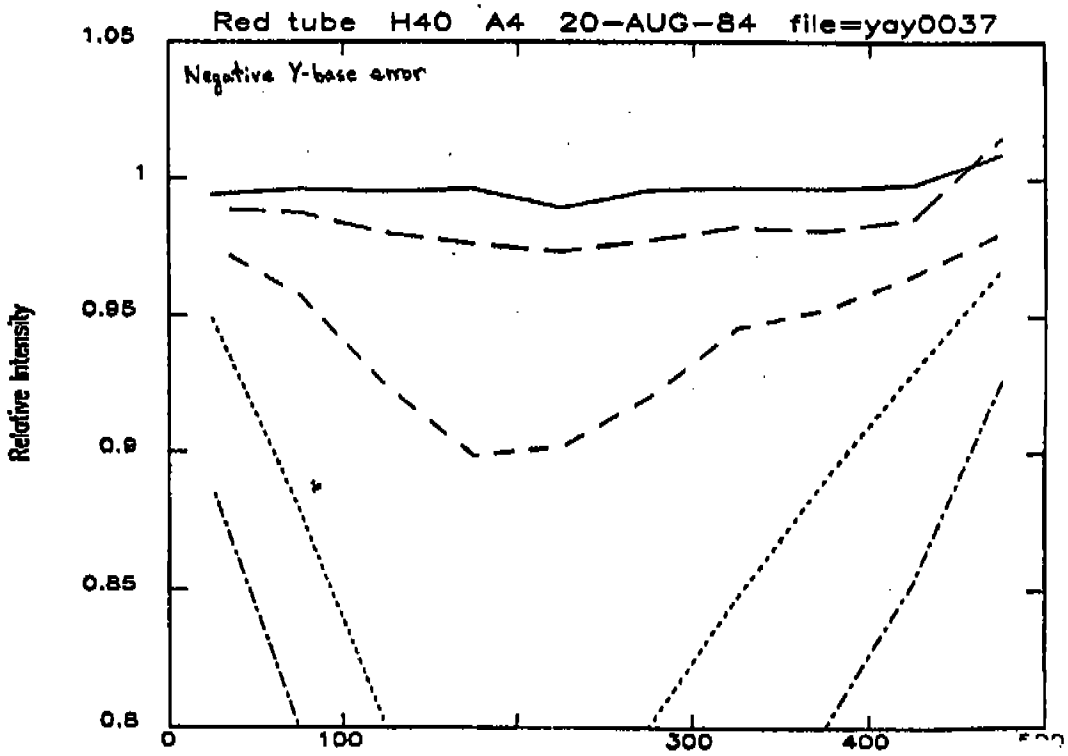

Figure 6.3.3-2. The effects of error in Y-position from continuum spectra on the red tube. The lines are coded as in Figure 6.3.3-1. The noise level is 1-2%, because the total counts per bin is higher than that of the emission line spectra.

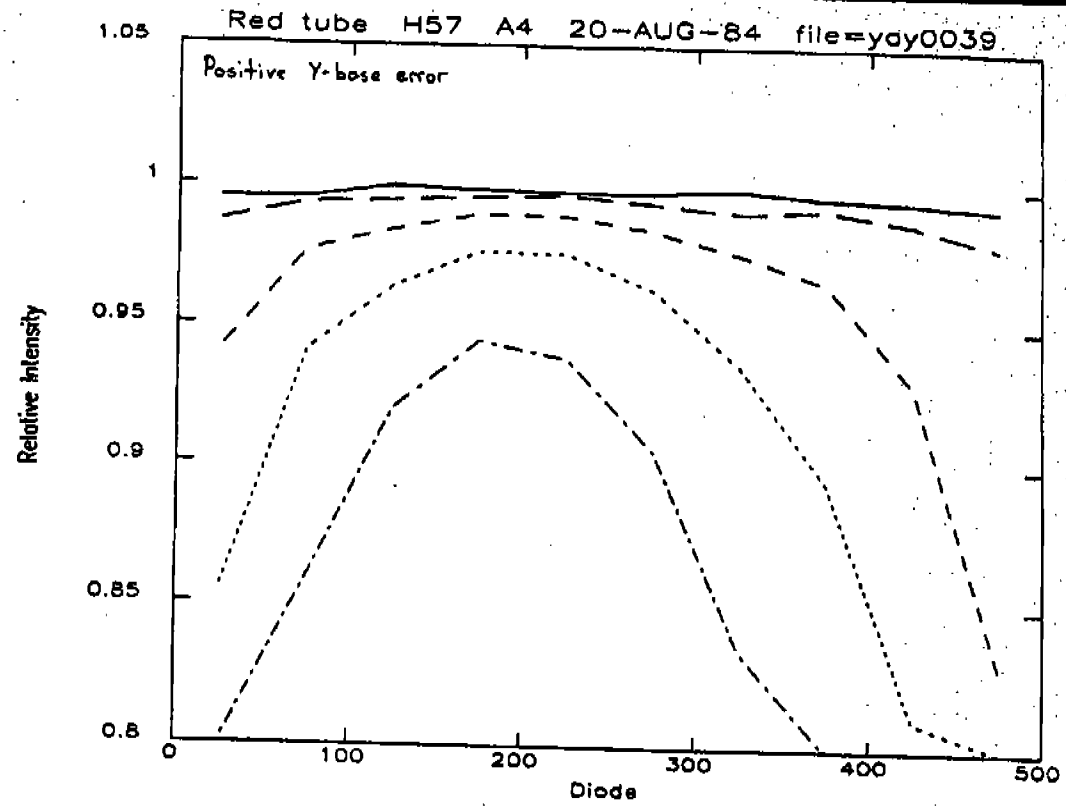

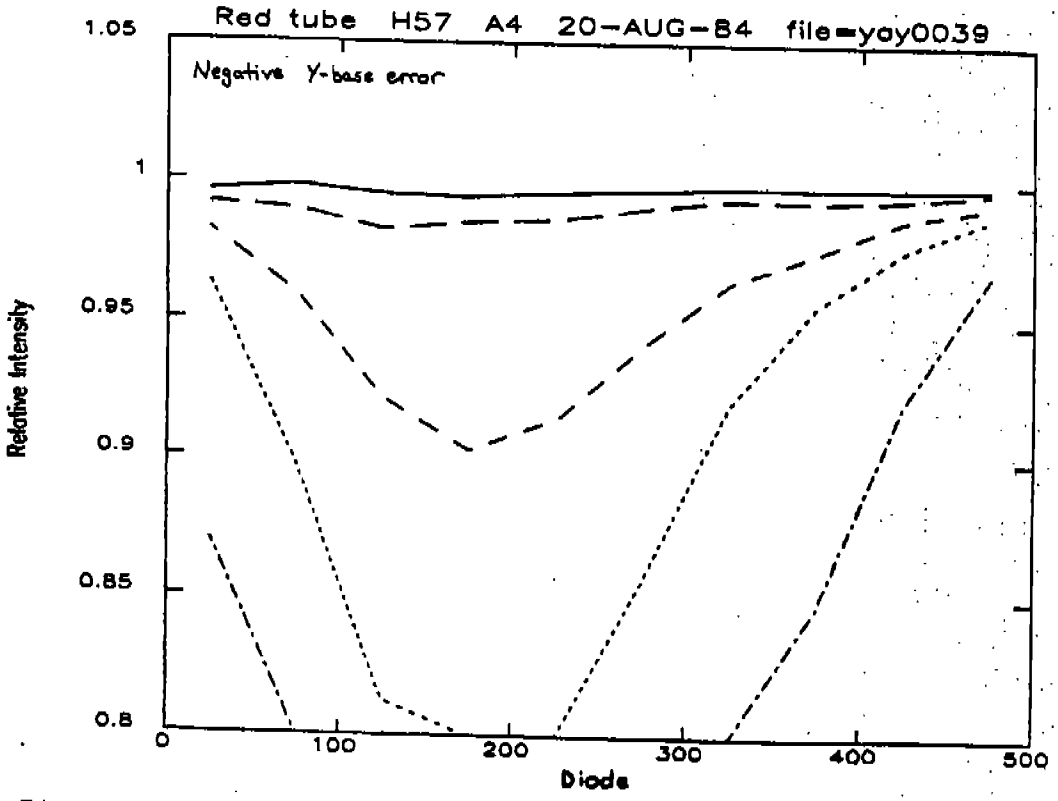

Figure 6.3.3-3. The effects of error in Y-position from continuum spectra on the red tube. The lines are coded as in Figure 6.3.3-1. The noise level is 1-2%, because the total counts per bin is higher than that of the emission line spectra.

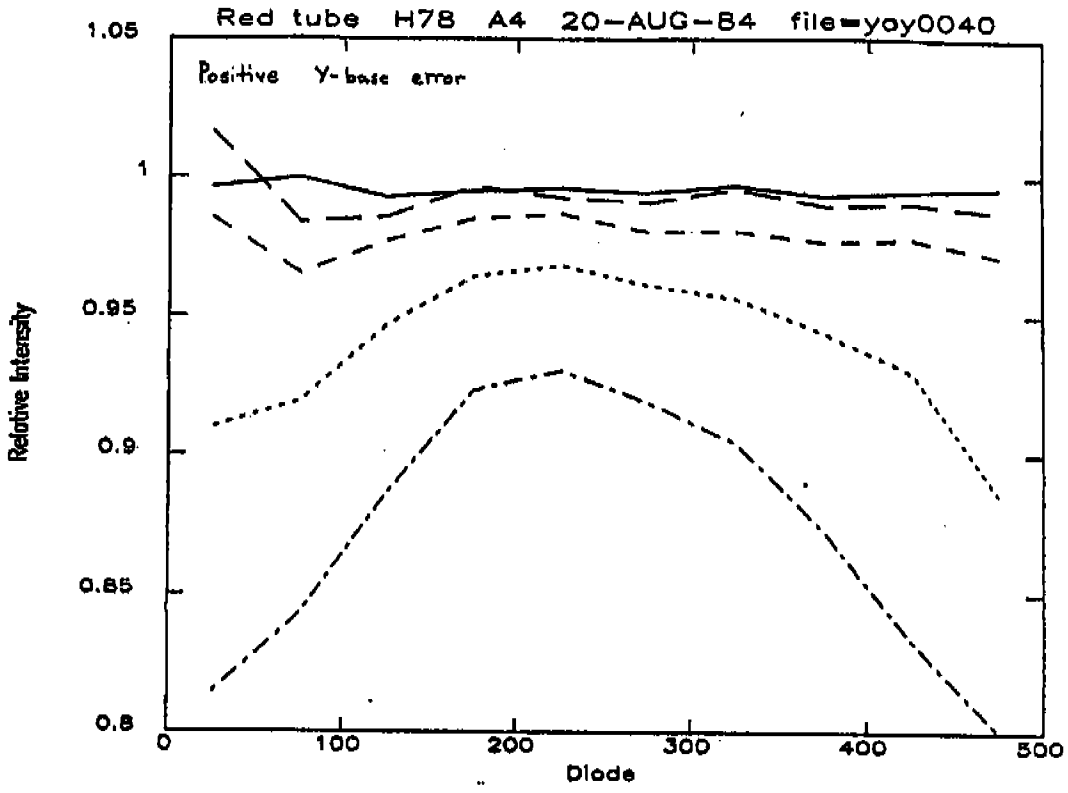

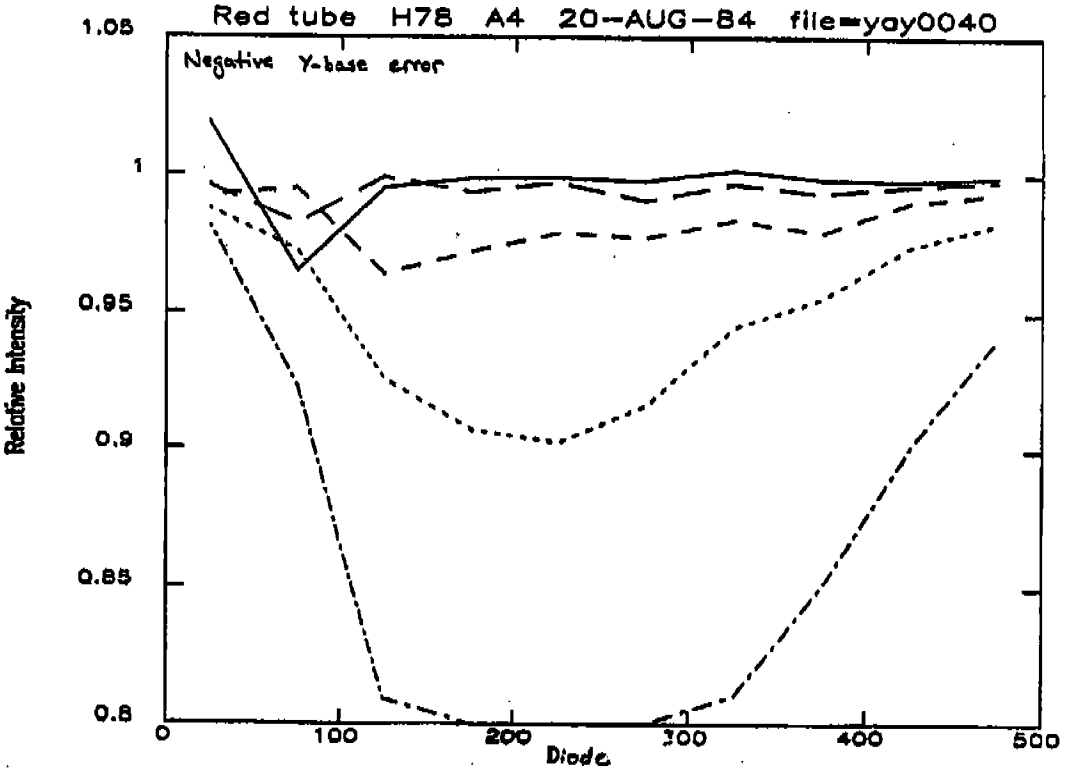

Figure 6.3.3-4. The effects of error in Y-position from continuum spectra on the red tube. The lines are coded as in Figure 6.3.3-1. The noise level is 1-2%, because the total counts per bin is higher than that of the emission line spectra.

$$Y = \frac{X \exp(-t_1 X)}{1 + t_2 X \exp(-t_1 X)} \qquad (6.4.1)$$

where X --> true input count rate
Y --> apparent output count rate
t --> recovery time
t --> dead time

Pulse paired correction calibration involves the optimum determination of t_1 and t_2 and assessing the accuracy of the standard formula (6.4.1) to correctly linearize digicon data.

6.4.3 FOS Counting Data - During FOS calibration, the input light rate was varied over a range of three magnitudes by sequencing through the 11 separate apertures. Table 6.4-1 gives the relative ratio of the various apertures to the B1 aperture. The ambient STOS serves as the constant light input to the FOS apertures.

The FOS calibration data is plotted in Figure 6.4-1. The continuous curve in Figure 6.4-1 is a least squares fit of Equation (6.4.1) to the data, assuming t_2 = 10.5 μs. The optimum value of t_1 is -0.17 μs. Except for real counting rates $X > 10^5$ counts/sec, the fit is excellent, as displayed in Figure 6.4-2. The FOS maximum counting requirement is 10^5 counts/sec. Any deviations from the dominant t_2 = 10.5 μs dead time can be attributed to errors in the aperture sizing at this accuracy level.

6.4.4 Procedure for Pulse Pair Calibration - For input rates below 10^5 counts/sec, Equation (6.4.1) can be used to establish the true count rate.

In practice, we have implemented pulse pair calibration by a procedure involving interpolation of a look up table. This also

TABLE 6.4-1

Aperture	Relative Size (Aperture/B1)
A4*	0.111
A3	0.898
B2	1.00
B1	3.19
A2	4.07
C2	6.03
B3	13.4
C4	14.3
C1	17.0
C3	42.3
A1	104.1

*Results from this aperture have not been considered, since effective size is difficult to measure due to diffraction effects.

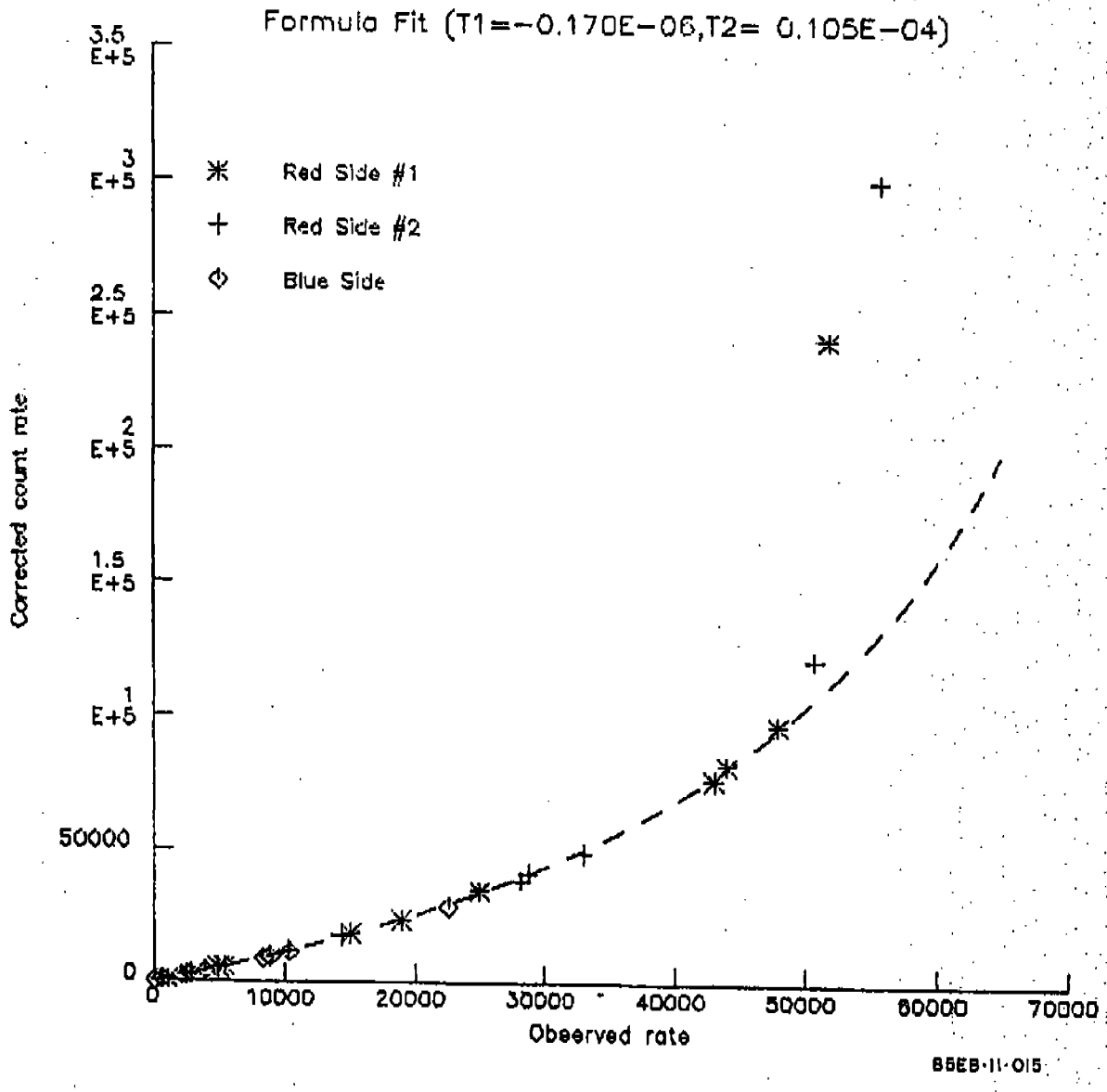
Formula Fit (T1=-0.170E-06,T2= 0.105E-04)
Red Side #1
Red Side #2
Blue Side
Corrected count rate
Observed rate
3.5 E+5
3 E+5
2.5 E+5
2 E+5
1.5 E+5
1 E+5
50000
0
10000
20000
30000
40000
50000
60000
70000
85EB-11-015

FIGURE 6.4-1

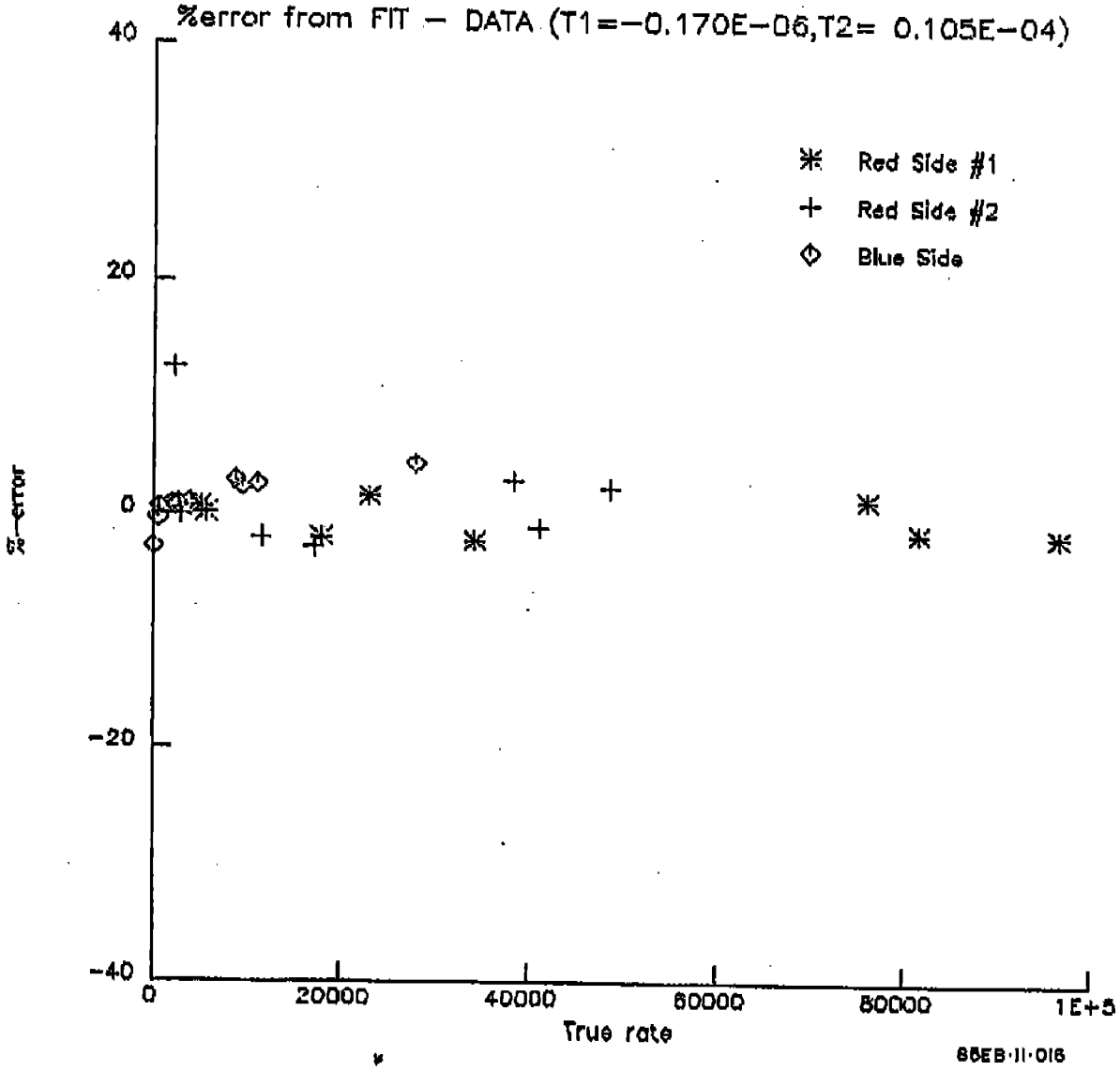
%error from FIT − DATA (T1=−0.170E−06,T2= 0.105E−04)
Red Side #1
Red Side #2
Blue Side
40
20
0
-20
-40
% error
0
20000
40000
60000
80000
1E+5
True rate
85EB-11-016

FIGURE 6.4-2

allows for pulse pair calibration at input rates X > 10^6 counts/sec, where Equation (6.4.1) does not apply.

6.5 Background

6.5.1 Dark Count Rate

A series of tests have been conducted with the FOS flight and spare detectors, during various stages of fabrication and assembly, and under a variety of environmental operating conditions.

At the simplest level, dark count data were obtained for samples of various diodes, near the desired operating voltage, for all digicon phototubes built at EVSD. These data represented a portion of the overall tube data used for the selection of the best tubes for flight. The data were obtained at an operating temperature of approximately -10°C, where the dark count spec (0.002 counts/sec/diode) must be verified. A sample of such data are included here.

At the next level, the digicon tubes are encapsulated, wired, and fully integrated into a single operating unit which incorporates the structural, thermal, and HV interfaces along with the permanent magnets, the deflection coils, and the charge amplifier hybrid boards.

Dark count data were obtained with these fully assembled flight detectors to verify the dark count specification compliance at this integration stage. A description of the test set up, operating conditions, and sample results are also included here.

Finally at the systems level, where the detector assemblies are integrated with all other operating components of the FOS, dark count data were obtained to demonstrate systems specification compliance. These data were obtained under a wide variety of operating conditions and environments, primarily during ambient calibration and Thermal Vacuum Cycling and Thermal Vacuum UV calibration of the FOS. Again, samples of these test data are described and included here to illustrate systems level compliance with the specifications.

Overall, the test program at all levels demonstrates that the FOS does indeed perform at very low noise levels, well within its performance specifications.

6.5.1.1 Digicon Dark Count Data

Test data were obtained by Electron Vision Systems Division (EVSD) for the digicon vacuum phototubes upon completion of their fabrication. Sample test data were obtained for selected diodes, deflected to various photocathode locations. These data are shown in Figure 6.5.1.1-1 and were obtained with an operating voltage of 22 kV at a temperature of -11°C. The integration time interval was 1000 sec. This data sheet is for flight tube F-7, and represents the basic information to screen out problem tubes. In the example shown, the average dark count is seen to be approximately 0.001 counts/sec/diode, within the acceptable specification level of 0.002 counts/sec/diode.

6.5.1.2 Detector Assembly Level Dark Count Measurements

These tests were performed in a Tenney Model T5-110250 Thermal Chamber. All measurements were made at ambient (room)

AT-3010

BACKGROUND COUNT RATE

Data Sheet

Tube S/N: FOS # F-7

Test Conditions: Tube Temperature -10°C.

Photocathode Voltage 22 KV

BACKGROUND COUNTS PER 1000 SEC PER DIODE

Average Over Entire Field .00123 @ -11°C HV off = .0008

(Specification Limit = 2 Max.) { .0051 @ +15°C
.0042 @ H.V off

Y Position (mm)

	Diode #	1	59	105	159	209	259	311	359	405	459	509
1* -X	+3.5	1	6	0	1	0	1	0	1	2	1	3
	0	2	2	5	2	1	2	3	2	1	0	1
	-3.5	0	0	0	0	2	0	1	1	0	0	2
2** +X	+3.5	2	8	1	1	0	0	0	1	2	1	0
	0	0	2	0	1	0	0	0	0	2	2	0
	-3.5	1	6	0	1	0	4	0	1	0	0	2
	HV Off	1	5	0	0	0	2	0	0	0	0	1
	***"Room" Temp.	5	10	5	11	6	5	1	6	4	3	0

*1 Diode #1 near edge of mask.
**2 Diode #512 near edge of mask.
***3 Temp +15°C.

=> .005 c/... ...@ 15°C

81

Date: 8-3-81 Tester: J Acton Q.A.: SAI QEB 8/6/81

Engineering: J Acton 8/6/81 SAI SDS

FIGURE 6.5.1.1-1

pressure. To maintain a dry environment and to avoid condensation on the detector, the chamber was purged with dry gaseous nitrogen throughout the operation, except for periods of high voltage operation. During high voltage operation, the detector was purged with Sulfur Hexafluoride to minimize the effects of high voltage breakdown in the tube's high stress front end.

The detector was mounted in a Permanent Magnet Focus Assembly (PMFA). An array of "pogo pins" was used to contact the detector's header bumps to the input of the SAI Digicon Test Facility. This facility contains twelve channels of charge sensitive amplifiers, twelve amplifier/discriminators, and a Hewlett-Packard 9845 computer for test control and data preprocessing. A test program in the computer software permits monitoring of all twelve channels simultaneously throughout the 1000 one-second integration periods used for each test. A green LED is included in the test facility to permit illumination of the cathode for aliveness checks. Aliveness checks were made before and after each set of data to verify proper detector and test facility operation.

It should be noted that the discrete charge amplifiers used in these tests, although of the FOS design, are somewhat noisier than the hybrid charge amplifiers used in the flight configuration to be flown on the FOS.

6.5.1.2.1 Digicon F-3 (S-20 Photocathode)

This was the first digicon to be tested. Room temperature baseline dark counts were made, recording four channels distributed across the diode array (some of the pogo pin contacts were

lost during thermal cycling). The average dark count was measured to be approximately 0.3 counts per second per pixel (see Table 6.5.1.2.1-1).

The chamber temperature was decreased to 0°C and the digicon cold soaked a minimum of four hours to permit full thermal stabilization. The average dark count was measured to be approximately 0.01 counts per second per pixel.

The chamber was returned to ambient temperature overnight and the room temperature dark count remeasured prior to beginning another cold cycle. This repeated the previously measured room temperature baseline of 0.3 counts per second per pixel.

The chamber temperature was slowly decreased to -10°C and the digicon cold soaked for a minimum of four hours. The average dark count was then measured to be approximately 0.003 counts per second per pixel.

The chamber was returned to room temperature. A final room temperature dark count was made before the digicon was removed from the chamber. This data averaged approximately 0.3 counts per second per pixel, repeating the room temperature baseline rate.

6.5.1.2.2 Digicon F-5 (Bi-Alkali Photocathode)

This, the second digicon to have its dark count measured, was by far the more difficult. Not only was the count rate from the UV photocathode lower, but we had more problems associated with noise in the test set-up during these measurements.

The average dark count at room temperature was found to be .0038 counts per second per pixel.

TABLE 6.5.1.2.1-1

FOS DIGICON NO. F-3
DARK COUNT

(August 7, 1983)

Temp.	Diode No.	Counts/1000 Sec.					Avg Dark Count
20°C	105	287	306	376			
	255	347	342	306			
	355	331	305	268			
	509	360	391	388			
		1325	1344	1238			
		(.331)	(.336)	(.309)			.326
0°C	105	12	9				
	255	11	11				
	355	10	4				
	509	8	12				
		41	36				
		(0.10)	(.009)				.0096
-10°C	105	1	1	2	4	4	
	255	3	4	1	1	4	
	355	2	1	3	2	2	
	509	6	6	4	7	7	
		12	12	14	14	17	
		(.003)	(.003)	(.0025)	(.0035)	(.0042)	.0033

At reduced temperaturee, the dark count dropped to .0014 counts per second per pixel at +3°C, and to an average of .00075 counts per second per pixel at -11°C.

6.5.1.3 System Level Dark Count Measurements from T/V II

Figure 6.5.1.3-1 summarizes all background counting rate data points taken during T/V II. The important feature to observe in this figure is that there is no significant increase in background rates for either detector with increasing voltage.

The background counting rate vs. temperature for the red and blue detectors are illustrated in Figures 6.5.1.3-2 and 6.5.1.3-3, respectively. There are no significant changes in the background rates with temperature. The corrected data result from eliminating counts from individual noisy channels (28 channels on the red side and 12 channels on the blue side) to get a background that is representative of the majority of pixels.

The background counting rates vs. voltage at constant temperature for the red and blue detectors are illustrated in Figures 6.5.1.3-4 and 6.5.1.3-5, respectively. Again, the important feature to note in these figures is that there is no significant increase in counting rates as the detector bias voltage is increased.

The background counting rate is less than the specification requirement of .002 counts/sec/diode for both detectors.

Figure 6.5.1.3-6 is a graph illustrating the background rate for each channel during the long background test for the blue detector. The baseline rate for this test is 4×10^{-4} counts/sec/diode. Channels 77, 146, 170, 177, 232, 237, 279, 422, 433,

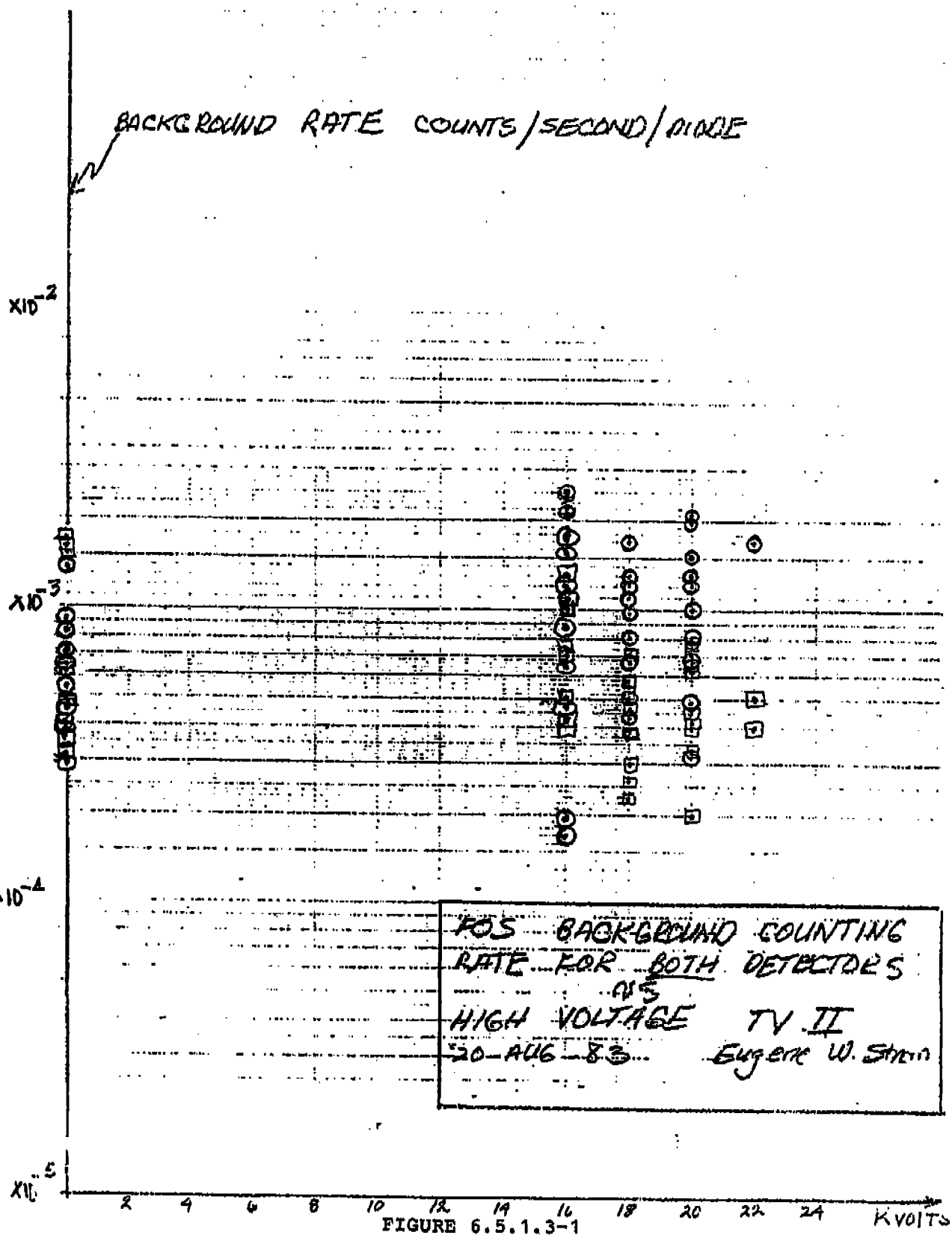

FIGURE 6.5.1.3-1

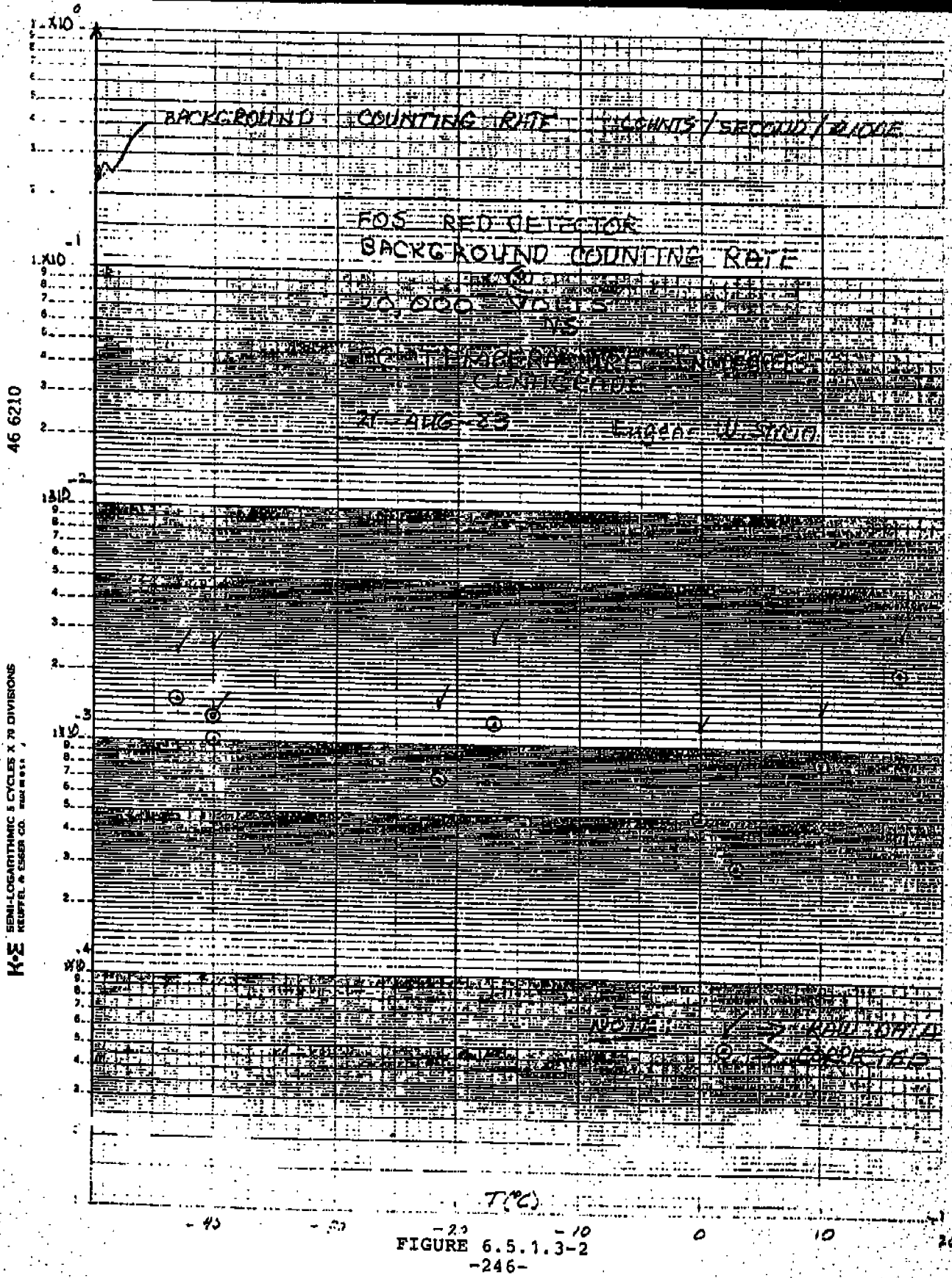

FIGURE 6.5.1.3-2

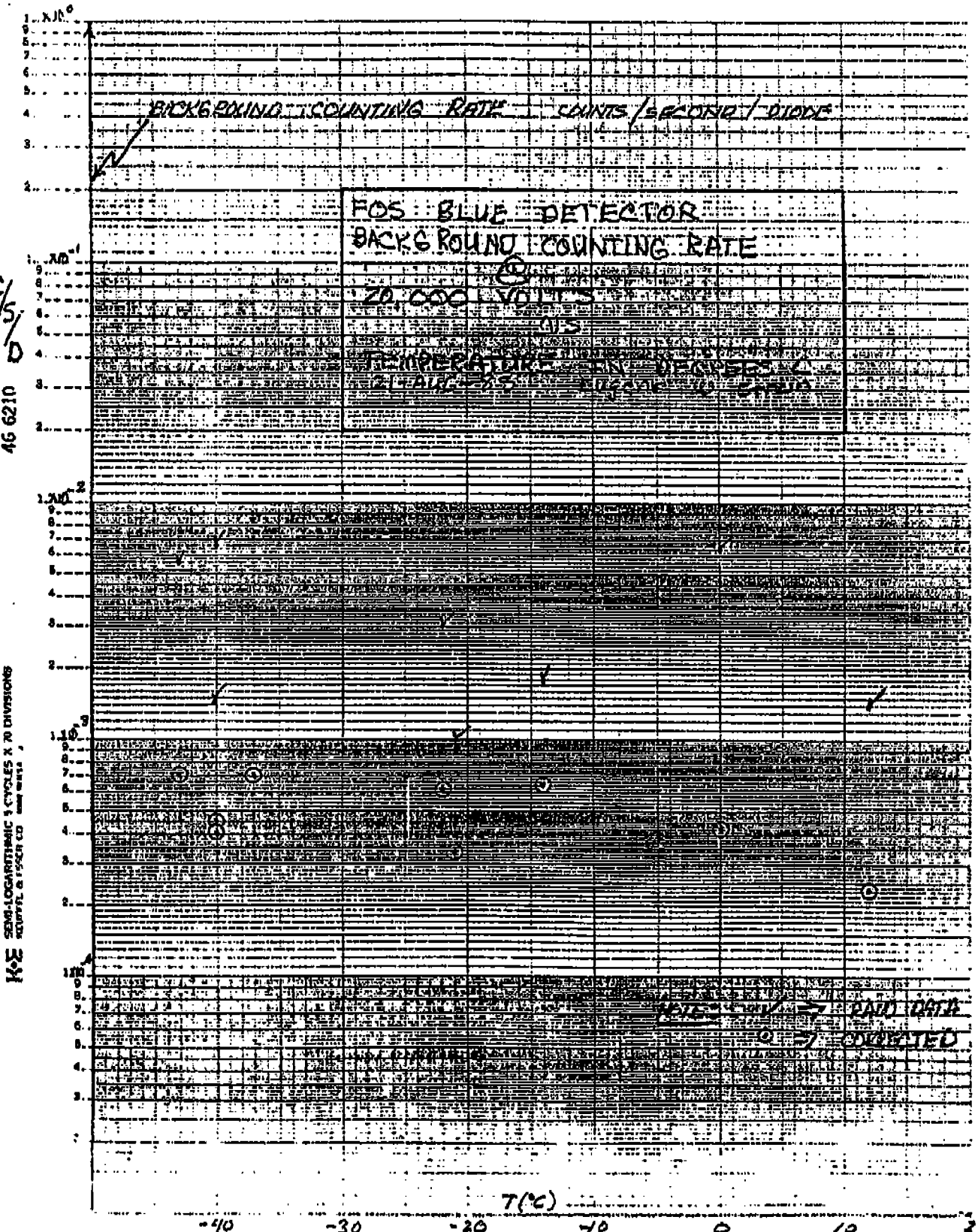

FIGURE 6.5.1.3-3

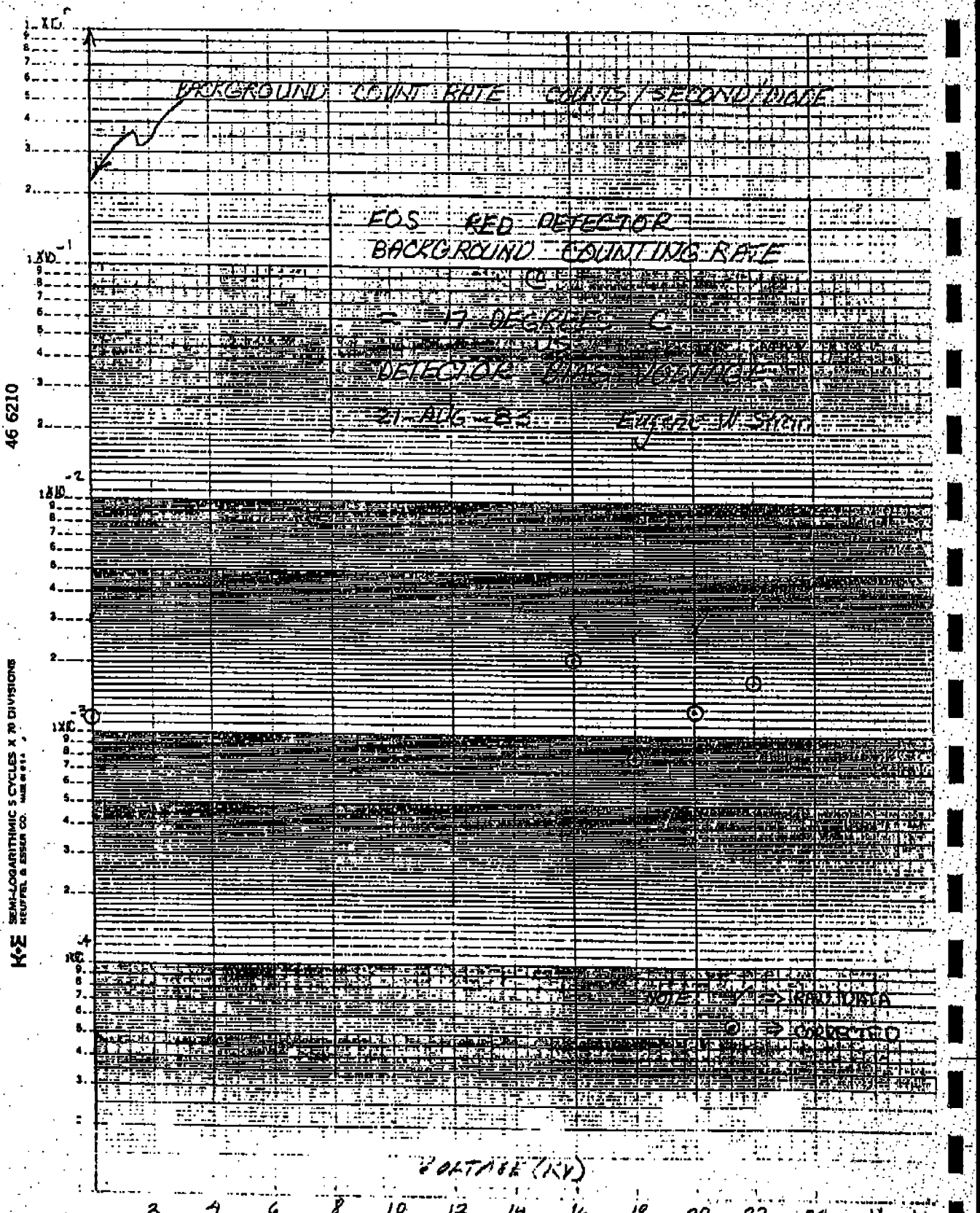

FIGURE 6.5.1.3-4

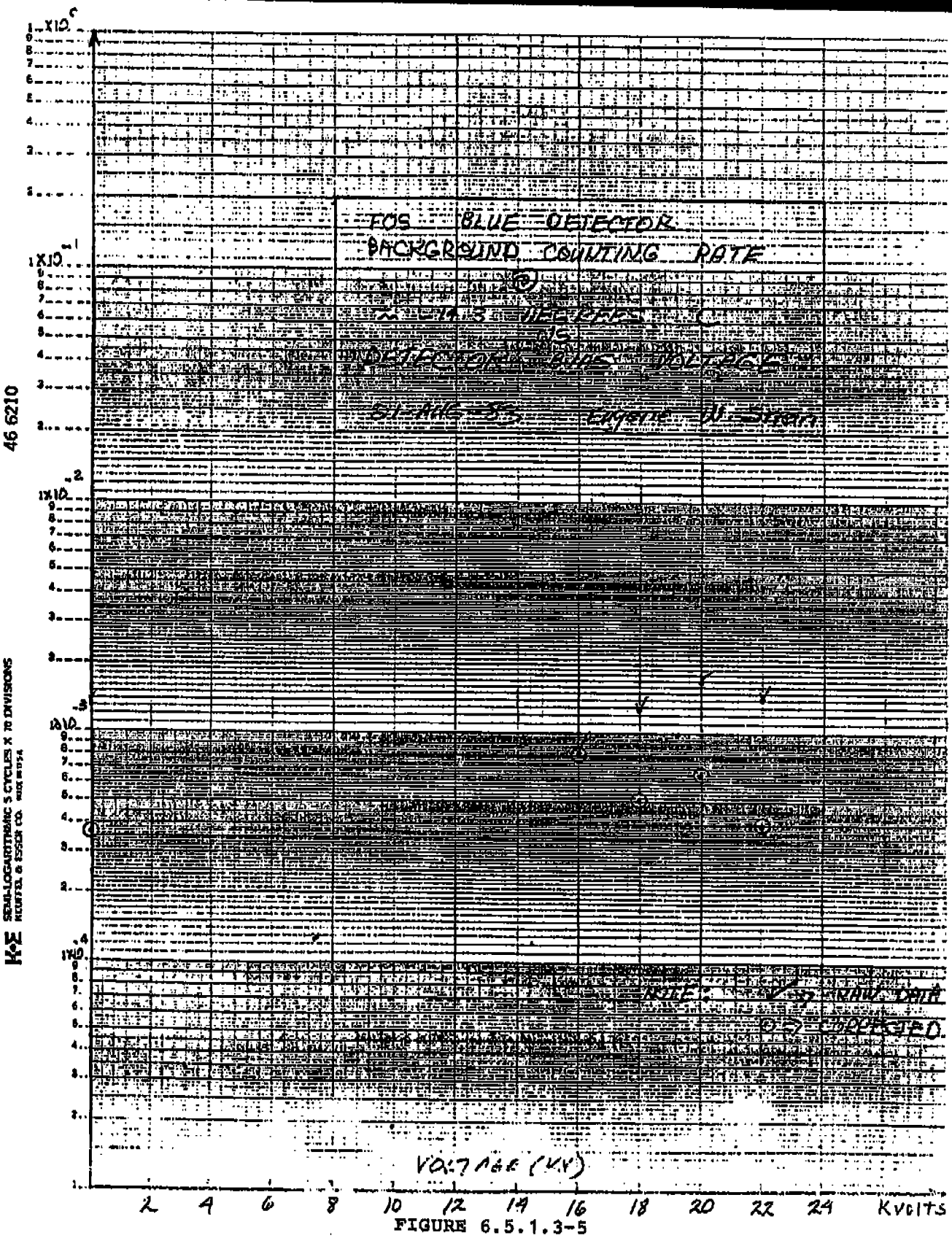

FIGURE 6.5.1.3-5

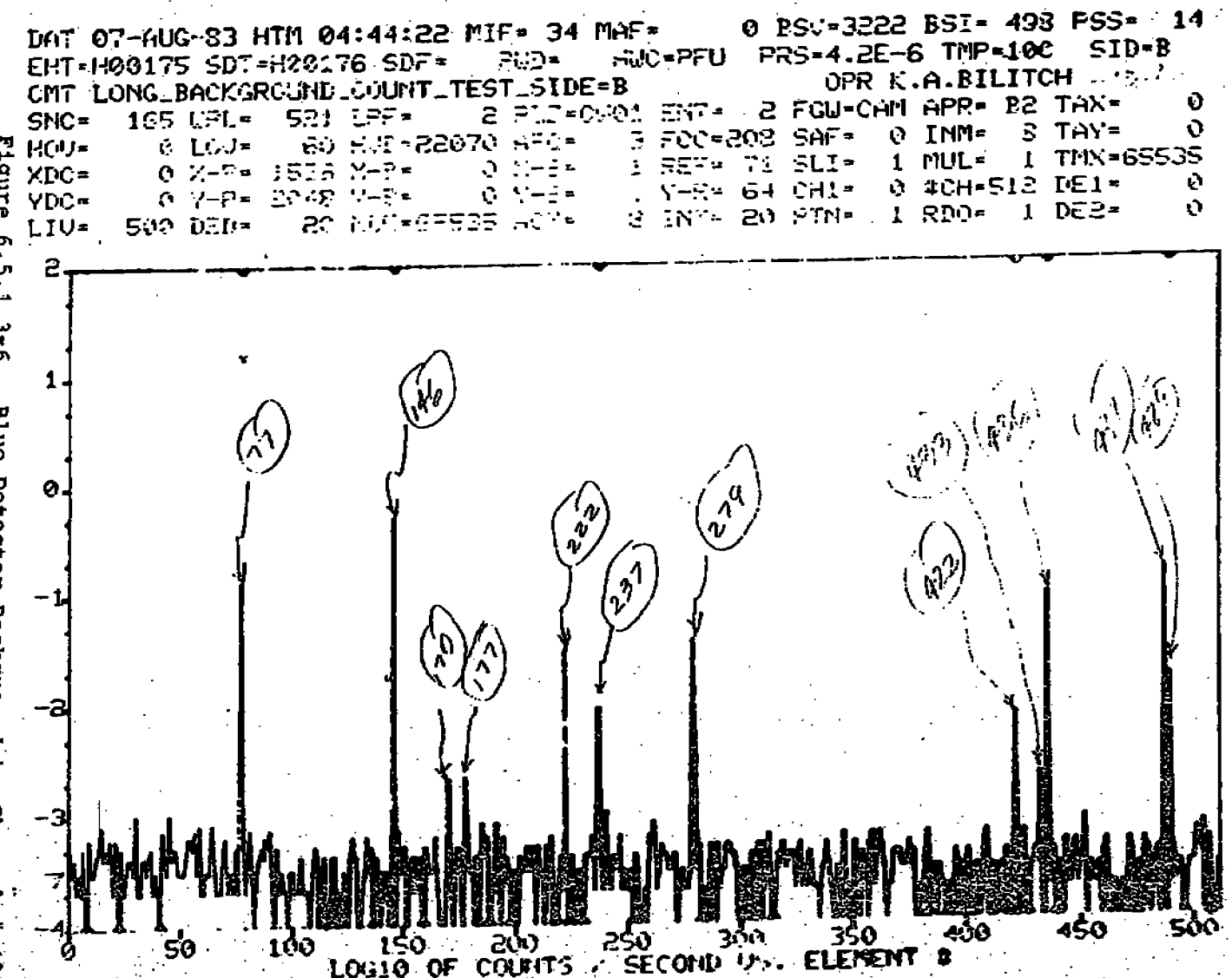

Figure 6.5.1.3-6. Blue Detector Background by Channel #, (@22kV)

436, 487,and 489 exhibited background rates that were significantly above the baseline. The data were taken with the detector operating at 22 kV.

Figure 6.5.1.3-7 is a graph illustrating the background rate for each channel during the long background test for the red detector. The baseline rate for this test is 1.1 x 10^{-3} counts/sec/diode. There are a large number of channels that have rates significantly above the baseline and there is a statistically significant feature at the center of the detector. The "hump" is believed to be additional evidence that the red detector is gassy. The enhancement in background rate at the center is believed to be caused by ions within the digicon. The data was taken with the detector operating at 22 kV. (NOTE: This F-4 red detector has since been replaced by F-3.)

Figure 6.5.1.3-8 is similar to Figure 6.5.1.3-7 for the Red Detector, except that these data were acquired at 20 kV. Note that the baseline rate is 2 x 10^{-3} counts/sec/diode for this test which is slightly higher than the data taken at 22 kV. The enhancement at the center of the detector is just noticeable here.

Figure 6.5.1.3-9 is similar to Figure 6.5.1.3-6 for the Blue Detector, except that the baseline rate is 5 x 10^{-4} counts/sec/diode for this test. Channels with counting rates significantly above the baseline are noted.

6.5.1.4 System Level Dark Count Measurements from T/V III

A number of the measurements performed during T/V II were repeated at T/V III. Some of these data are illustrated here, again to demonstrate overall system noise level specification

DAT [redacted]-AUG-83 HTM 17:14:39 MIF=103 MAF= 0 BSV=3229 BSI= 407 FSS= 11
EHT=H00164 SDT=H20165 SDF= PWD= PWC=PFU PRS=4.0E-6 TMP=13C SID=A (F4)
CMT LONG_BACKGROUND_COUNT_TEST_SIDE=A (F-4) OPR K.A.BILITCH
SNC= 165 LPL= 521 LPF= 2 PLE=CW01 ENT= 2 FGW=CHM APR= B2 TAX= 0
HOV= 0 LOV= 533 HVD=22070 ARC= 3 FOC=139 SAF= 0 INM= 8 TAY= 0
XDC= 0 X-P= 1533 X-P= 0 X-S= 1 REF= 71 SLI= 1 MUL= 1 TMX=65535
YDC= 0 Y-P= 2048 Y-P= 0 Y-S= 1 Y-R= 64 CH1= 0 #CH=512 DE1= 0
LIV= 500 DED= 20 HVM=65535 ACY= 9 INT= 20 PTN= 1 RDO= 1 DE2= 0

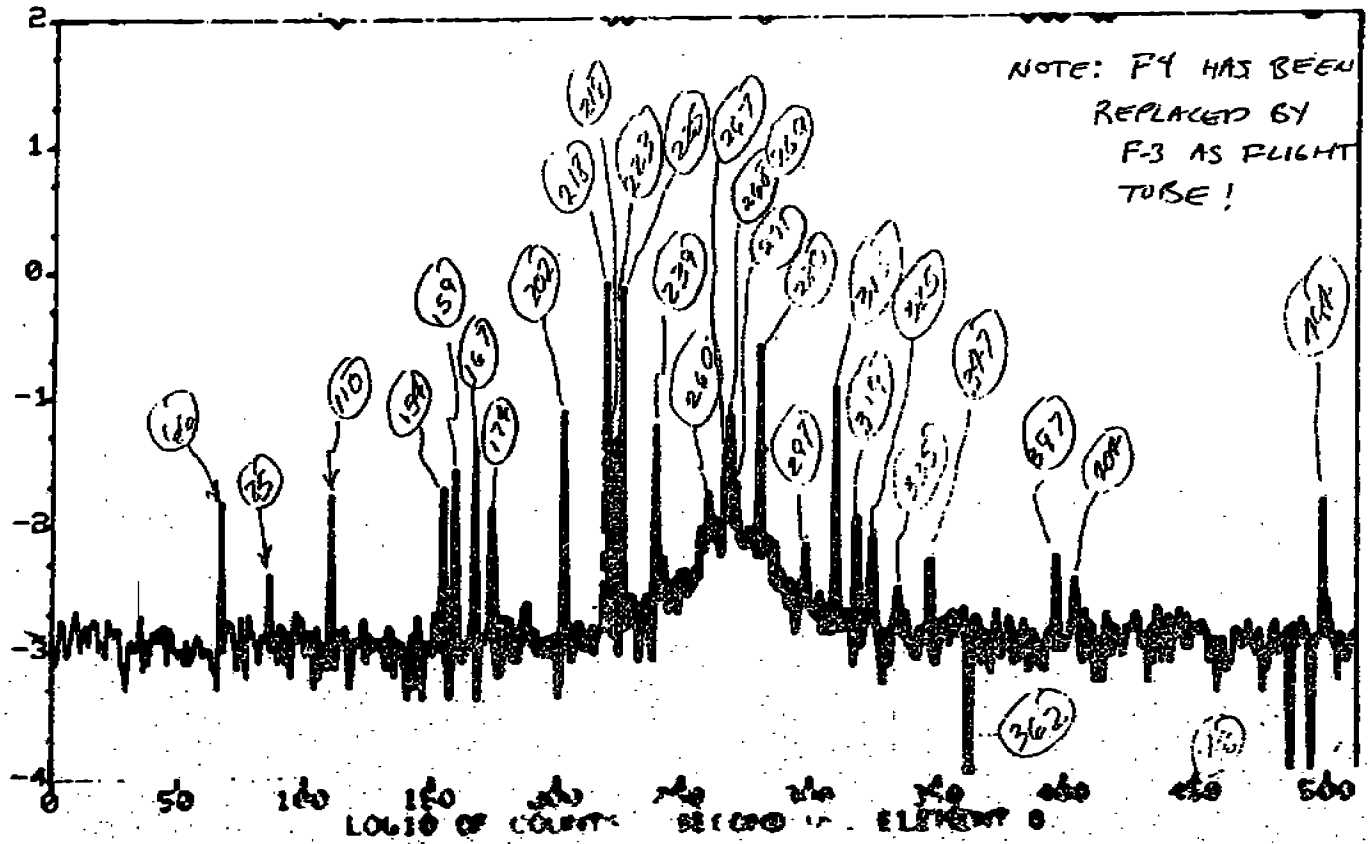

Figure 6.5.1.3-7. Red Detector Background by Channel #, (022KV)

DAT 02-AUG-83 HTM 00:57:27 MIF= 27 MAF= 0 ESV=3236 BSI= 3.7 PSS= 11
EHT=H00155 SDT=H00154 SDF= PWD= HWC=PFU PRS=3.4E-6 TMP=-39C SID=A(F-4)
CMT LONG_BACKGROUND_COUNT_TEST_SIDE-A (F-4) OPR E. W. STREIN
SNC= 165 WPL= 521 LPF= 2 PLU=CU01 ENT= 2 FGW=H40 APR= A4 TAX= 0
HOU= 0 LOU= 662 HVD=19921 ARG= 3 FOC=20S SHF= 0 INM= 8 TAY= 0
XDC= 0 X-P= 1536 X-P= 0 X-S= 1 REF= 71 SLI= 1 MUL= 1 TMX=65535
YDC= 0 Y-P= 2048 Y-S= 0 Y-S= 1 Y-R= 64 CH1= 0 #CH=512 DE1= 0
LIV= 500 DED= 0 NLL=65535 AC= 2 INT= 20 PTN= 1 PDO= 1 DE2= 0

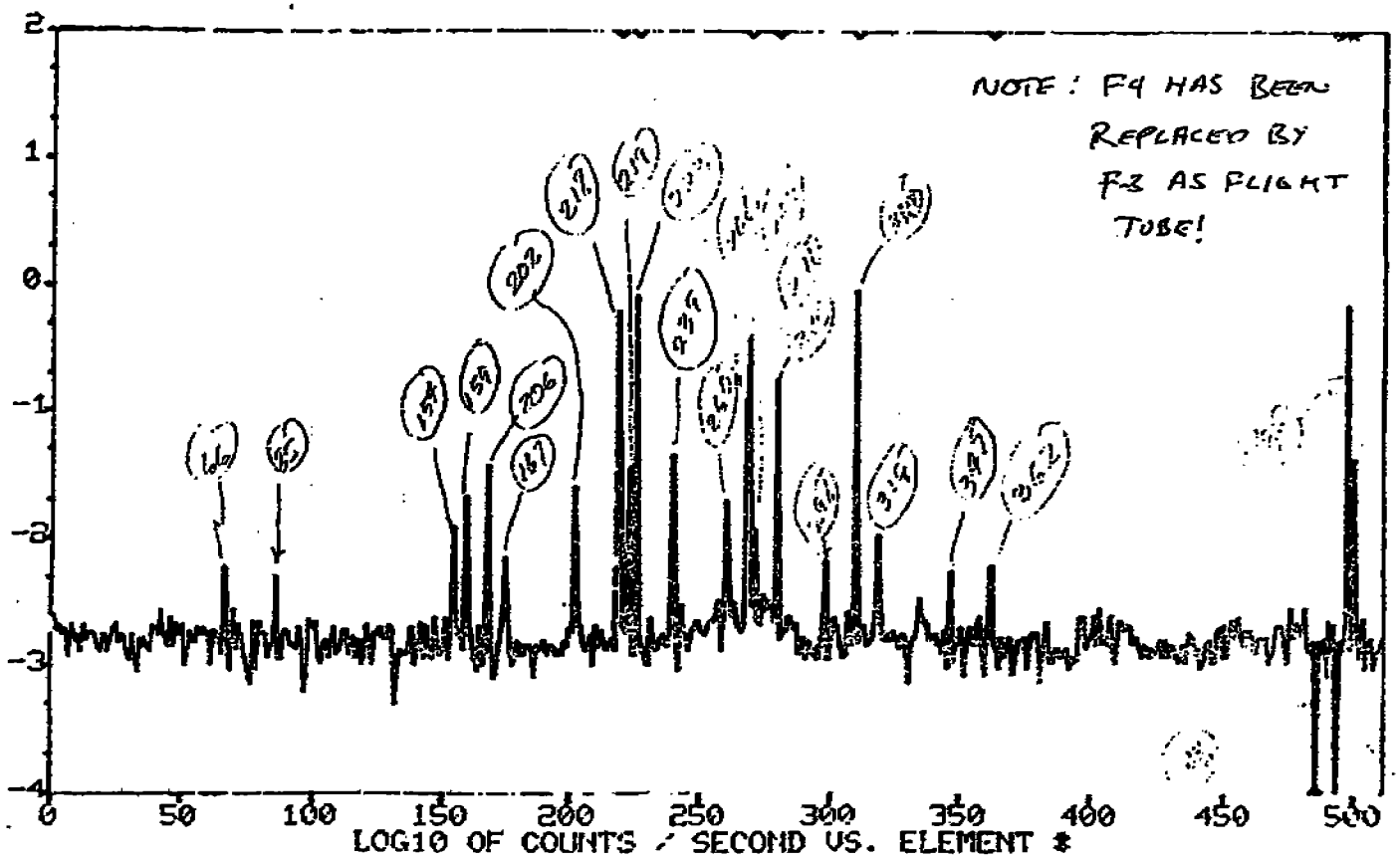

Figure 6.5.1.3-8. Red Detector Background by Channel # (@20kV)

```
DAT 04-AUG-83 HTM 17:37:07 MIF= 97 MAF=      0 BSC=3225 BSI= 459 PSS=  14
EHT=H00158 SDT=H00163 SDF=    PGD=    PGC=PFU  PRS=3.1E-6 TMP=+18C SID=B
CMT  LONG_BACKGROUND_COUNT_TEST_SIDE=B                 OPR E.W.STREIN
SNC=  165 LPI.=  521 LPF=    2 PLT=C001 ENT=  2 FGW=H40 APR= A4 TAX=     0
MOV=    % LOJ=   41 HJL=21704 APC=    3 FCC=130 SHF=  0 INM=  8 TAY=     0
XDC=    0 X-P= 1523 X-F=    0 X-I=    1 REP=  72 SLI=  1 MUL=  1 TMX=65535
YDC=    0 Y-P= 2048 Y-F=    0 Y-I=    1 Y-R=  64 CH1=  0 #CH=512 DE1=    0
LIV=  500 DED=    0 HOL=65535 ACY=    8 INT=  20 PTN=  1 RDO=  1 DE2=    0
```

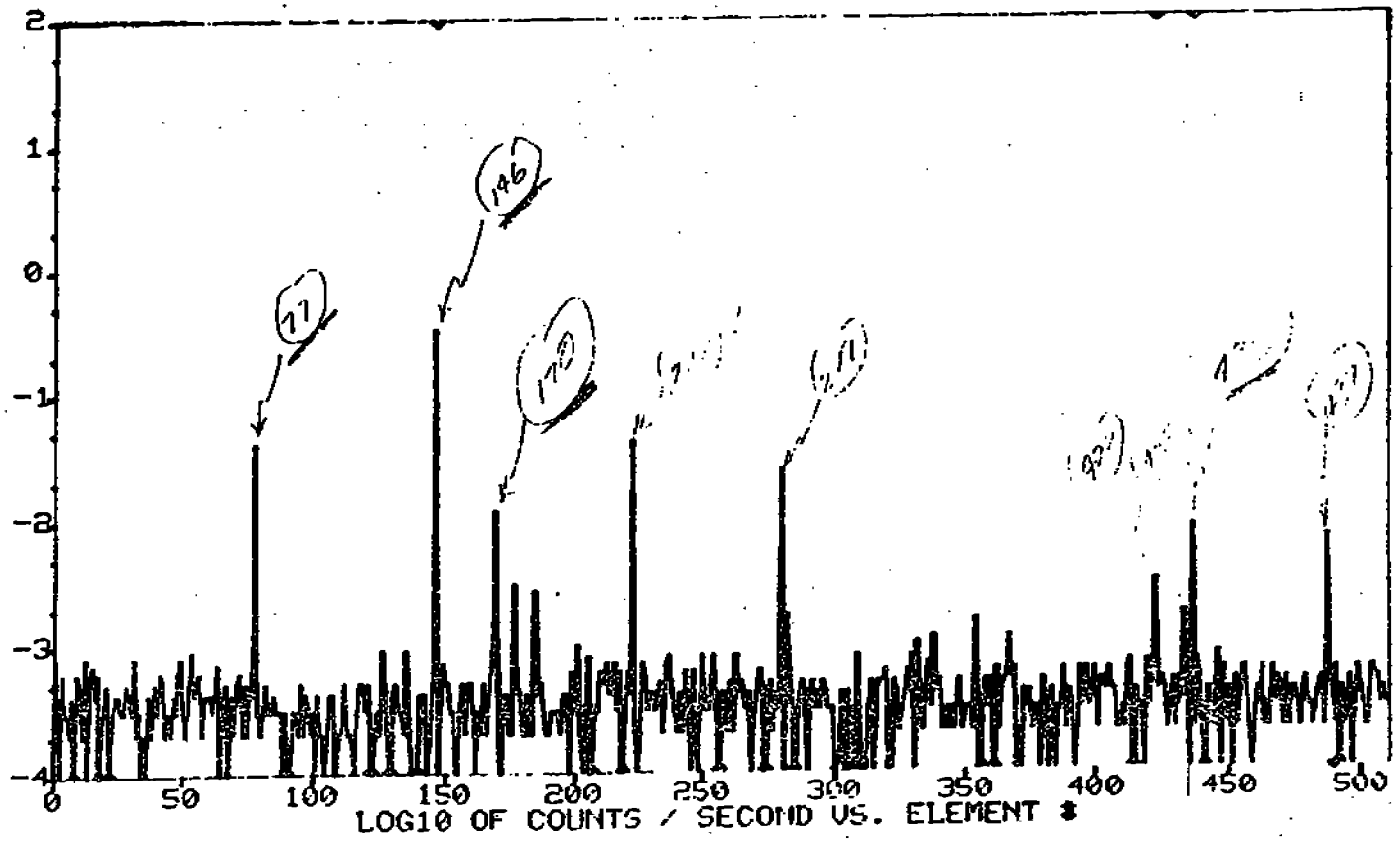

Figure 6.5.1.3-9. Blue Detector Background by Channel (020kV)

compliance. Figures 6.5.1.4-1 through 6.5.1.4-3 illustrate dark count maps for the Blue Detector taken at various time intervals. The various noisy diodes which show the large noise spikes dominate the plots. These channels have been identified and will be treated to eliminate their contribution or replaced. The plots illustrate the repeatability and stability of the system level dark count within the specifications, after subtraction of the bad channel contributions.

Figures 6.5.1.4-4 through 6.5.1.4-7 illustrate a similar sequence of dark count plots for the Red Detector. Again, after subtraction of several bad channel contributions, the system dark count is stable and repeatable, and within specification.

Table 6.5.1.4-1 summarizes 100 sec integration interval dark count data as a function of temperature for the blue detector. Figure 6.5.1.4-8 illustrates a plot of some similar, but more limited, data obtained for the Red Detector.

6.5.2 Scattered Light

Scattered light levels are obtained by observing emission lines. At a distance of 50 diodes from the spectral lines, the scattered light ranges from 1 x 10^{-5} to 4 x 10^{-5} that of the peak count rates. Upper limits to scattered light at 2 diodes from the lines range from 7 x 10^{-3} to 1 x 10^{-2} the peak count rates. An anomalous feature on the blue tube with a periodic structure of 4 diodes is not understood.

A mercury discharge tube is observed and its spectra obtained with both tubes. Three narrow bandpass filters (~ 100 Å FWHM) are used to isolate bright lines at 2537, 3458, and 5461 Å.

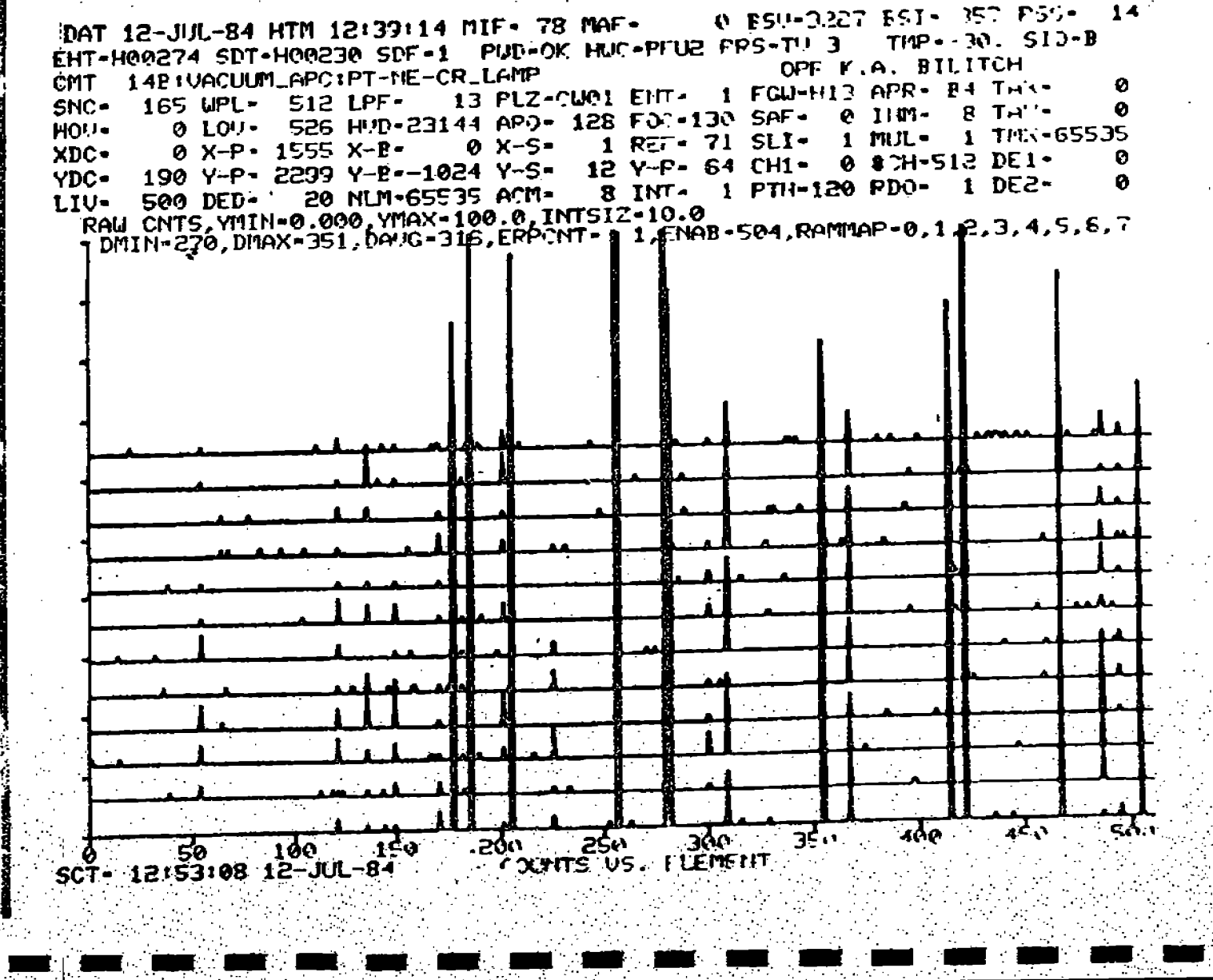

Figure 6.5.1.4-1. Blue Detector Dark Count Map from T/V III, t1

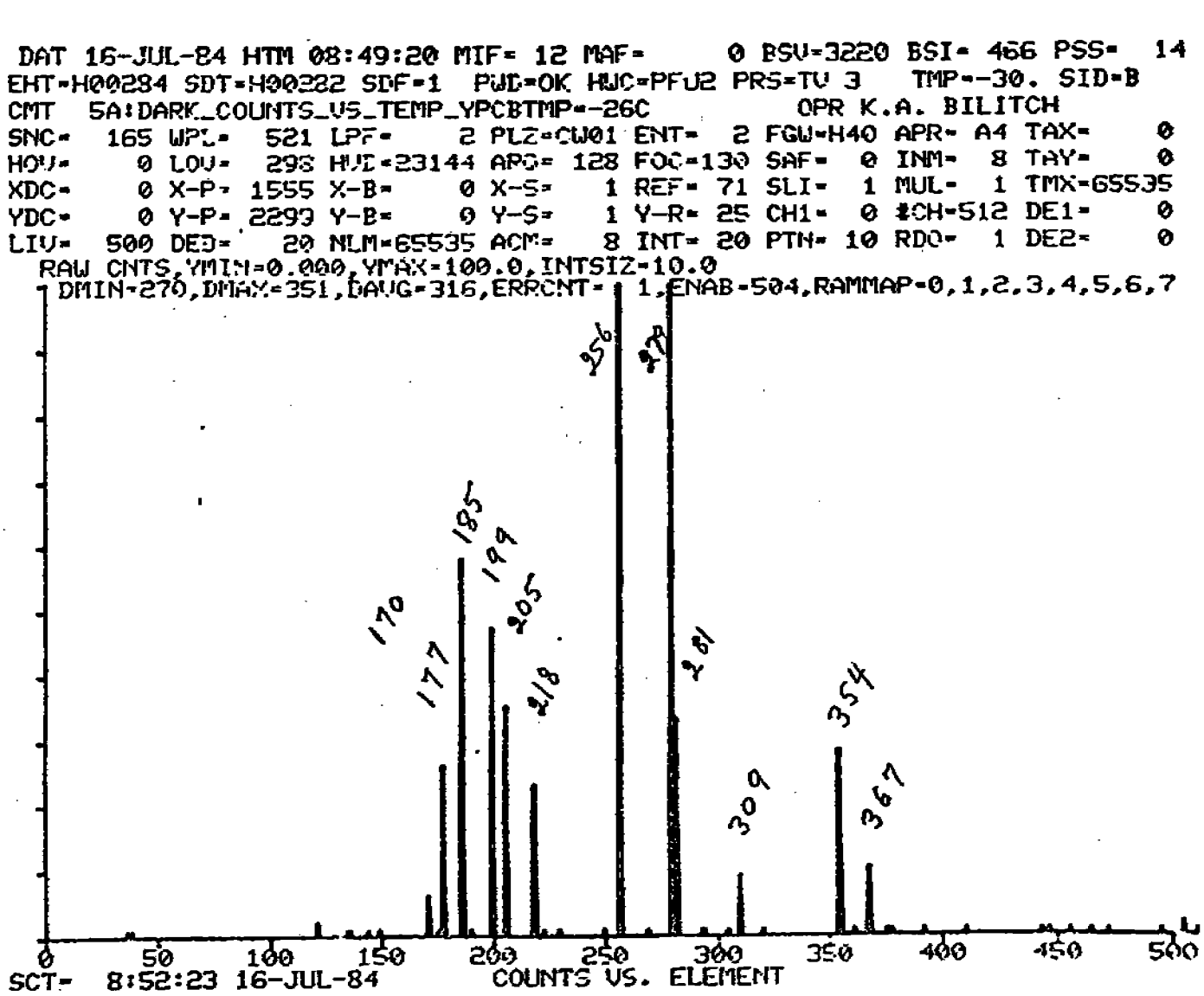

Figure 6.5.1.4-2. Blue Detector Dark Count Map from T/V III, t2

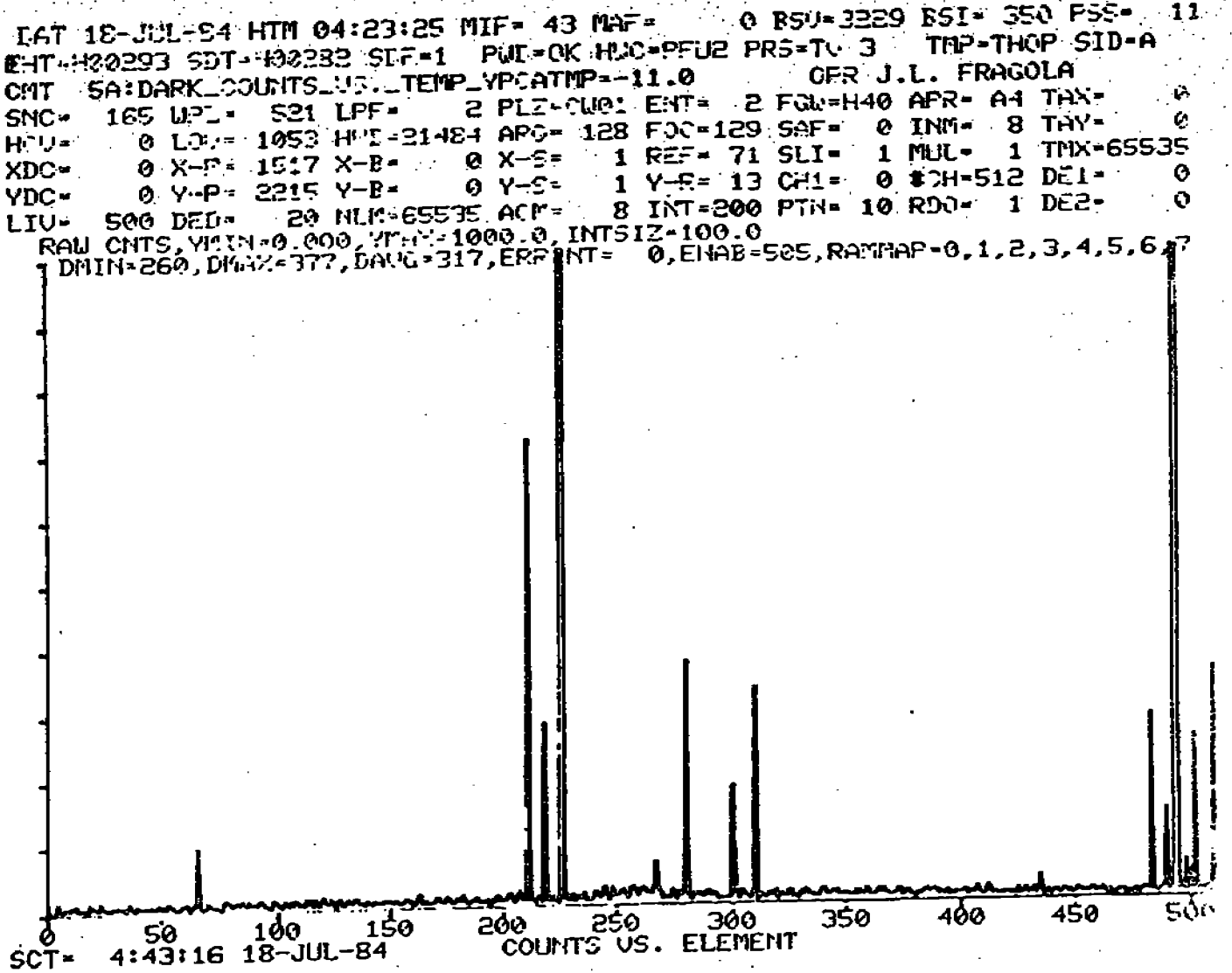

Figure 6.5.1.4-3. Blue Detector Dark Count Map from T/V III, t3

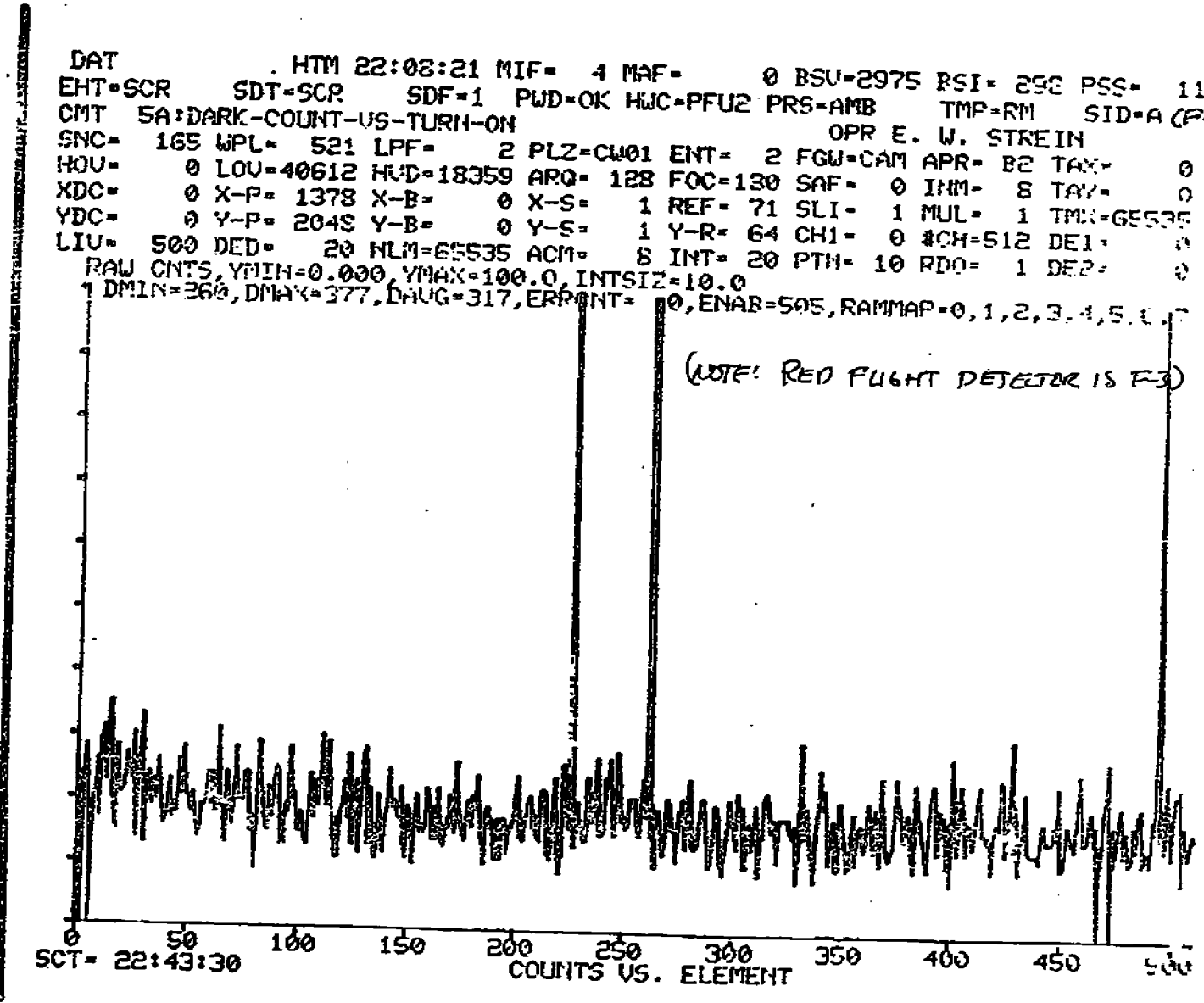

Figure 6.5.1.4-4. Red Detector Dark Count Map from T/V III, t1

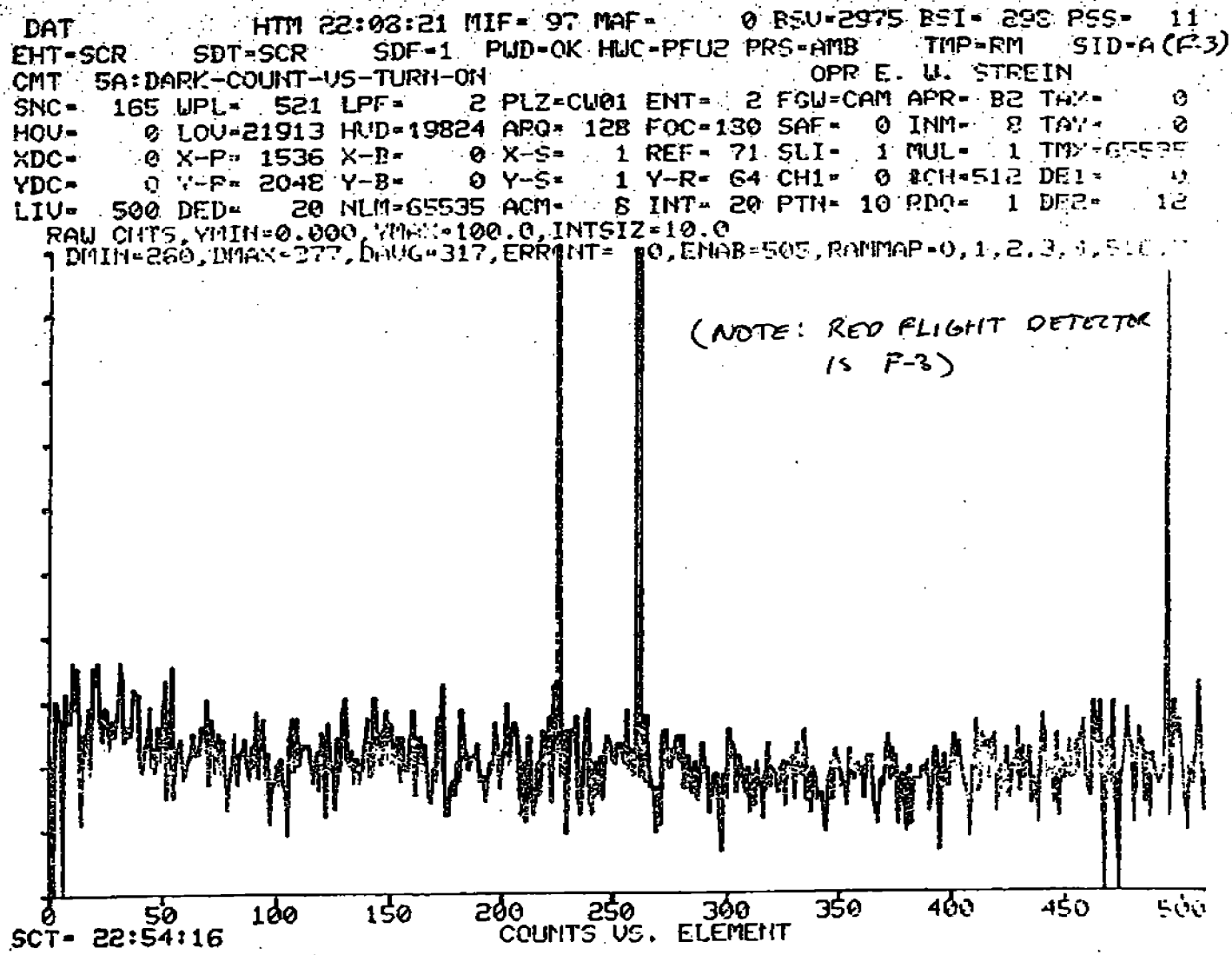

Figure 6.5.1.4-5. Red Detector Dark Count Map from T/V III, t2 -260-

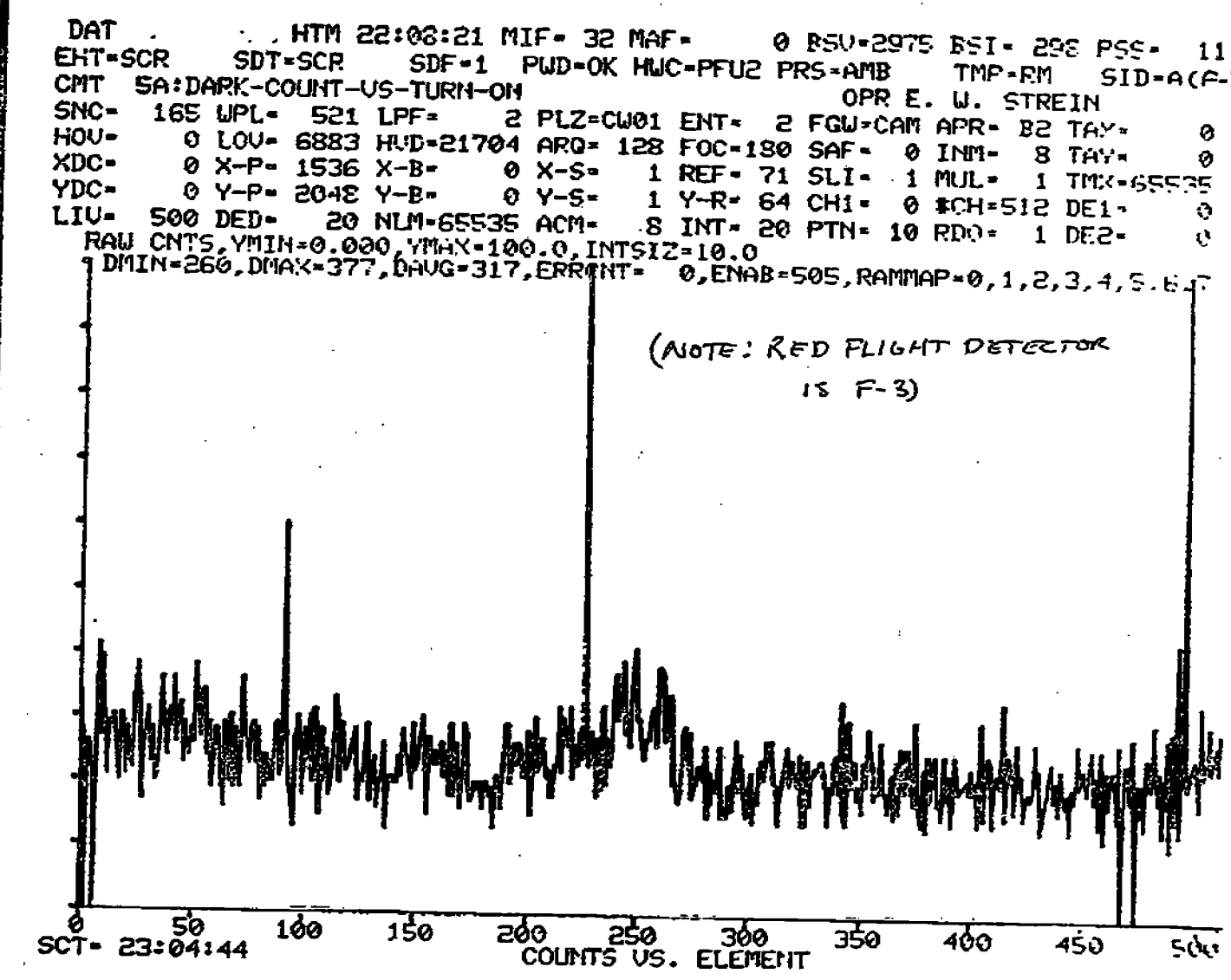

Figure 6.5.1.4-6. Red Detector Dark Count Map from T/V III, t4

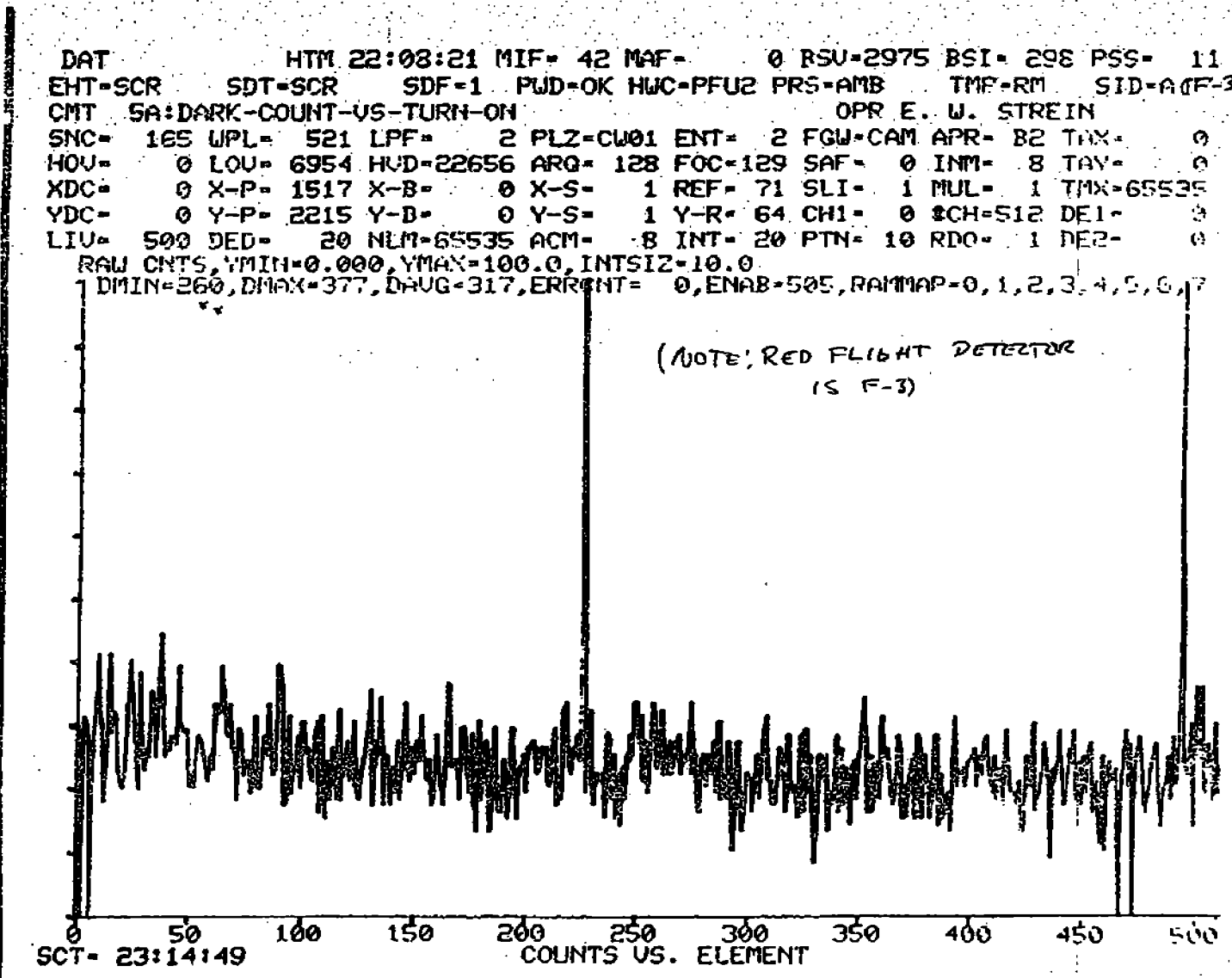

Figure 6.5.1.4-7. Red Detector Dark Count Map from T/V III, t4

TABLE 6.5.1.4-1

BACKGROUND RATE VS. TEMPERATURE, MONDAY, JULY 16, 1984

side = blue; 100 sec. integr. times

TIME	YPCBTMP	BACKGROUND CT.RATE
07:52:34	-28C	8.06 (-4)
08:49:20	-26C	5.73 (-4)
10:58:37	-23.3C	2.48 (-4)
12:02:43	-22.7C	3.74 (-4)
13:13:24	-22C	4.63 (-4)
14:11:42	-21.3C	4.38 (-4)
15:29:14	-21.3C	5.71 (-4)
16:31:24	-20.7C	1.01 (-4)
17:24:03	-20.7C	6.85 (-4)
18:29:45	-20.0C	2.45 (-4)
19:29:38	-20.0C	5.25 (-4)
20:36:27	-20.0C	2.4 (-4)
21:20:47	-20.0C	9.93 (-4)
22:17:57	-20.0C	4.61 (-4)
23:18:58	-20.0C	2.03 (-4)

Poisson fit to low-noise diodes; in addition, there are non-thermionic noise spikes in typically 10 channels

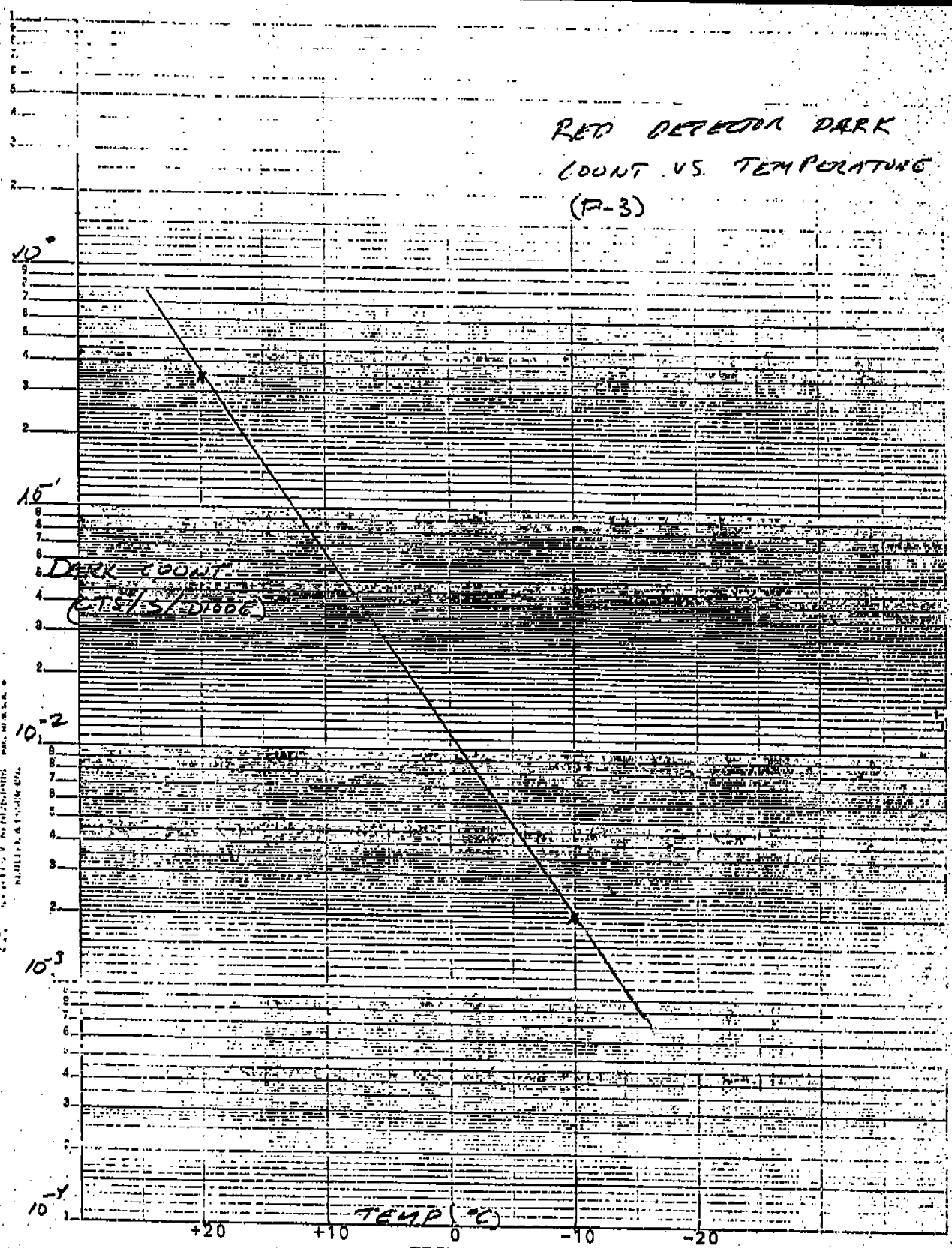

FIGURE 6.5.1.4-8

Long and short exposures are obtained of each line using several gratings. Transmission curves for the filters are determined using continuum lamps.

For each Digicon detector, four mercury spectra were obtained through the A4 aperture. Exposures of 5 seconds each were made with gratings H19, H27, H40, and H57 on the blue tube. On the red tube, exposures of 1, 15, 40, and 10 seconds were made with gratings H27, H40, H57, and H78, respectively. The concatenated spectra from the blue and red tubes are shown as Figures 6.5.2-1 and 6.5.2-2, respectively. Identified lines are labeled with their air wavelengths from the MIT wavelength tables. The blue spectra show identifiable lines from 1942 to 5791 Å and the red spectra show lines from 2481 to 7945 Å. The spectra from H40 for both tubes show a continuum from 3500 to 4600 Å. The bright UV line at 2537 Å on the blue tube has overflowed the 16-bit counter, but a shorter exposure through the 2537 A filter implies a peak of about 480,000 counts/sec.

Transmission curves for the three interference filters are obtained by taking the spectra of continuum sources with and without the filters (for example, see Figure 6.5.2-3). The expected spectra are obtained from the product of the mercury spectra and the transmission curves. Subtracting the expected spectra from the observed long-exposure filter spectra yields the scattered light (see Figure 6.5.2-4).

The short exposure spectra are used to estimate scattered light in the region 2 to 20 diodes from the mercury lines. Subtraction of the expected spectra was not possible for these expo-

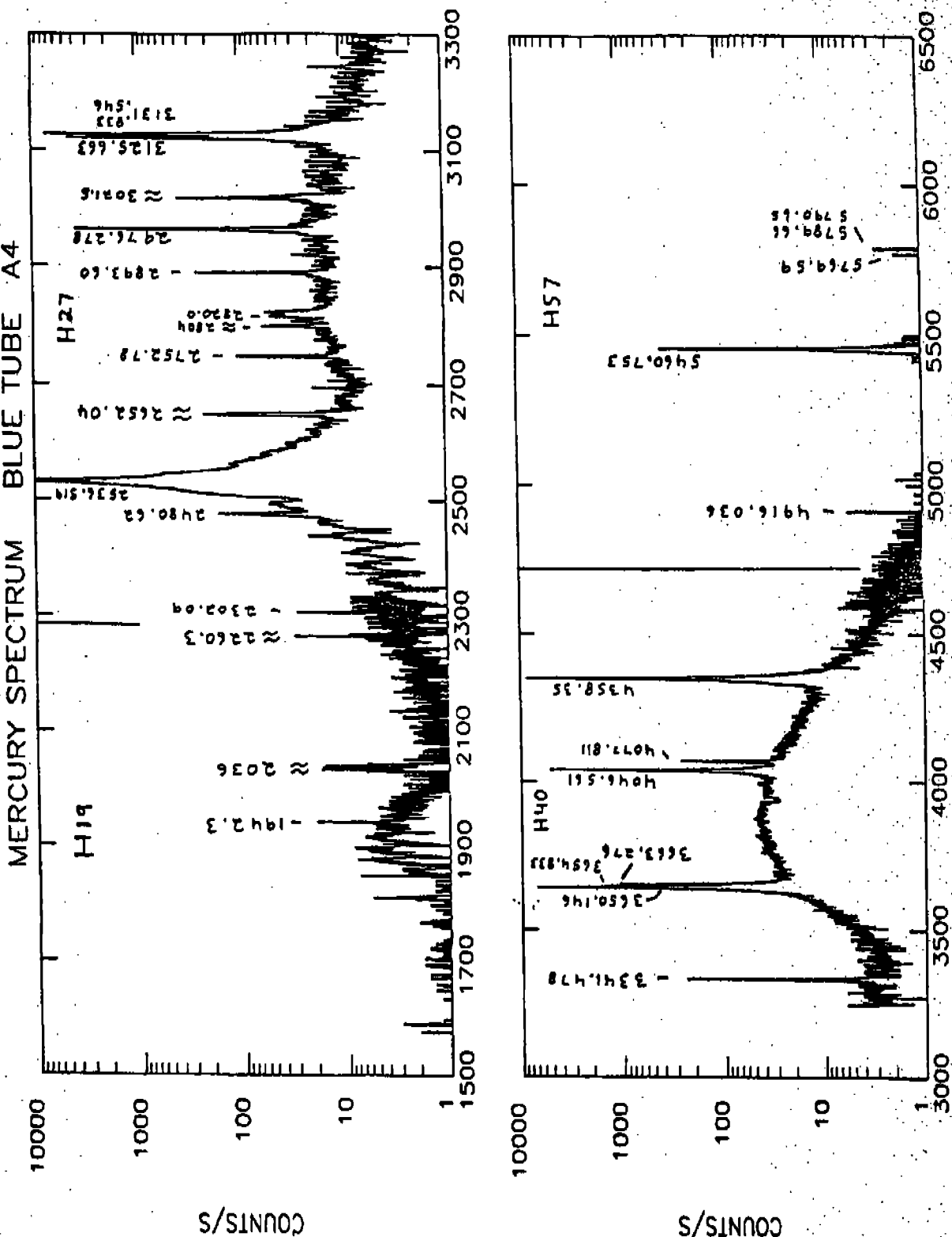

Figure 6.5.2-1. Mercury Spectrum from the blue tube

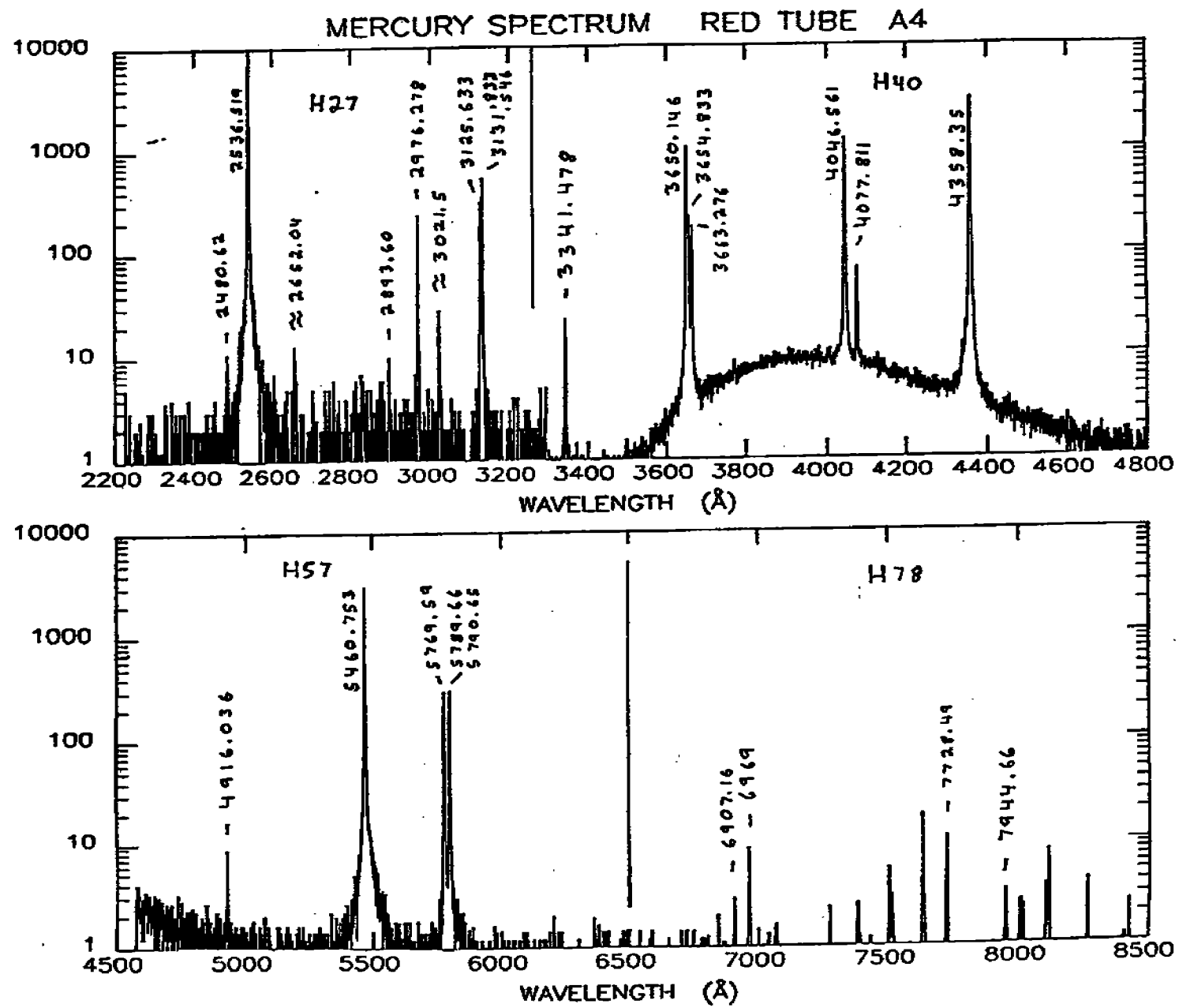

Figure 6.5.2-2. Red Tube Mercury Spectrum as for Figure 6.5.2-1

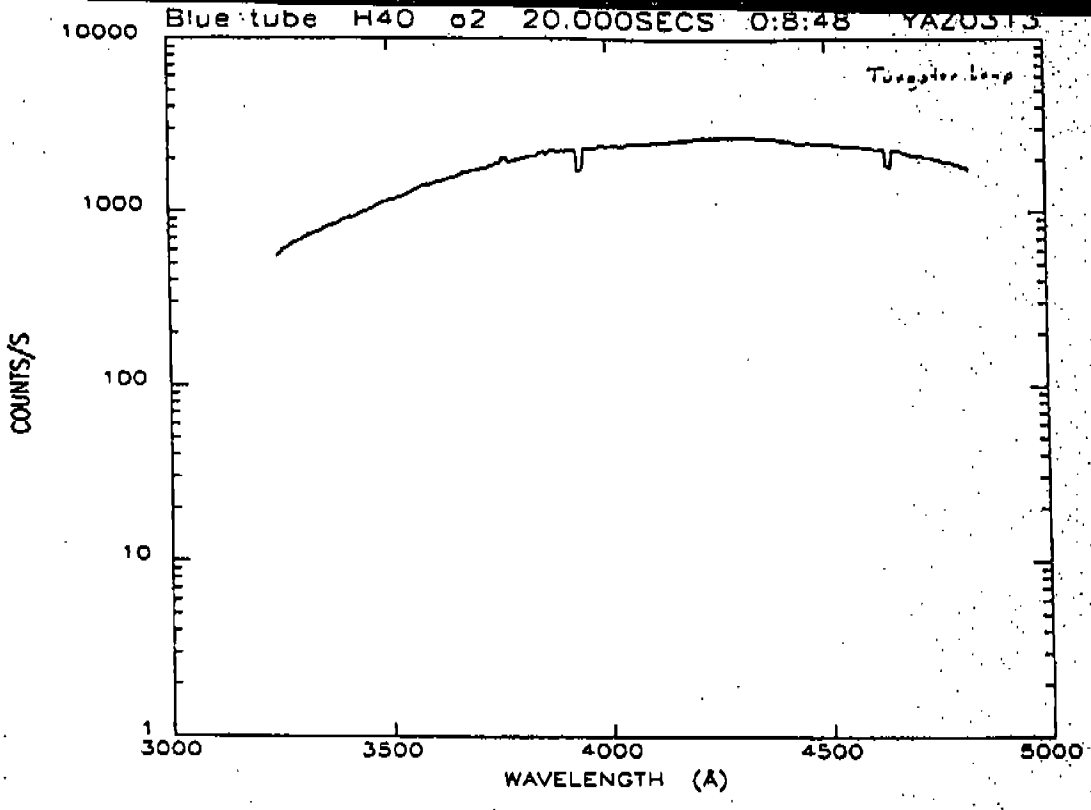
Blue tube H40 o2 20.000SECS 0:8:48 YAZ0313
Tungsten lamp
10000
1000
100
10
1
COUNTS/S
3000
3500
4000
4500
5000
WAVELENGTH (Å)

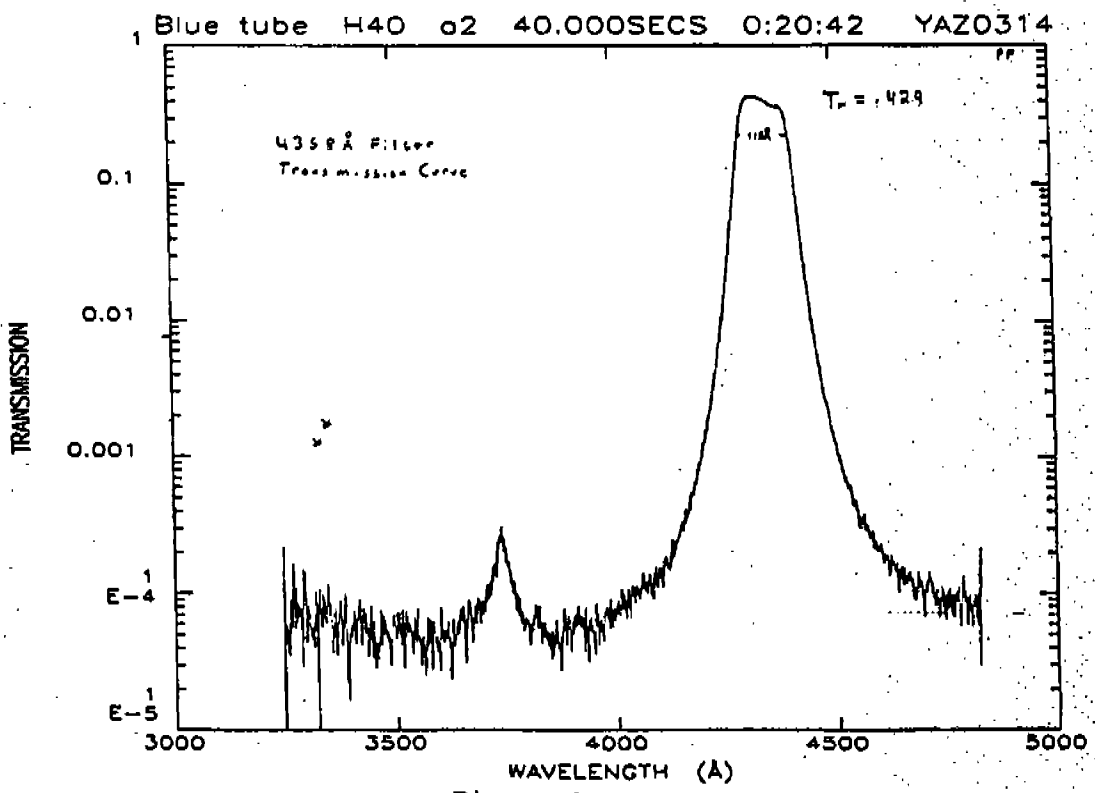
Blue tube H40 o2 40.000SECS 0:20:42 YAZ0314
4358 Å Filter
Transmission Curve
T_p = .429
1
0.1
0.01
0.001
E-4
E-5
TRANSMISSION
3000
3500
4000
4500
5000
WAVELENGTH (Å)

Figure 6.5.2-3

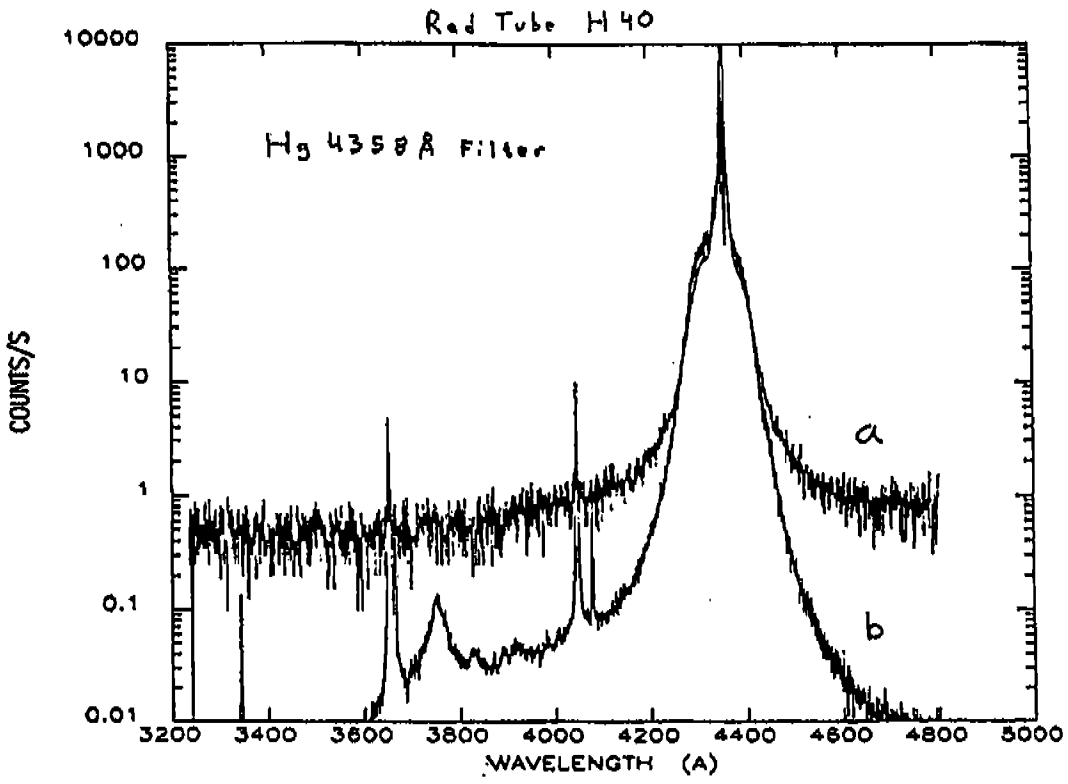
Red Tube H40
Hg 4358 Å Filter
COUNTS/S
10000
1000
100
10
1
0.1
0.01
3200
3400
3600
3800
4000
4200
4400
4600
4800
5000
WAVELENGTH (A)
a
b

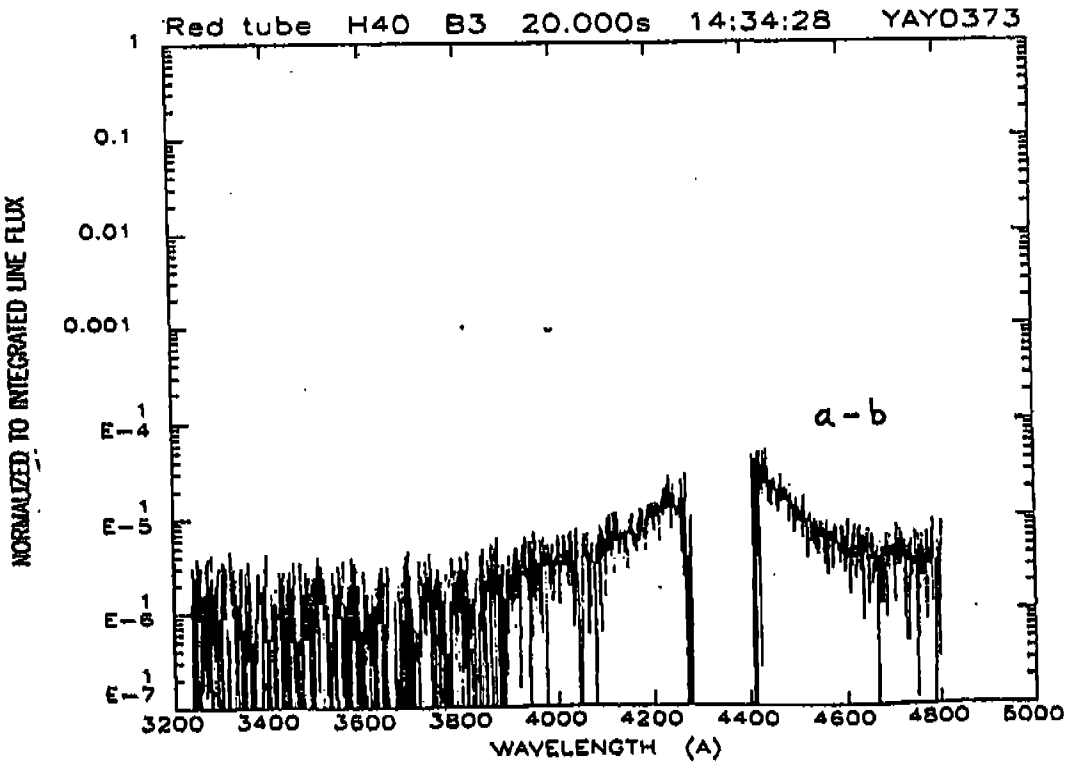
Red tube H40 B3 20.000s 14:34:28 YAY0373
NORMALIZED TO INTEGRATED LINE FLUX
1
0.1
0.01
0.001
E-4
E-5
E-6
E-7
3200
3400
3600
3800
4000
4200
4400
4600
4800
5000
WAVELENGTH (A)
a-b

Figure 6.5.2-4

sures due to insufficient counting statistics. However, the spectra are upper limits on the scattered light. Figure 6.5.2-5 shows the profile of mercury line 4358 A observed on the red tube through the 4358 filter. At two diodes from the line center, the profile agrees with the requirements specified in the FOS design. From 6 to 20 diodes, the profile is greater than the specifications by about a factor of 2. Since the FWHM transmission of the filter is 38 diodes for H40, the continuum in Figure 6.5.2-2, which is 10^{-3} times the level of line 4358 Å, may dominate the profile, so that the actual scattering in the near wings may be well below the upper limits in Figure 6.5.2-5. The scattering in the far wings shown in Figure 6.5.2-4, bottom plot, is typical for both tubes and for gratings H27, H40, and H57. In all cases, the scattered light is well below the design specifications of 2×10^{-4} at 50 diodes and 1×10^{-4} beyond 100 diodes from the line center.

In eight spectra from the blue tube, periodic features are present, examples of which are shown in Figure 6.5.2-6. In all eight cases, the period of the features is between 4.0 and 4.12 diodes and the distance from the emission line approximately 270 diodes. Since the features appear on spectra taken with H27, H40, L15, the prism, and the camera mirror, with filters 2837 and 4358, the anomalies seem to be independent of grating, filter, and wavelength, thus suggesting an origin within the Digicon. For the H27 spectrum in Figure 6.5.2-6, the maximum level of the anomaly is 2×10^{-5} of the total count rate. No anomalous features are observed from red tube spectra. However, the thermionic

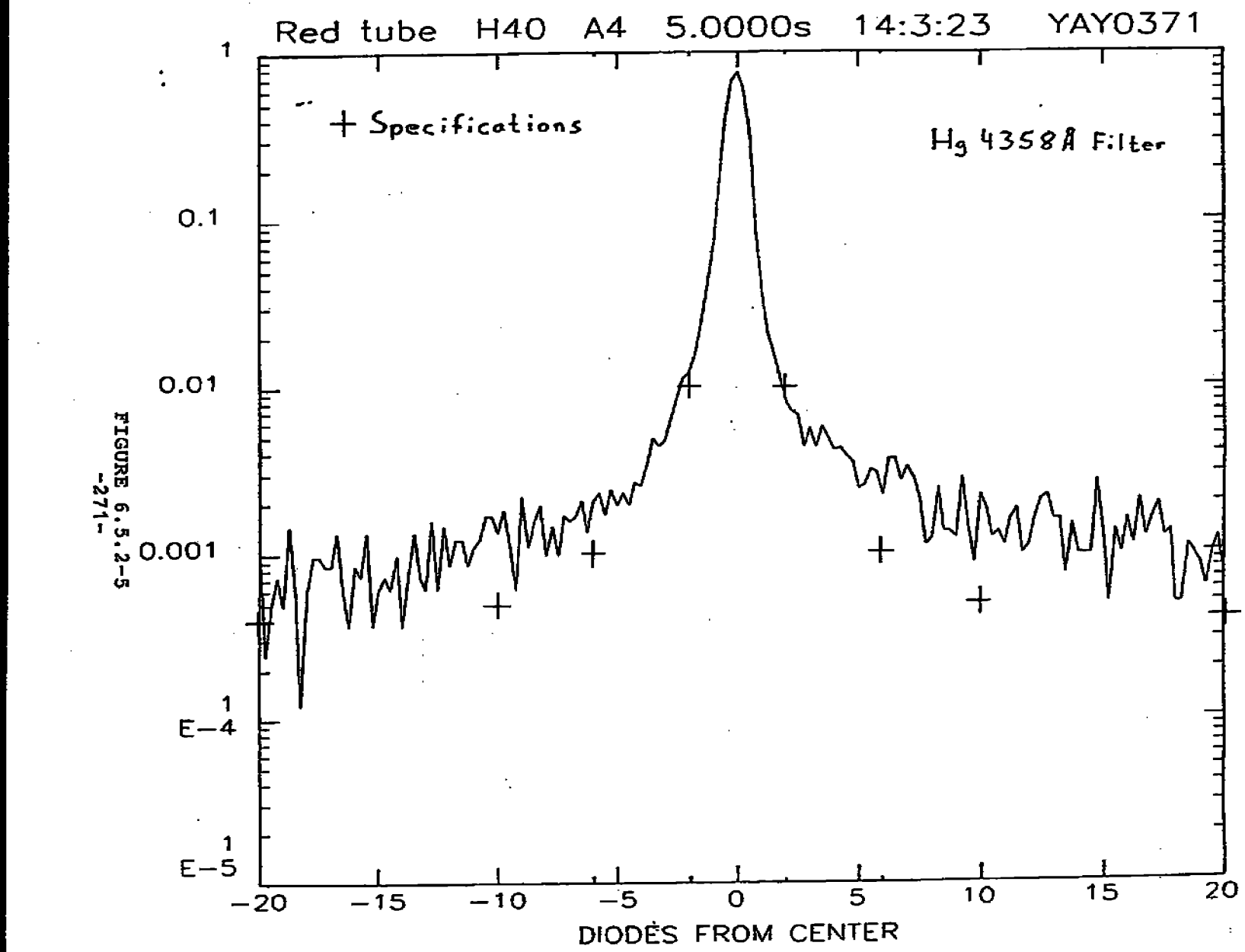
Red tube H40 A4 5.0000s 14:3:23 YAY0371
+ Specifications
Hg 4358Å Filter
1
0.1
0.01
0.001
1
E-4
1
E-5
-20
-15
-10
-5
0
5
10
15
20
DIODES FROM CENTER

FIGURE 6.5.2-5

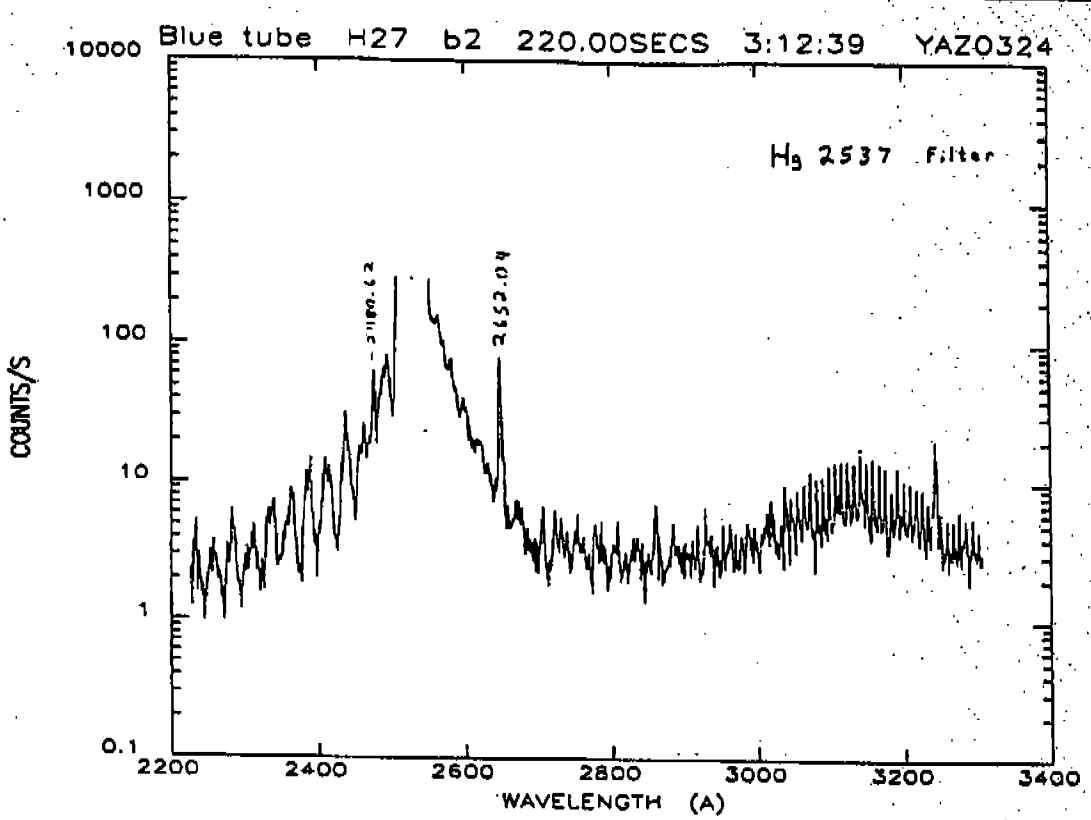
Blue tube H27 b2 220.00SECS 3:12:39 YAZ0324
Hg 2537 Filter
COUNTS/S
10000
1000
100
10
1
0.1
2200
2400
2600
2800
3000
3200
3400
WAVELENGTH (A)

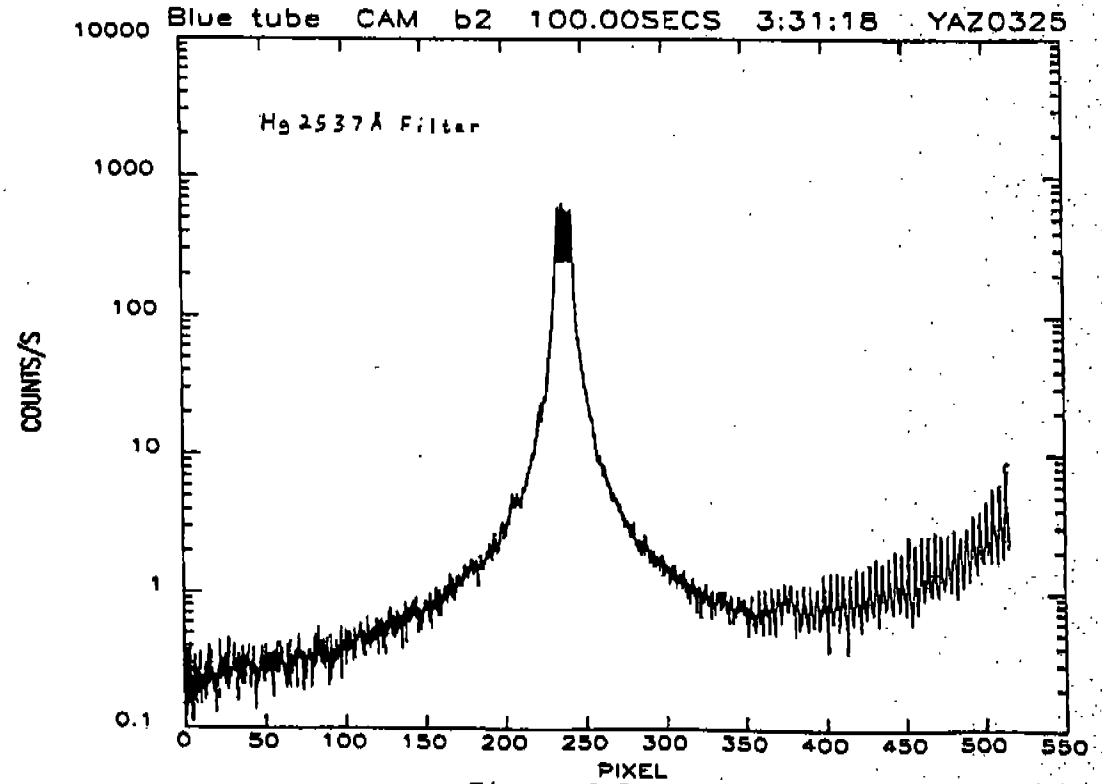
Blue tube CAM b2 100.00SECS 3:31:18 YAZ0325
Hg 2537Å Filter
COUNTS/S
10000
1000
100
10
1
0.1
0
50
100
150
200
250
300
350
400
450
500
550
PIXEL

Figure 6.5.2-6

dark count of 0.33 counts/sec at ambient temperature may mask any such features on the red tube. Power spectrum analysis will be performed on red spectra to see if such anomalies do indeed exist.

6.5.3 FOS-Scattered Red Light (Red Tube)

The FOS is inherently susceptible to unwanted light, since it is a single pass spectrograph employing blazed, concave gratings, and possesses a wide spectral bandpass of sensitivity.

The laboratory data to be discussed here were obtained by placing several different (red-pass) absorbing filters in front of the (Tungsten) continuum source. The resulting absorption region was observed to measure the stray light contribution. This method is particularly relevant as it mimicks the observation of late type stars, which have rather steep cut-offs in their energy distribution in the ultraviolet.

The filters used were spare flight (Schott) units, designated OG530, GG395*, WG295, and WG230. Their approximate transmission curves are shown as Figure 6.5.3-1.

The actual observed countrates (through aperture C3) are shown as Figure 6.5.3-2. For each filter, four different gratings (H19, H27, H40, and H57) were observed. The necessary paired-pulse corrections for countrates in excess of approximately 2000 counts/sec are indicated with broken lines.

Of particular relevance are the observed counts using the H19 grating (1500-2350 Å). The four curves shown in that wavelength region correspond to each of the four filters used and the countrates increase from roughly 2 counts/sec for OG530 to about 8 counts/sec for WG230. This is easily understood as the conse-

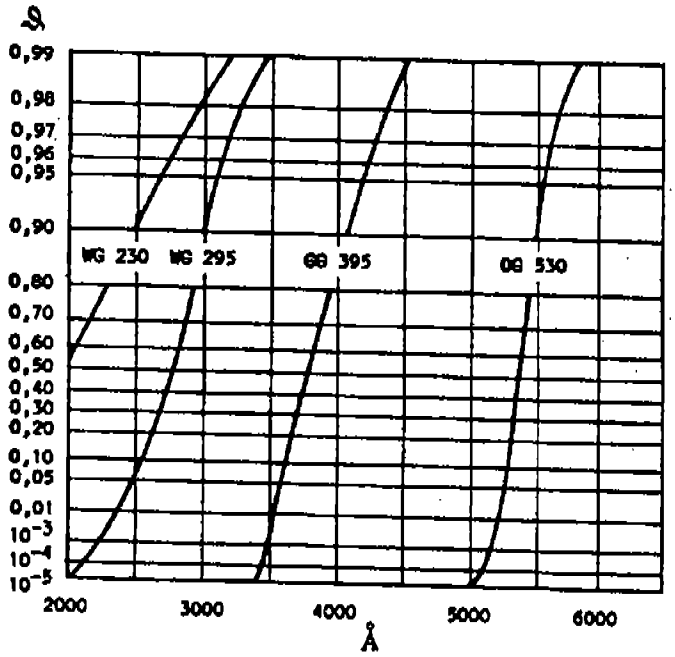
ϱ
0,99
0,98
0,97
0,96
0,95
0,90
0,80
0,70
0,60
0,50
0,40
0,30
0,20
0,10
0,05
0,01
10⁻³
10⁻⁴
10⁻⁵
WG 230
WG 295
GG 395
GG 530
2000
3000
4000
5000
6000
Å

Figure 6.5.3-1

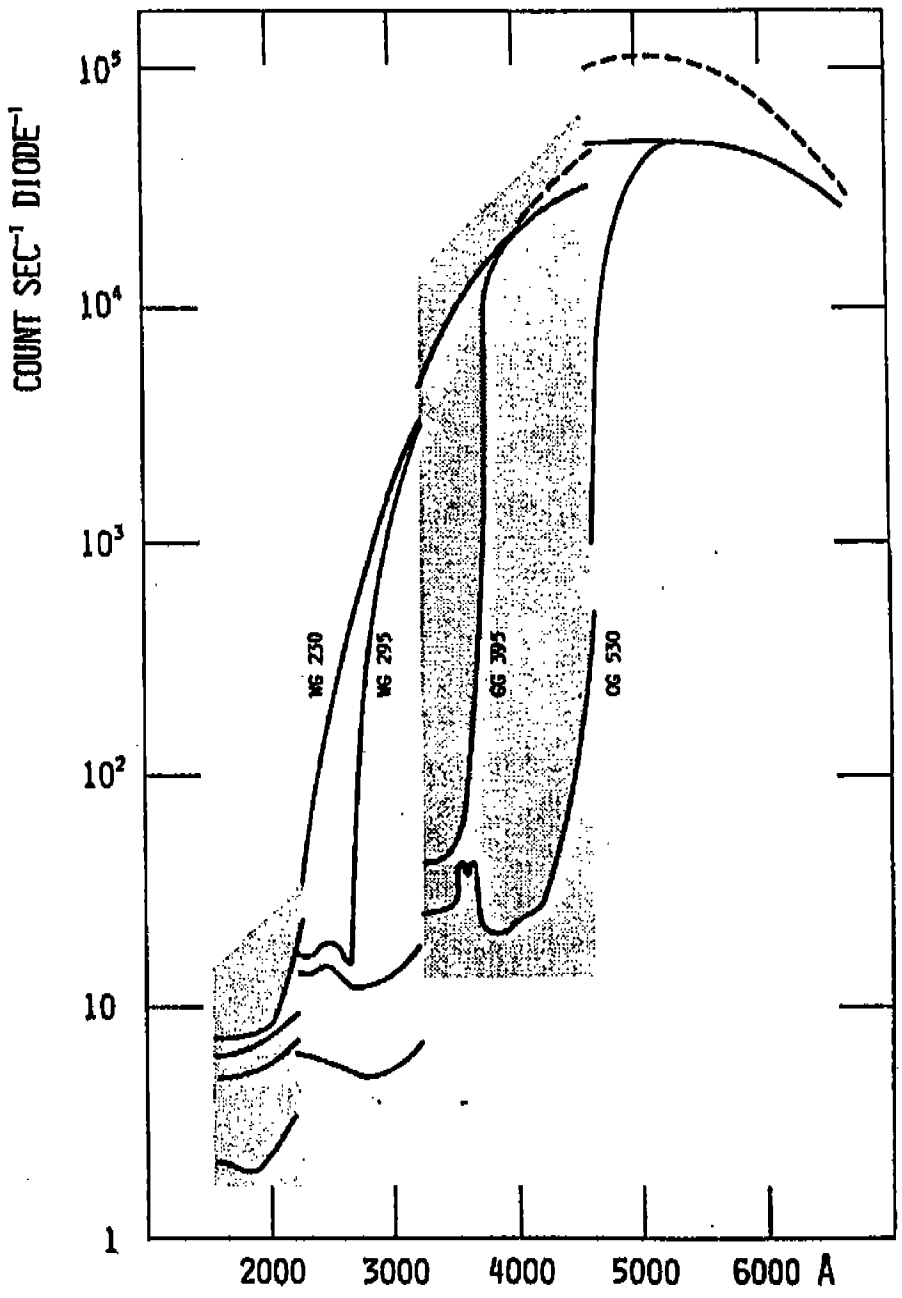
COUNT SEC⁻¹ DIODE⁻¹
10⁵
10⁴
10³
10²
10
1
WG 230
WG 295
GG 395
GG 530
2000
3000
4000
5000
6000 Å

Figure 6.5.3-2

quence of the increase in bandwidth of the incoming flux from the Tungsten lamp. Note that although the Figure 6.5.3-2 is labelled in Angstroms, the measured counts are obviously from ("scattered") optical and near ultraviolet photons.

The effective bandwidth of the incoming light is limited at the long wavelength side by the cut-off of the photocathode of the (Red) tube which occurs around 7000 Å. On the blue side, the observed values for the cut-off are about 4800**, 3750, 2850 and 2300 Å, for OG530, GG395, WG295, and WG230, respectively. Note that although the increase of bandwidth in going from OG530 to GG375 is rather modest in an absolute sense, the observed amount of scattered light (in H19) more than doubles. This is probably due to the increase of scattering efficiency for decreasing wavelength (e.g., Rayleigh scattering $\alpha \lambda^{-4}$) and suggests that most of the photons counted in H19 through the OG530 filter have probable wavelengths of around 5500 Å, rather than the larger values present in the incoming flux.

The observed curves of Figure 6.5.3-2 are thus generally well understood, at least in a qualitative sense. Exception should be made for the unidentified feature around 3550 Å (H40-grating). The width of this feature is about 150 Å and exhibits a central "inversion". The observational data in this wavelength region are attached as Figure 6.5.3-3.

*There is some confusion with respect to this filter. The FOS Scientists Notebook calls this filter GG395, whereas Harms et al. in NASA CP-2244 quote GG375.

**This observed cut-off is somewhat surprising as the Schott-catalog (see Figure 6.5.3-1) claims that the transmission in this filter should be down to 10^{-5} at 5000 Å.

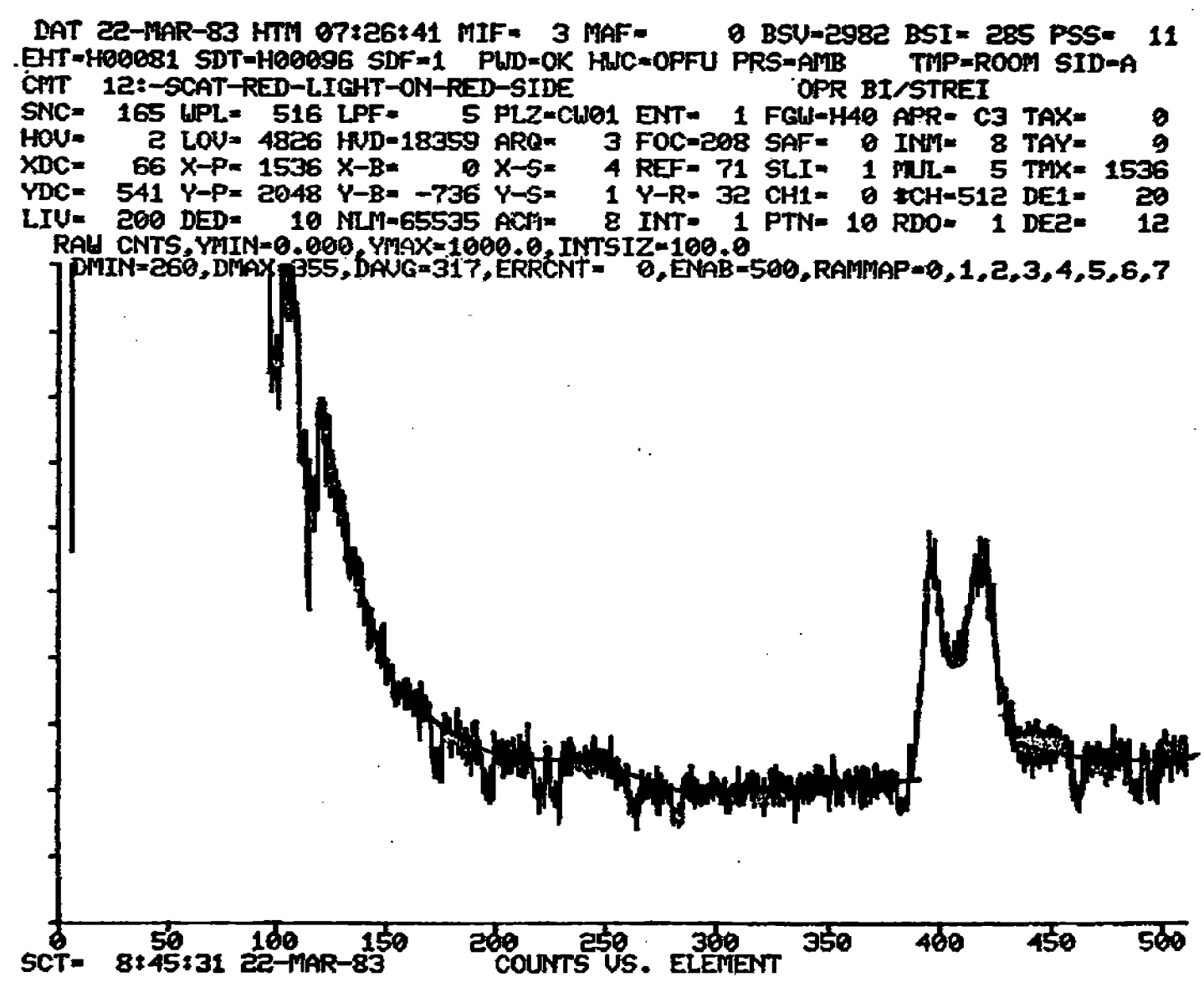
DAT 22-MAR-83 HTM 07:26:41 MIF= 3 MAF= 0 BSV=2982 BSI= 285 PSS= 11
EHT=H00081 SDT=H00096 SDF=1 PWD=OK HWC=OPFU PRS=AMB TMP=ROOM SID=A
CMT 12:-SCAT-RED-LIGHT-ON-RED-SIDE OPR BI/STREI
SNC= 165 WPL= 516 LPF= 5 PLZ=CW01 ENT= 1 FGW=H40 APR= C3 TAX= 0
HOV= 2 LOV= 4826 HVD=18359 ARQ= 3 FOC=208 SAF= 0 INM= 8 TAY= 0
XDC= 66 X-P= 1536 X-B= 0 X-S= 4 REF= 71 SLI= 1 MUL= 5 TMX= 1536
YDC= 541 Y-P= 2048 Y-B= -736 Y-S= 1 Y-R= 32 CH1= 0 #CH=512 DE1= 20
LIV= 200 DED= 10 NLM=65535 ACM= 8 INT= 1 PTN= 10 RDO= 1 DE2= 12
RAW CNTS,YMIN=0.000,YMAX=1000.0,INTSIZ=100.0
DMIN=260,DMAX=355,DAVG=317,ERRCNT= 0,ENAB=500,RAMMAP=0,1,2,3,4,5,6,7
0
50
100
150
200
250
300
350
400
450
500
SCT= 8:45:31 22-MAR-83
COUNTS VS. ELEMENT

FIGURE 6.5.3-3

7.0 STABILITY AND REPEATABILITY

7.1 High-Voltage, Thermal, and Aperture Mechanism Effects

Operational constraints allow the high voltage to be on for only one FOS detector at a time. After turning on the high voltage, the electric field in the Digicons requires time to achieve equilibrium. For the first 30 minutes after high voltage turn on, large image shifts (on the order of 1 micron per minute) are present. This motion decreases to less than 2 microns per hour after 60 minutes. Studies of the motion for a longer period using data taken to measure aperture repeatability, showed a small (1.2 micron/hour) drift up to five hours after turn on. However, this drift may be due to temperature effects.

The aperture repeatability data demonstrated that the aperture position on the photocathode was repeatable to within one micron.

During the transition from cold to hot operate, a motion of the spectrum along the diode array of 32 microns was measured on the blue side for a change of 5°C in the optical bench temperature.

To monitor the image stability after high voltage turn on, a series of platinum-neon spectra was taken using grating H27. Data were acquired for both detectors for a period of one hour after high voltage turn on. Data were taken at both cold and hot operate temperatures. To monitor the image stability for a longer period, these data were supplemented with data taken to measure the aperture wheel repeatability. These later data were

of 7 dispersers. With the additional motor step, the standard deviation was found to be 3.2 microns, indicating an average improvement of more than a factor of 2! The improvement ranged from ~20% to a factor of nearly 3.5, depending on the disperser selected. The full range of minimum to maximum X-position over the 9 trials for each of the tested dispersers is plotted in Figure 7.2.2-1, along with some previous measurements made in the same manner. The mean spread has been reduced by approximately a factor of 2, from 21 microns for the October 1984 measurements to 10.2 microns.

Although these data indicate that a noticeable improvement in the FGW repeatability is likely to result from the simple addition of a single step command following each wheel positioning, we note that even the performance level measured in the March 6 test is not entirely satisfactory, particularly for target acquisition into the smallest, 0.1 arcsecond (A4) apertures. The ~10-micron spread in the (camera mirror) aperture image location, inferred from the average behavior of the 7 dispersers tested, remains a large fraction of the (14-micron) A4 aperture image size. For a substantial percentage of A4 acquisitions, the target will suffer significant decentering. Thermal drifts, which may now dominate the non-repeatability, will aggravate the situation. Furthermore, we have no assurance that the behavior demonstrated in our tests is applicable to the camera mirror, which was not actually measured, or that the improvement noted in the X direction will be reflected in the Y axis, since no correlation between X and Y errors was present in

only available on the red side and extended to five hours after high voltage turn on.

Motion between spectra was computed using cross-correlation techniques. In order to analyze motion versus diode position, the data were separated into groups containing diodes 1-100, 101-200, 201-300, 301-400, and 401-500. Cross-correlation was done on each group separately. To obtain motion estimates below the 50-micron resolution of the pixels and the 12.5-micron data sample spacings, the minimum of the correlation matrix was found and a quadratic fit was done using that point and its two neighbors. The position of the minimum of the quadratic fit was used to give the relative spectral motion.

Figures 7.1-1 to 7.1-5 show the results for the blue tube in hot and cold operate. All shifts are relative to the last spectrum taken at cold operate. Large image motions are seen for the first 30 minutes with the largest shifts at the two ends of the diode array. The large offsets between the hot and cold operate spectra, seen 60 minutes after turn on, are due to the lack of perfect repeatability of the filter-grating wheel. Figures 7.1-6 to 7.1-10 show similar results for the red tube.

Figures 7.1-11 to 7.1-15 show an attempt to measure the high voltage settling after one hour using data taken to study the aperture wheel repeatability. All motion is relative to zero motion at 60 minutes after turn on. The aperture repeatability data were shifted in time by 45 minutes to match the previous data. After 100 minutes, all diodes moved in the same direction at a rate of 1.2 microns per hour. This small drift may be

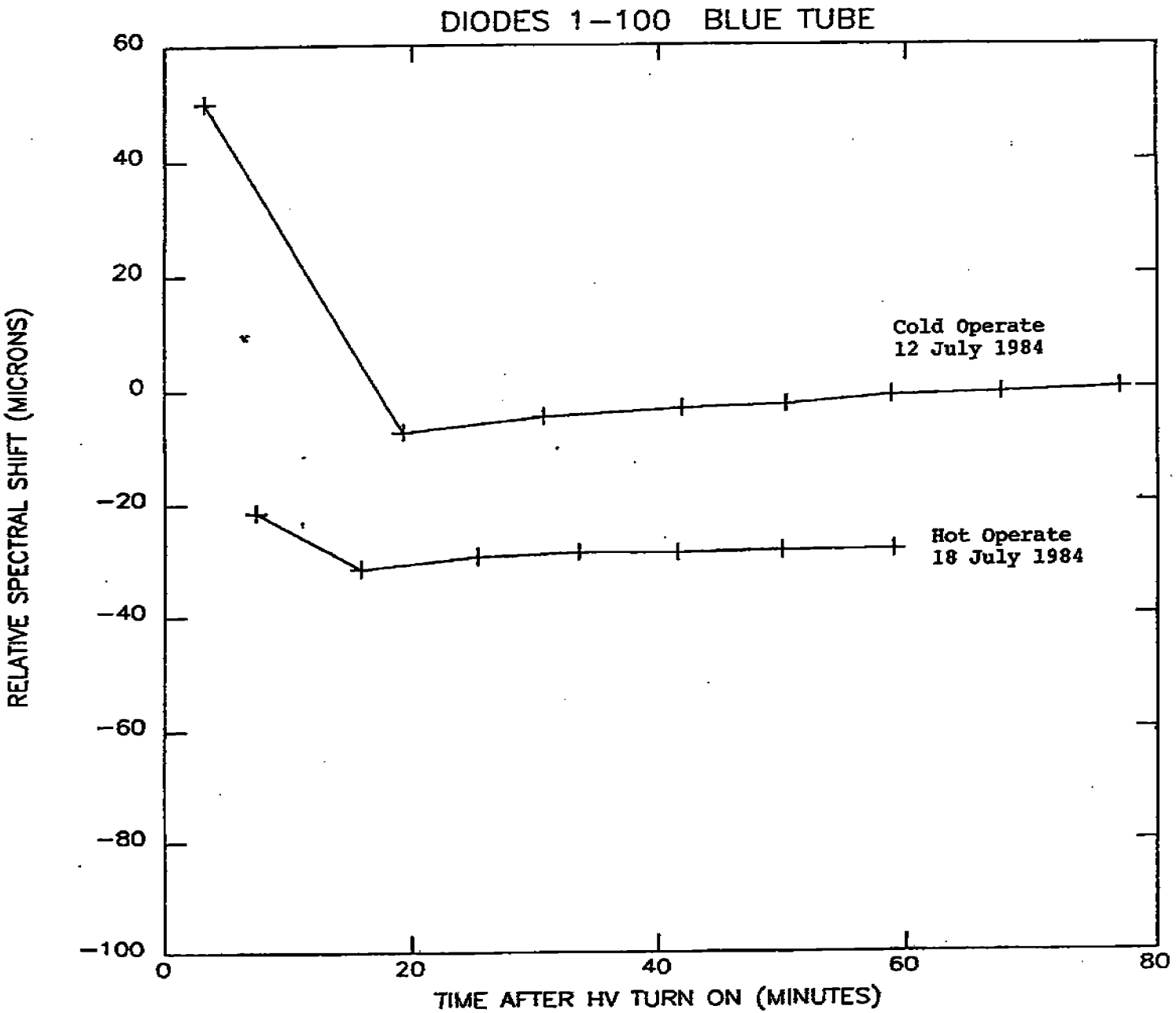
DIODES 1–100 BLUE TUBE
RELATIVE SPECTRAL SHIFT (MICRONS)
60
40
20
0
−20
−40
−60
−80
−100
0
20
40
60
80
TIME AFTER HV TURN ON (MINUTES)
Cold Operate
12 July 1984
Hot Operate
18 July 1984

FIGURE 7.1-1

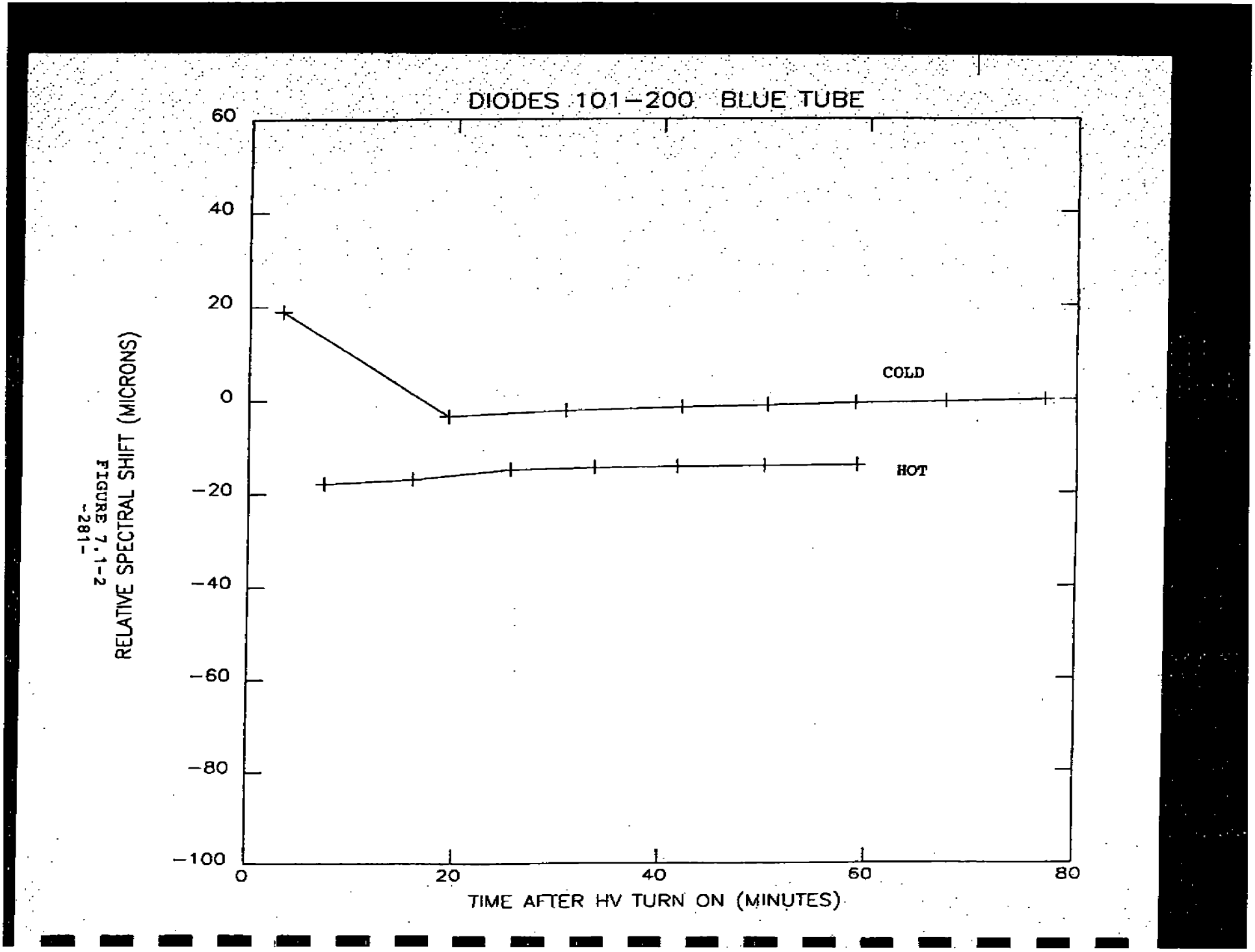

FIGURE 7.1-2
-281-

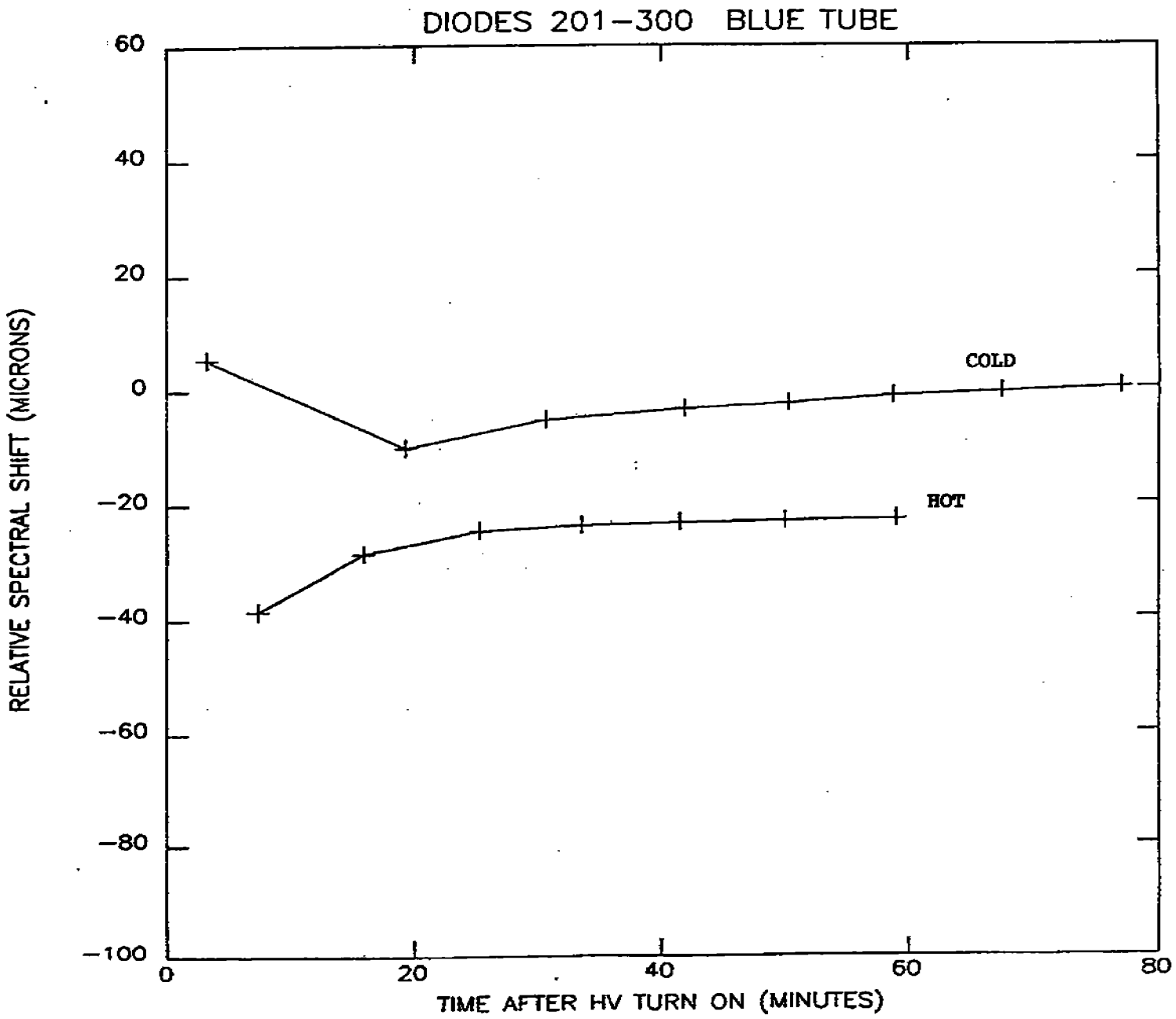
DIODES 201–300 BLUE TUBE
60
40
20
0
−20
−40
−60
−80
−100
0
20
40
60
80
COLD
HOT
RELATIVE SPECTRAL SHIFT (MICRONS)
TIME AFTER HV TURN ON (MINUTES)

FIGURE 7.1-3

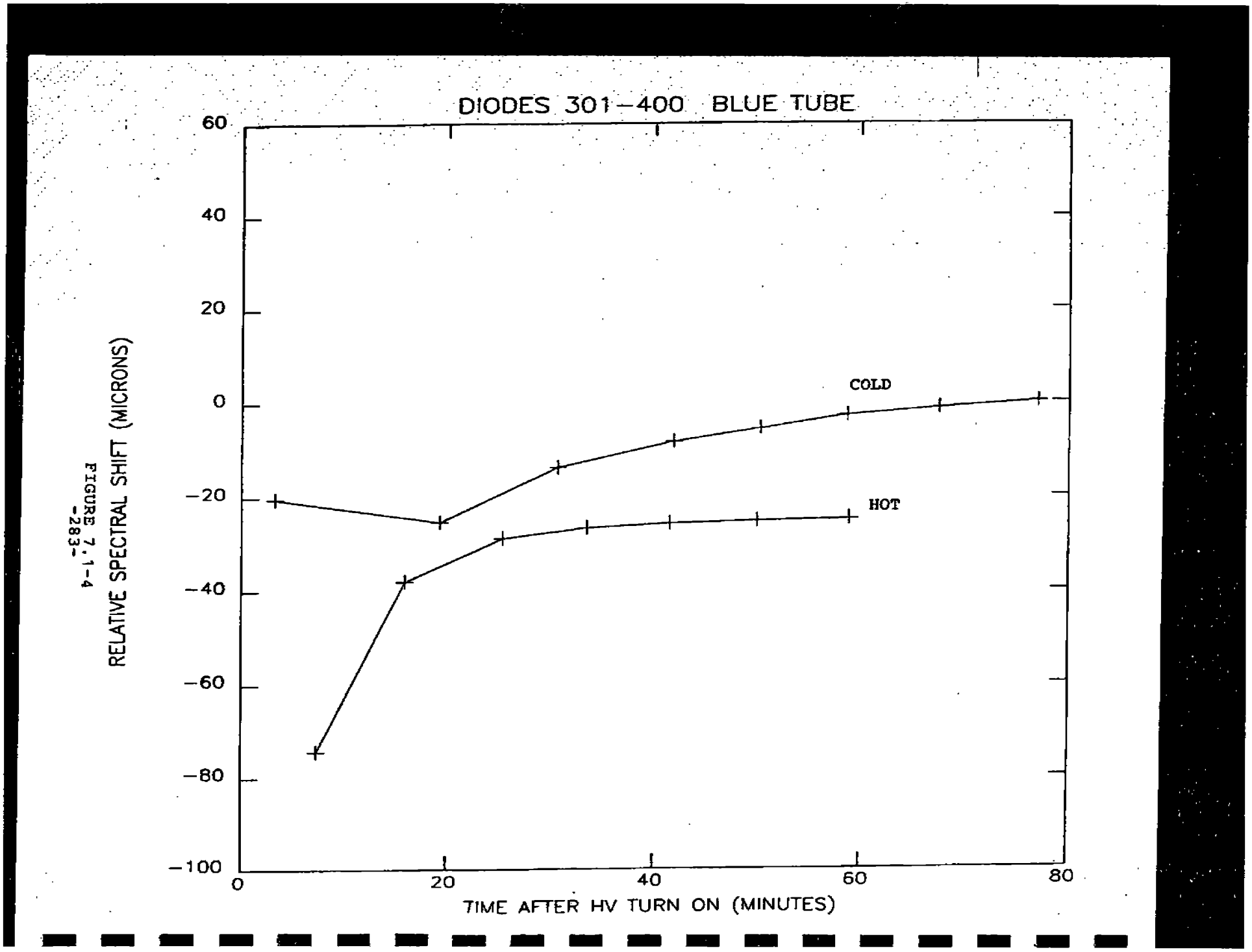
DIODES 301–400 BLUE TUBE
RELATIVE SPECTRAL SHIFT (MICRONS)
60
40
20
0
−20
−40
−60
−80
−100
0
20
40
60
80
TIME AFTER HV TURN ON (MINUTES)
COLD
HOT

FIGURE 7.1-4

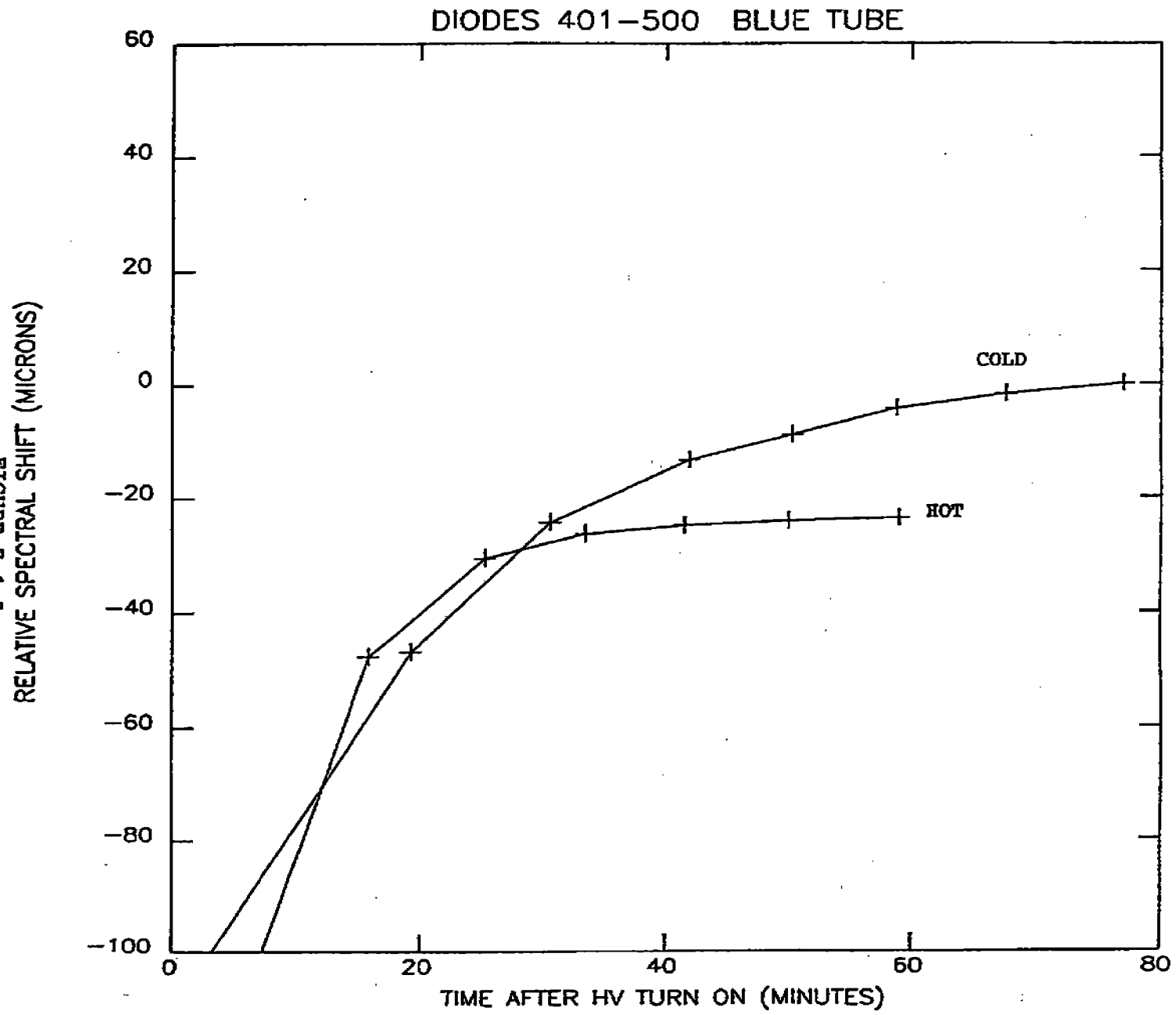

FIGURE 7.1-5
-284-

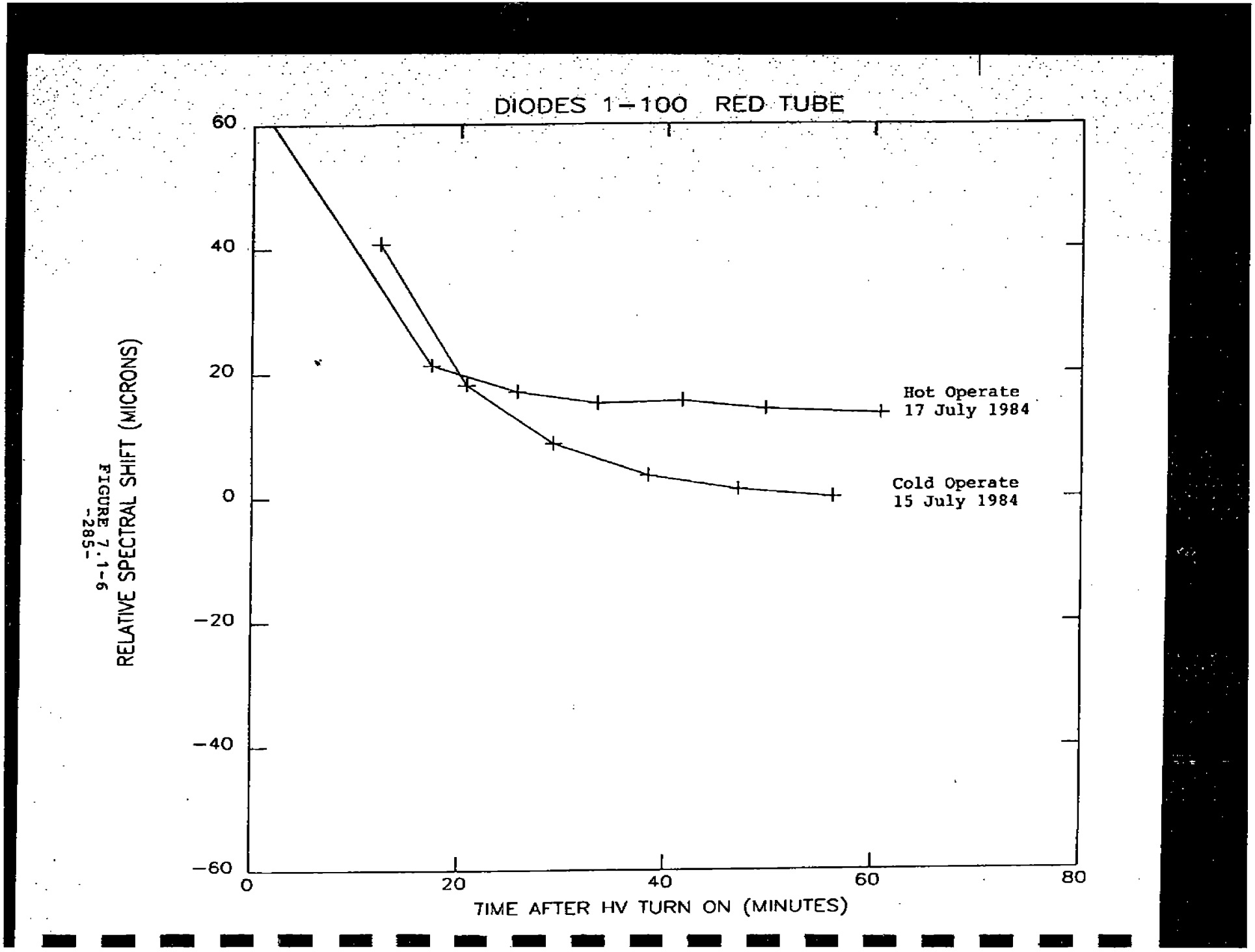

FIGURE 7.1-6
-285-

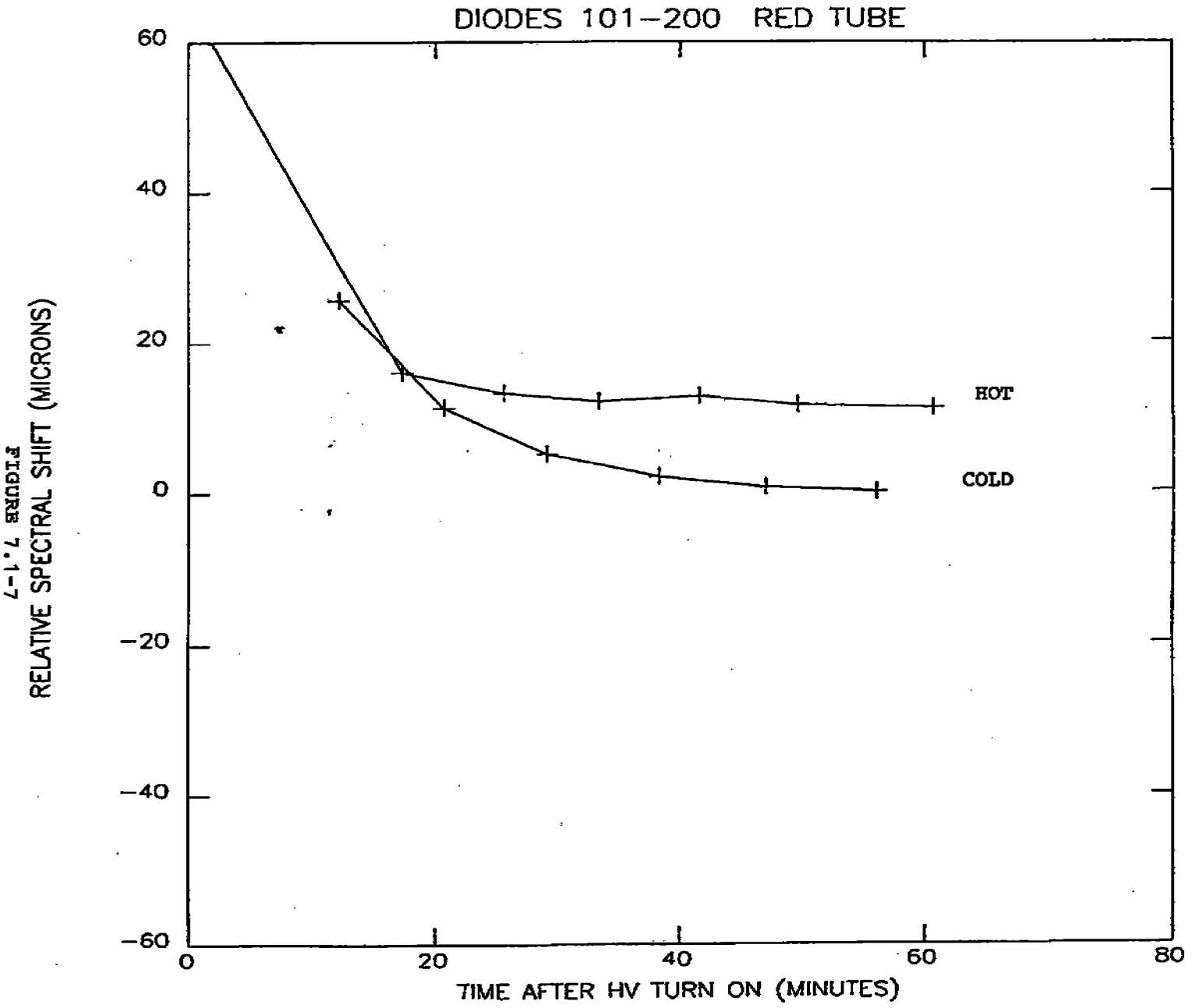
DIODES 101–200 RED TUBE
60
40
20
0
−20
−40
−60
0
20
40
60
80
HOT
COLD
RELATIVE SPECTRAL SHIFT (MICRONS)
TIME AFTER HV TURN ON (MINUTES)

FIGURE 7.1-7

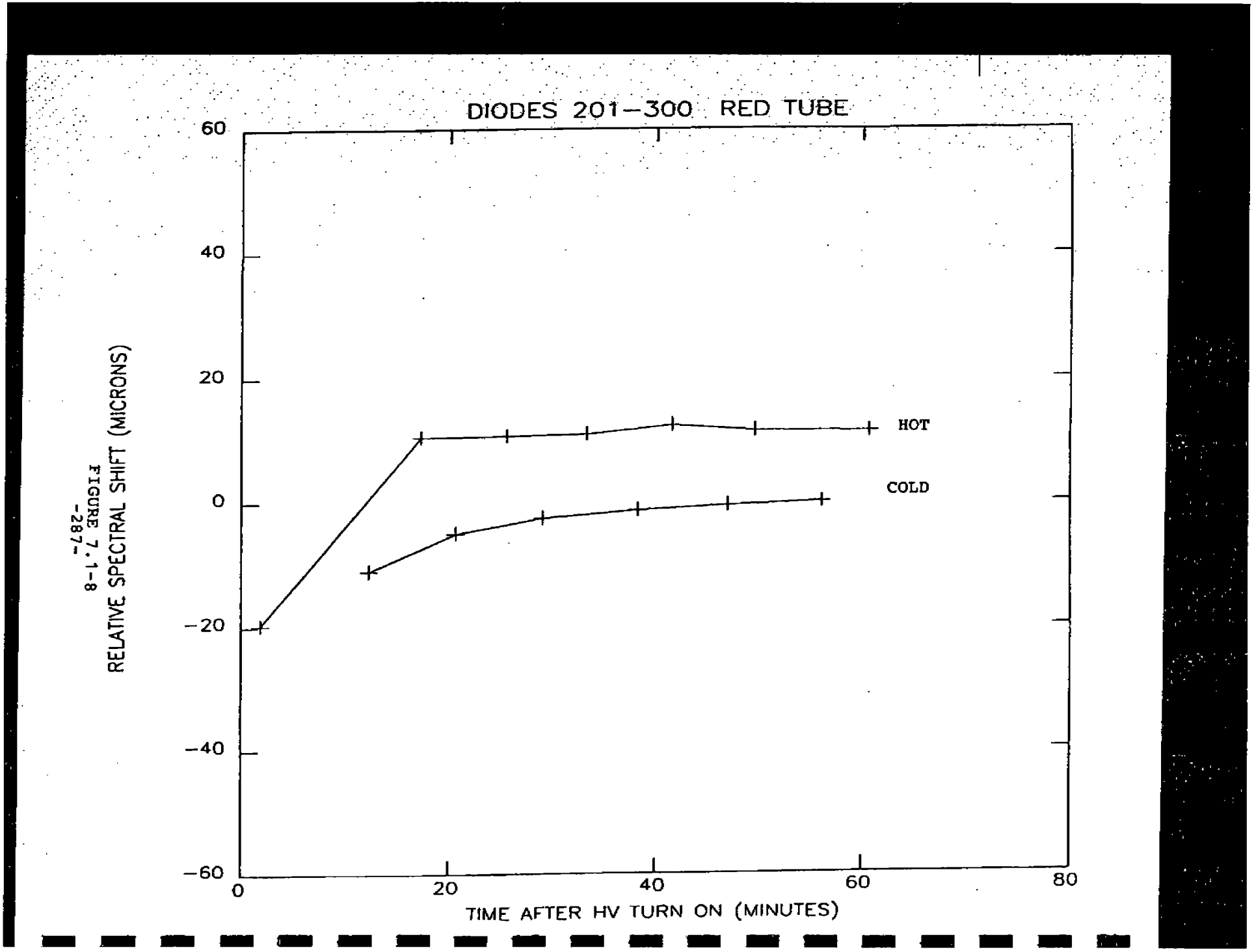
DIODES 201–300 RED TUBE
60
40
20
0
−20
−40
−60
0
20
40
60
80
HOT
COLD
RELATIVE SPECTRAL SHIFT (MICRONS)
TIME AFTER HV TURN ON (MINUTES)

FIGURE 7.1-8

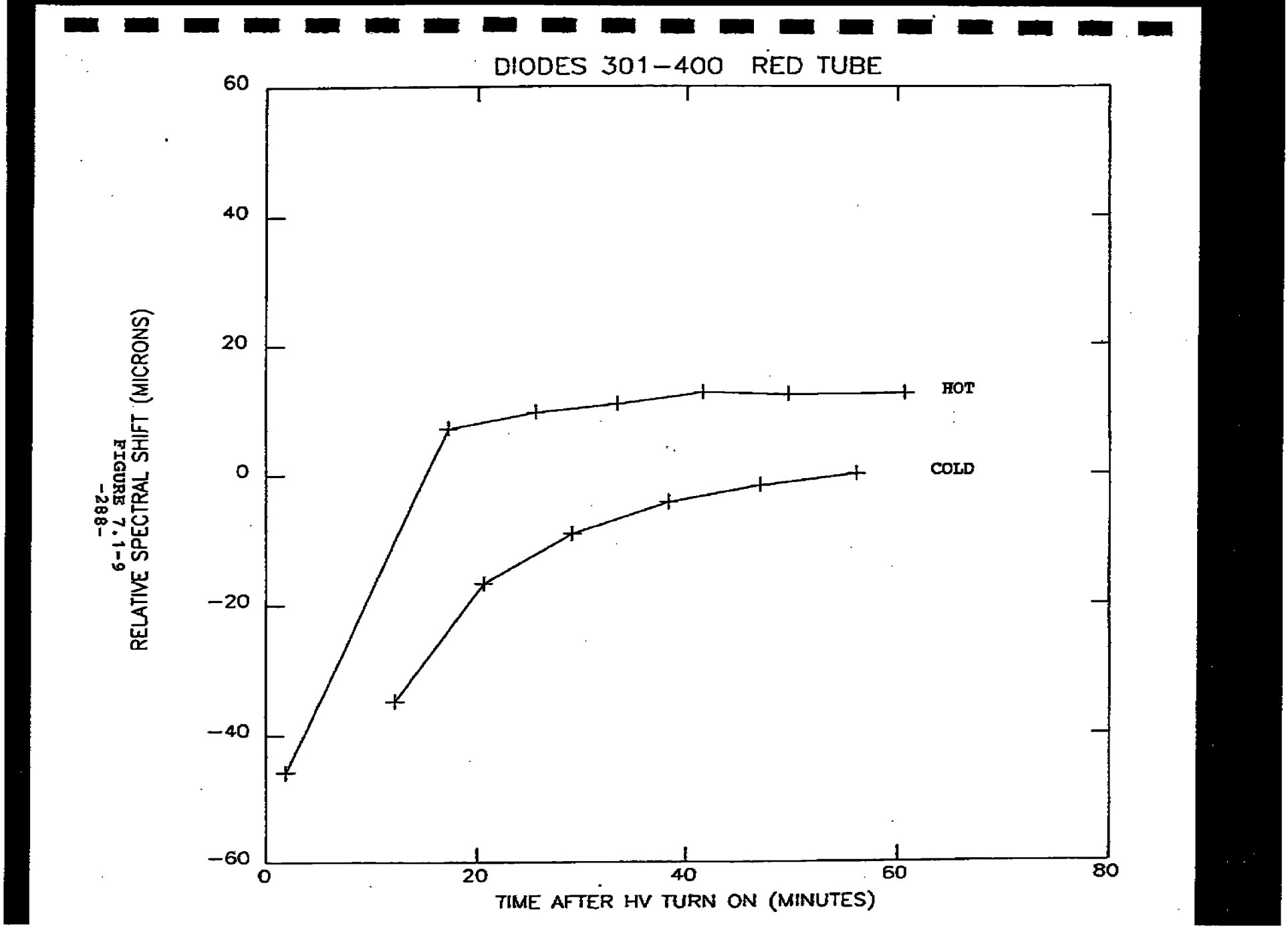
DIODES 301-400 RED TUBE
60
40
20
0
-20
-40
-60
0
20
40
60
80
HOT
COLD
RELATIVE SPECTRAL SHIFT (MICRONS)
TIME AFTER HV TURN ON (MINUTES)

FIGURE 7.1-9

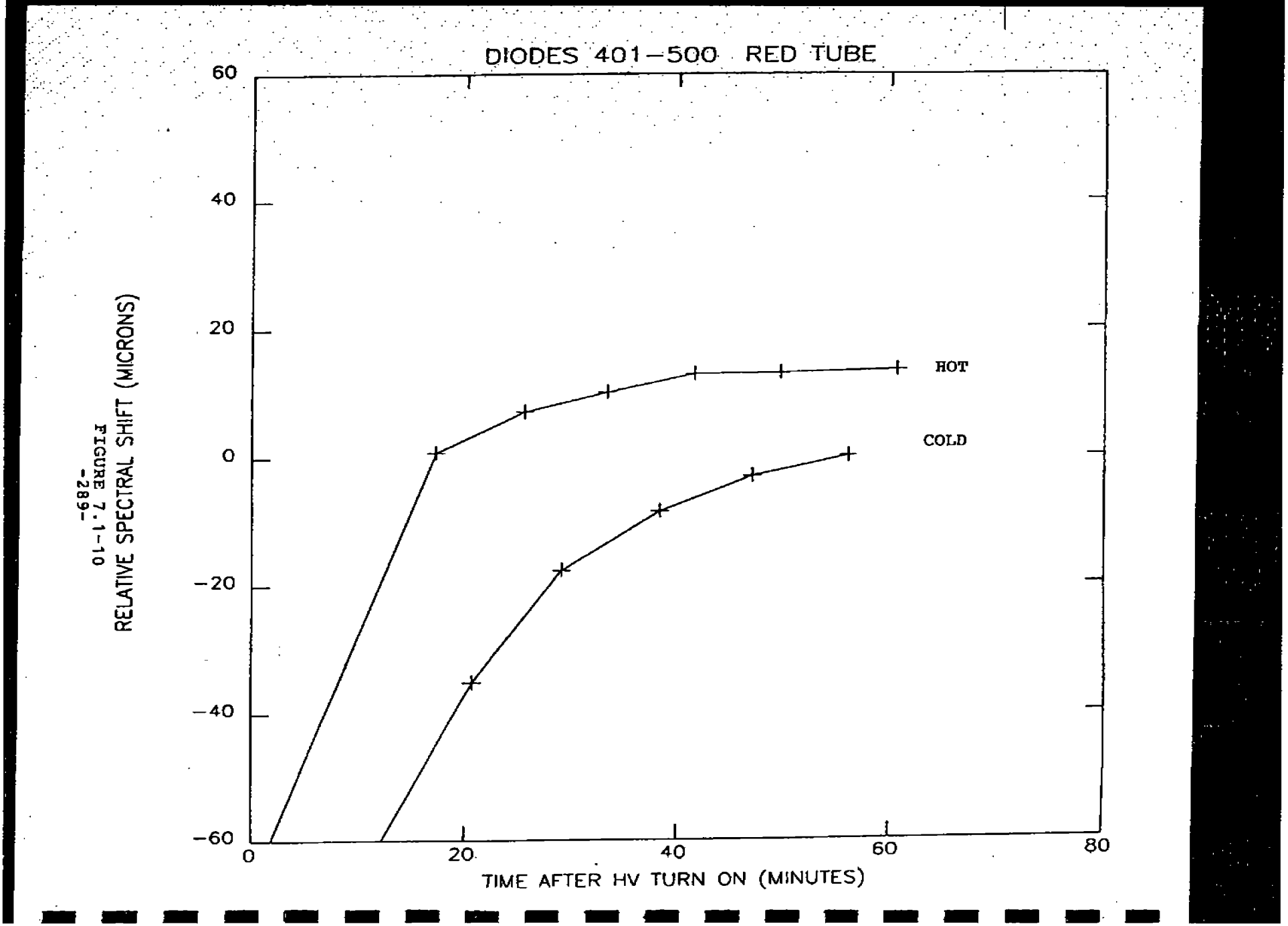
DIODES 401–500 RED TUBE
60
40
20
0
−20
−40
−60
0
20
40
60
80
HOT
COLD
RELATIVE SPECTRAL SHIFT (MICRONS)
TIME AFTER HV TURN ON (MINUTES)

FIGURE 7.1-10

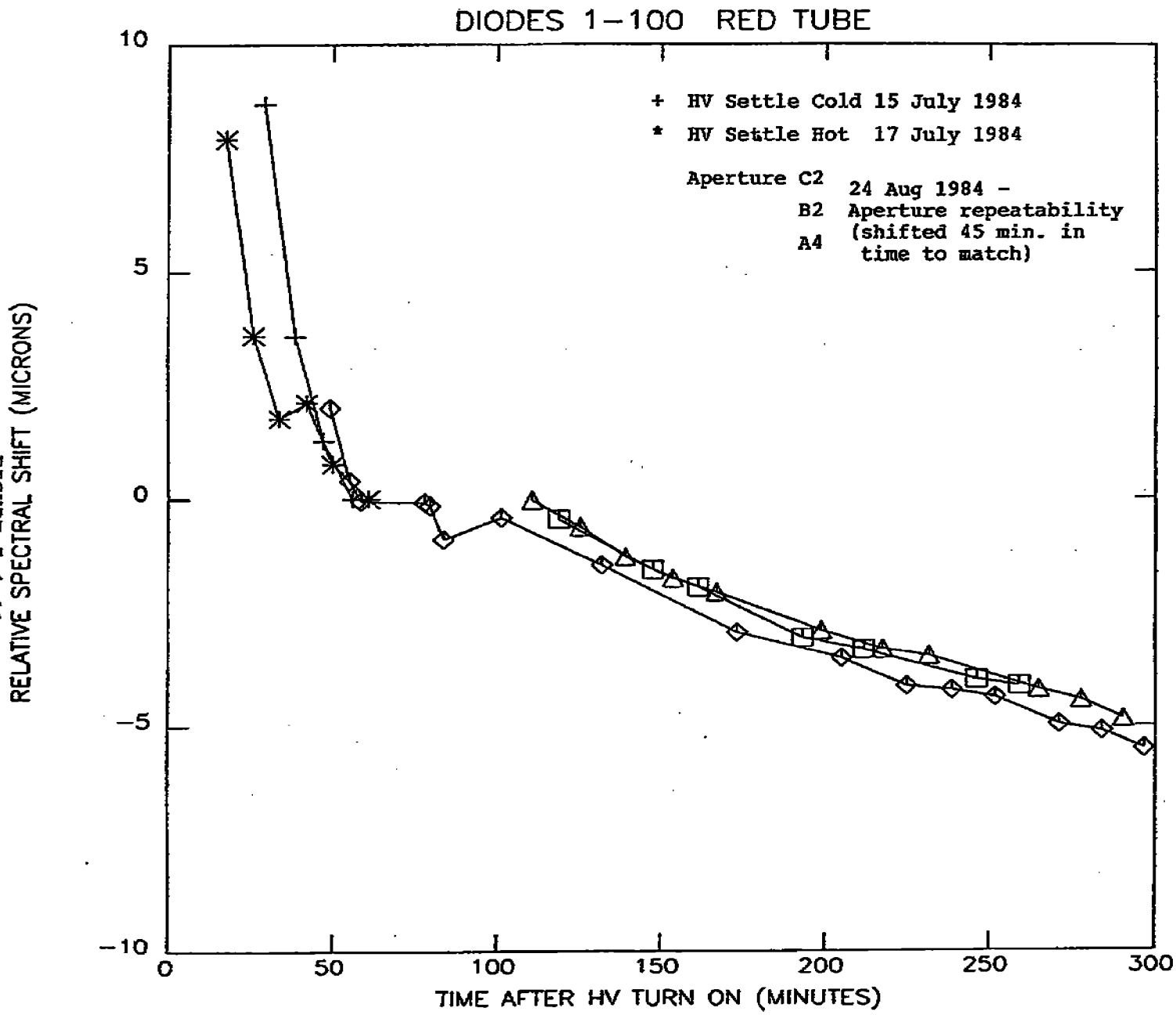
DIODES 1–100 RED TUBE
+ HV Settle Cold 15 July 1984
* HV Settle Hot 17 July 1984
Aperture C2
B2
A4
24 Aug 1984 –
Aperture repeatability
(shifted 45 min. in
time to match)
RELATIVE SPECTRAL SHIFT (MICRONS)
TIME AFTER HV TURN ON (MINUTES)
10
5
0
−5
−10
0
50
100
150
200
250
300

FIGURE 7.1-11

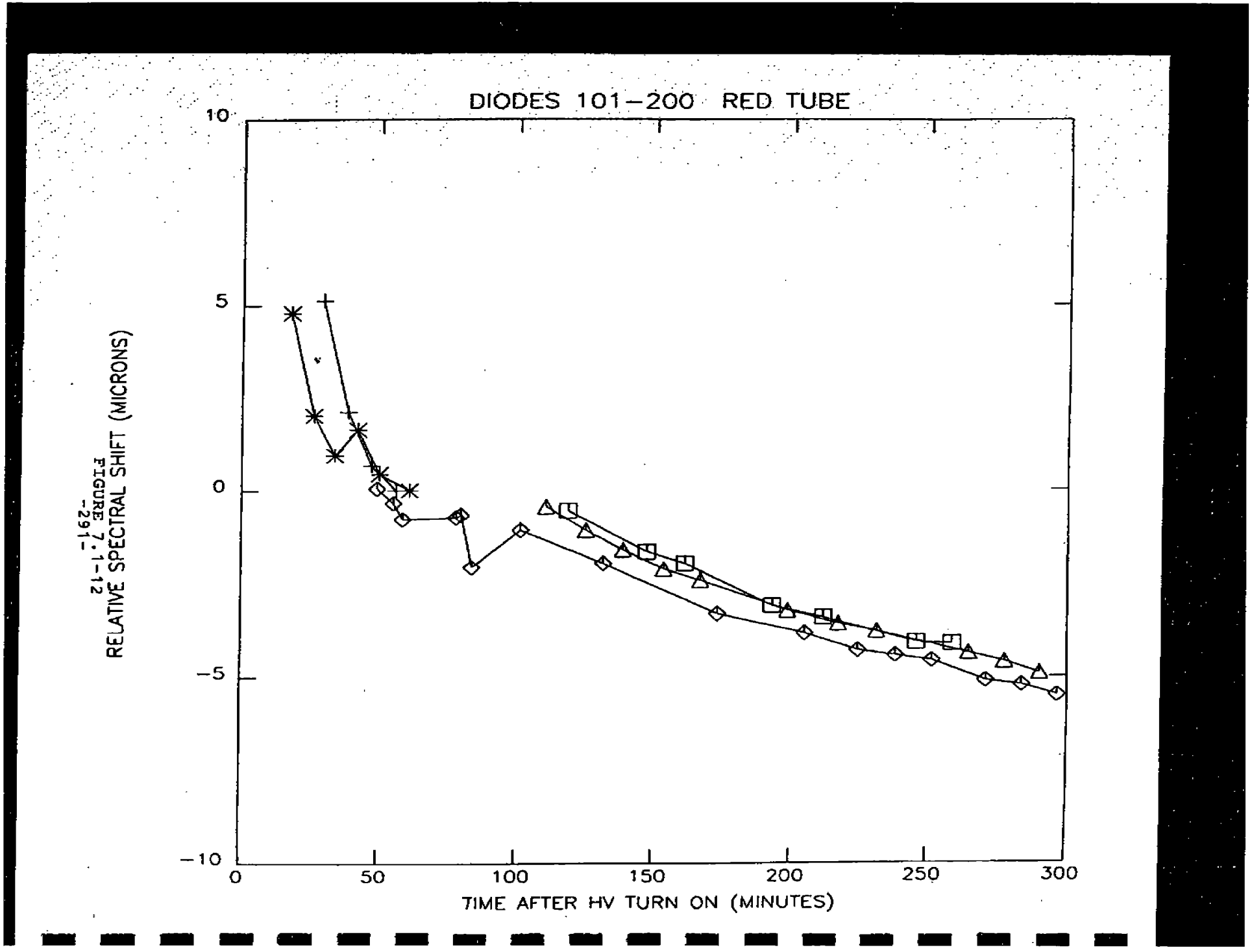

FIGURE 7.1-12
-291-

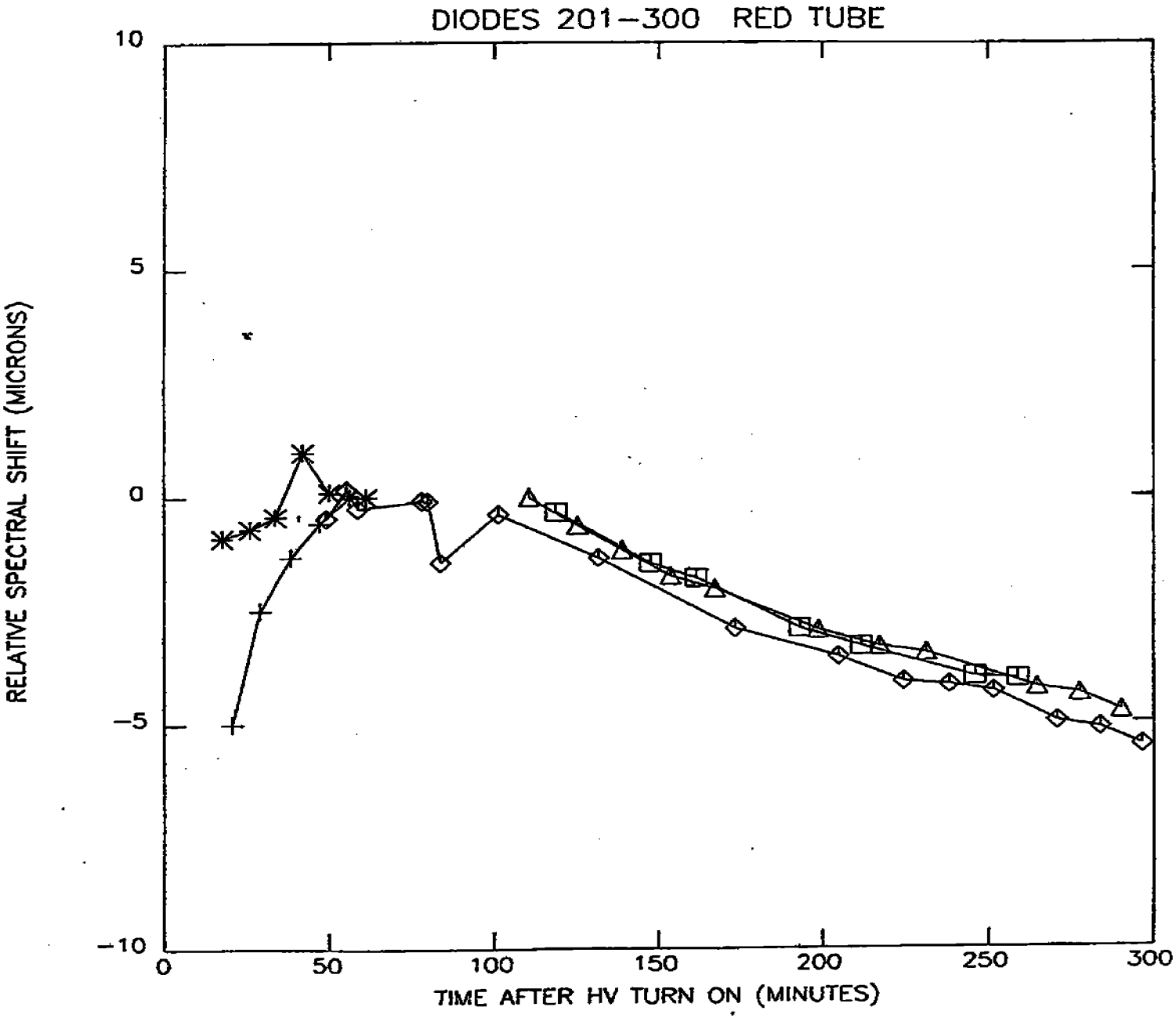

FIGURE 7.1-13
-292-

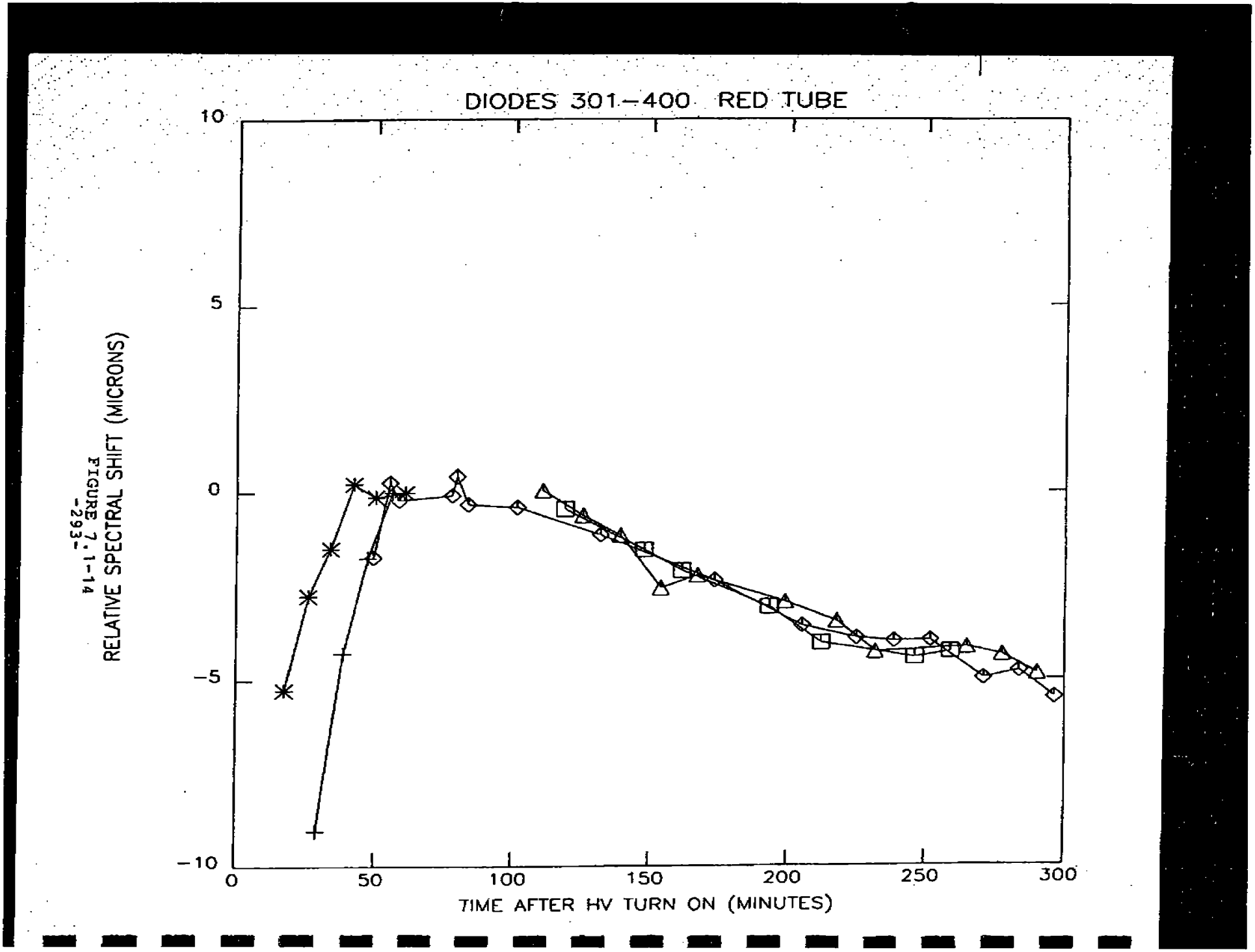

FIGURE 7.1-14
-293-

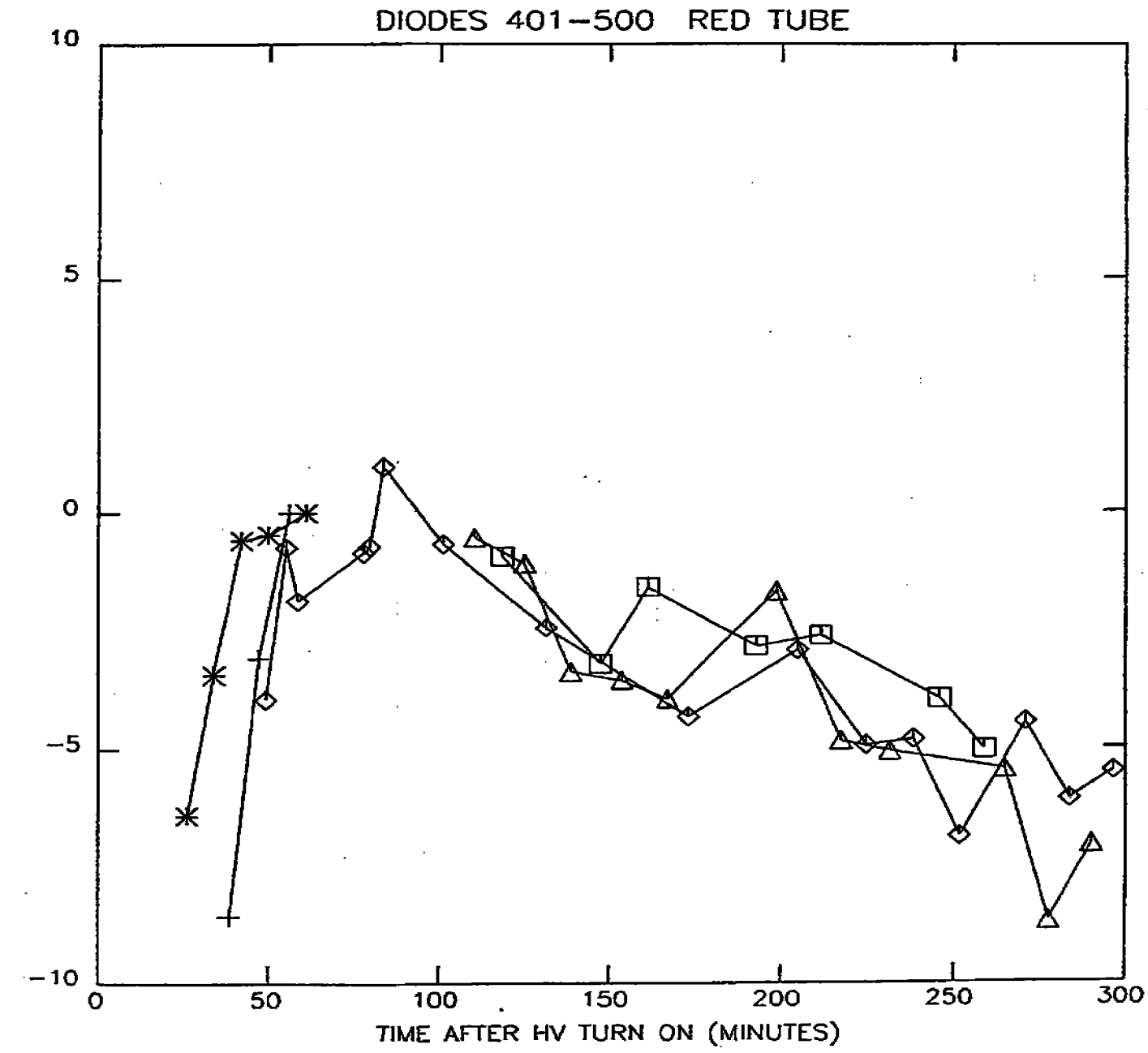

FIGURE 7.1-15
-294-